TECHNISCHE
UNIVERSITÄT
DRESDEN

Integrated nanoscaled detectors of biochemical species

Dissertation
zur Erlangung des wissenschaftlichen Grades
Doktoringenieur
(Dr.-Ing.)

vorgelegt von

Julian Benjamin Schütt
geboren am 10. November 1987 in Esslingen am Neckar

Institut für Werkstoffwissenschaft
Lehrstuhl Materialwissenschaft und Nanotechnik
Fakultät Maschinenwesen
Technische Universität Dresden
2018

Eingereicht am : 14.08.2018
Verteidigt am : 11.01.2019

Erklärung

a) Hiermit versichere ich, dass ich die vorliegende Arbeit ohne unzulässige Hilfe Dritter und ohne Benutzung anderer als der angegebenen Hilfsmittel angefertigt habe; die aus fremden Quellen direkt oder indirekt übernommenen Gedanken sind als solche kenntlich gemacht.

b) Bei der Auswahl und Auswertung des Materials sowie bei der Herstellung des Manuskripts habe ich Unterstützungsleistungen von folgenden Personen erhalten:

Sebastian Pregl: Herstellung der Siliziumnanodraht Feld Effekt Transistoren Chips (Unterkaptiel 4.2.1)

Felix Zörgiebel: MATLAB-Programmcode der FET Steuerung (Unterkaptiel 3.5.1)

Elisabetta Avitabile: PBMC Isolation, Bereitstellung und Durchflusszytometrie (Unterkaptiel 3.6.1 und 5.12.2)

Gleb Milyukov: Programmierung des Machine-Learning Algorithmus (Unterkaptiel 5.13.2)

Martina Rauner: Isolation und Bereitstellung PBMC Populationen von gesunden und kranken Spendern (Unterkaptiel 5.13)

Weitere Personen waren an der geistigen Herstellung der vorliegenden Arbeit nicht beteiligt. Insbesondere habe ich nicht die Hilfe eines kommerziellen Promotionsberaters in Anspruch genommen. Dritte haben von mir keine geldwerten Leistungen für Arbeiten erhalten, die in Zusammenhang mit dem Inhalt der vorgelegten Dissertation stehen.

c) Die Arbeit wurde bisher weder im Inland noch im Ausland in gleicher oder ähnlicher Form einer anderen Prüfungsbehörde vorgelegt und ist auch noch nicht veröffentlicht worden.

d) Diese Promotionsordnung der Fakultät Maschinenwesen an der TU Dresden vom 01.07.2001 wird anerkannt

Datum Julian Schütt

Abstract

Rapid and reliable diagnostics of a disease represents one of the main focuses of today's academic and industrial research in the development of new sensor prototypes and improvement of existing technologies. With respect to demographic changes and inhomogeneous distribution of the clinical facilities worldwide, especially in rural regions, a new generation of miniaturized biosensors is highly demanded offering an easy deliverability, low costs and sample preparation and simple usage. This work focuses on the integration of nanosized electronic structures for high-specific sensing applications into adequate microfluidic structures for sample delivery and liquid manipulation. Based on the conjunction of these two technologies, two novel sensor platforms were prototyped, both allowing label-free and optics-less electrochemical detection ranging from molecular species to eukaryotic micron-sized human cells.

In the first part of the work, silicon nanowire field effect transistors (SiNW FET) were integrated into emulsion-based microfluidic structures for label-free and optics-less sensing of nanoliters droplets, guided over a SiNW FET geometry. These sensors demonstrated significant differences in their conductance, while being exposed to the flow of alternating liquid phases with different electrical properties, *e.g.* conductivities and dielectric constants. Further, the platform showed significant sensitivity towards aqueous droplets in the range of physiological pH values from 4-8 as well as towards ionic concentrations of the surrounding buffer solution over three magnitudes. Finally, the kinetics of a chemical reaction, namely oxidation of glucose by glucose oxidase, was tracked in microfluidic droplets based on the accompanied pH drop during the reaction. In the second part of the work, the fabrication of a sensing platform is demonstrated from scratch for label-free detection of micron-sized biospecies on chip scale. Interdigitating gold nanowire arrays were integrated into a microfluidic hydrodynamic focusing geometry, which allowed guidance of the analyte liquid directly to the nanowire geometry. Based on the methodology of electrical impedance cytometry (EIC), alterations of the device's impedance were tracked when an analyte enters the area of influence of its electric field. Here, by introduction of a new element (the analyte) into the equivalent circuit of the system, its dielectric properties and self-impedance can be tracked dependent on

its membrane configuration and size. Here, successful electrochemical and label-free differentiation of human peripheral blood mononuclear cells (PBMCs) from healthy donors and donors with acute myeloid leukemia (AML) is demonstrated. Finally, the novel sensor platform’s detection limit was explored by analysis of various bacteria strains.

In conclusion, the developed sensor platforms in this work contribute to an alternative miniaturized and automated strategy of established state-of-the-art methodologies for diagnostics of diseases. Here, without the use of secondary optical label compounds, sensitive detection of analytes ranging from the molecular level to micron-sized biospecies was successfully demonstrated on a pure electrical detection mode using nanosized detection elements.

Kurzfassung

Rasche und zuverlässige biologische Krankheitsdiagnostik repräsentiert eines der Hauptfokusse heutiger akademischer und industrieller Forschung in der Entwicklung neuer Sensor-Prototypen und Verbesserung existierender Technologien. In bezug auf weltweite demographische Änderungen und hohe Distanzen zu Kliniken, besonders in ländlichen Gegenden, werden zusätzliche Anfordungen an neue miniaturisierte Biosensor-Generationen gestellt, wie zum Beispiel ihre Transportfähigkeit, geringe Kosten und Probenpräparation, sowie einfache Handhabung. Diese Dissertation beschäftigt sich mit der Integration nanoskalierter Strukturen zur Detektion chemischer und biologischer Spezies und mikrofluidischen Kanälen zu deren Transport und zur Manipulation der Ströme. Basierend auf der Verbindung dieser beiden Technologien wurden zwei Sensor-Plattformen entwickelt, die eine markierungsfreie und nicht-optische elektrische Detektion von Molekülen bis zu eukaryotischen menschlichen Zellen erlauben.

Der erste Teil dieser Arbeit widmet sich der Integration von Silizium-Nanodraht Feld-Effekt-Transistoren (SiNW FET) in emulsions-basierte mikrofluidische Strukturen zur markierungsfreien und optisch-freien Detektion von Tropfen im Bereich von wenigen Nanolitern, die über die SiNW FET Struktur geführt werden. Die genutzten SiNW FETs zeigten signifikante Unterschiede in ihrer Leitfähigkeit in Abhängigkeit der alternierenden Phasen, basierend auf ihren unterschiedlichen elektrischen Eigenschaften. Zudem zeigte die Sensor-Plattform Sensitivität gegenüber wässrigen Tropfen mit physiologisch-relevanten pH-Werten (von pH-Werten zwischen 4 bis 8) und ionischen Konzentrationen über drei Größenordnungen. Zuletzt wurde die Kinetik einer chemischen Reaktion, nämlich der Oxidation von Glukose mittels Glukose-Oxidase, in mikrofluidischen Tropfen beobachtet, da während der Reaktion der pH-Wert durch Bildung von Glukonsäure verringert wird. Der zweite Teil der Arbeit beschäftigt sich mit der Herstellung einer Impedanz-basierender Detektionsplattform für markierungsfreie Detektion von Bio-Spezies in der Mikrometer-Dimension auf Chip-Ebene. Ineinandergreifende Gold-Nanodraht Anordnungen wurden in eine mikrofluidische hydrodynamische Fokussierungsstruktur integriert, welche eine Führung des Analyten direkt auf die

Detektionsstruktur erlaubte. Basierend auf der Methodik der elektrischen Impedanz-Durchflusszytometrie (EIC), konnten Unterschiede der Sensor-Impedanz gemessen werden, welche durch die Anwesenheit des Analyten im Einwirkungsbereich des elektrischen Feld induziert wurde. Durch die Einführung des neuen Elements (des Analyten) in das Ersatzschaltbild des elektrischen Systems konnte die Eigenimpedanz sowie die dielektrische Eigenschaften des Analyten beobachtet werden, welche abhängig von seiner Oberflächenkonfiguration und Größe waren. Es wurde erfolgreich eine markierungsfreie und nicht-optische Differenzierung von peripheren mononukleären Blutzellen (PBMCs) von gesunden Spendern und einer Spenderin, bei welcher akute myeloidischer Leukämie (AML) diagnostiziert wurde, durchgeführt. Zuletzt wurde das Detektionslimit der Sensor-Plattform mittels Detektion und Analyse verschiedener Bakterienstämme erforscht.

In Zusammenfassung können die entwickelten Sensor-Platformen zu einer minaturisierten und automatisierten Alternative für etablierte und hochmoderne Methodiken der Krankheitsdetektion beitragen. Sensitive Detektion von Analyten vom molekularen Level bis zu Biospezies im Mikrometer-Bereich, konnten erfolgreich ohne die Benutzung optischer Markierungsverbindungen rein elektrisch mittels nanodimensionierter Detektionselementen erfasst werden.

Content

Table of Figures

List of Tables

Abbreviations

General

MEMS	Microelectromechanical systems
NEMS	Nanoelectromechanical systems
PBS	Phosphate buffered saline
POC	Point-of-care
GOx	Glucose oxidase
HRP	Horseradish peroxidase
TMB	3,3’,5,5’ tetramethylbenzidine
oDCB	1,2-dichlorobenzene/orthodichlorobenzene

Transistors

MOS	Metal-oxide-semiconductor
CMOS	Complementary metal-oxide-semiconductor
FET	Field effect transistor
MOSFET	Metal-oxide-semiconductor field effect transistor
ISFET	Ion-sensitive field effect transistor
SiNW FET	Silicon nanowire field effect transistor
EDL	Electrical double layer
EDLC	Electrical double layer capacitance

Impedance Biosensing

EIS	Electrical impedance spectroscopy
EIC	Electrical impedance cytometry

Methods

EBL	Electron beam lithography
SEM	Scanning electron microscope
PBMC	Peripheral blood mononuclear cell
AML	Acute myeloid leukemia
PMMA	Poly(methylmethacrylate)
PDMS	Poly(dimethylsiloxane)

Re	Reynolds number
APTES	(3-Aminopropyl)triethoxysilane
FITC	Fluorescein isothiocyanate
FIB	Focused ion beam
AFM	Atomic force microscopy

List of Symbols

Transistors

General

S	Source
D	Drain
G	Gate
V_{SD}	Source-drain voltage
V_{GS}	Source-gate voltage
I_{SD}	Source-drain current
I_{SD}	Source-gate current
V_{T}	Threshold voltage

Experimental

Q_{water}/Q_{oil}	Flow ratio of water and oil
$R_{Droplet/Oil}$	Reference ratio of droplet and oil signals
R_{0}	Pre-reaction ratio of droplet and oil signals
$\Delta R_{Droplet/Oil}$	Subtraction difference of $R_{Droplet/Oil}$ and R_0

Impedance Biosensing

General

σ_{c}	Cytoplasm conductivity
ε_{c}	Cytoplasm dielectric constant
σ_{m}	Membrane conductivity
ε_{m}	Membrane dielectric constant
C_{p}	Particle capacitance
C_{m}	Medium capacitance
C_{eq}	Equivalent circuit capacitance
C_{dl}	Double-layer capacitance
R_{p}	Particle resistance
R_{m}	Medium resistance
R_{eq}	Equivalent circuit resistance
R_{ct}	Charge-transfer resistance

A_{gap}	Pitch area between the nanowires

Impedance calculation

Z	Impedance
Z'	Real part of the impedance
Z''	Imaginary part of the impedance
V_{out}	Output signal amplitude
V_{in}	Input signal amplitude
ω	Angular frequency ($2\pi f$)
C_{ref}	Inner capacitance of the measurement device (10pF)
R_{ref}	Inner resistance of the device (1 MΩ)
$Phase_{rad}$	Output signal phase shift (in rad)
$Phase_{deg}$	Output signal phase shift (in degree)

Experimental

z[m]	Particle height in channel
ΔV_{out}	Analyte amplitude signal change
$\Delta Phase$	Analyte phase shift signal change

Microfluidics

ρ	Liquid density
v	Liquid velocity
d	Channel length
h	channel height
η	Liquid dynamic viscosity
F_{γ}	Surface tension force
γ	Interfacial tension coefficient
F_{τ}	Shear stress force
μ_c	Viscosity continuous phase
Q_c	Speed continuous phase
F_R	Flow resistance force
w_c	Channel width
e	Gap thickness

1 Introduction

1.1 Motivation

Current demographic changes with a population percentage of 13% over 60 years in 2017 worldwide[1] and 22% over 65 years in Germany[2], low access to medical facilities in rural regions and developing countries, as well as costly and stationary devices for clinical diagnostics and treatment, lead to a high demand for portable, easy-to-use and cheap devices as well as sensors for treatment of patients on regular basis and in emergency situations. Here, the utilization of miniaturized diagnostic tools and first aid devices, applicable even by untrained personals, can lead to higher survival rates in emergency situations by immediate treatment on spot[3]. Additionally, they are able to improve life quality of *e.g.* long-term patients treated from their homes by *in vivo* observation of various treatment-related parameters. For instance, miniaturized chip devices, wirelessly connected to the doctor's computer can collect and transfer various health- and disease-indicating parameters in real-time for direct analysis without any temporal or spacial delay by the medical personnel[4,5]. Especially for elderly persons under clinical observation, the need of routine visits during their treatment can be replaced via online diagnostics and thus avoid the strong physical strain of traveling to the hospital or doctor's office. Further, miniature and cheap devices also lead to a faster and cheaper detection of diseases, making an adequate diagnosis and treatment possible for people with lower income. Here, the glucose blood sensor for people diagnosed with *diabetes mellitus* represents most prominent example. Starting from impractical manual needle stinging and *ex vivo* measuring of the glucose level, so called "flash glucose monitoring" device are available nowadays, allowing permanent, painless and user-friendly recording and analysis of the glucose level in vivo[6]. Last but not least, the installation of miniaturized sensors in buildings and streets which able to detect harmful liquids or gaseous substances that can greatly contribute to societal safety[7,8]. In the respective field of research, the field of biosensors, the ultimate goal represents the development of transferring conventional laboratory techniques to a small scale integrated solution on a single chip device. Here, the introduction of several methodologies, *e.g.* electrochemical sensing structures and microfluidics, opens the path for an automated and highly sensitive sensing platform, usable even by untrained persons[9]. Further, the spatial integration of an analyte delivery systems (*e.g.* microfluidics)[10], its recognition structure (receptor) and a platform for signal transfer into an electrical signal (transducer), makes the device portable[11,12]. In order to push real-time diagnostic sensorics to the new generation, both selectivity and sensitivity to molecules and pro- and eukaryotic cells at very low concentrations in complex media (*e.g.* blood, saliva, and urine) has to be improved to guarantee early detection of diseases like cancer or bacterial and viral infections, without the use of bulky devices and trained personnel[13]. Further, the new generation of diagnostic chips has to be able to detect multiple parameters simultaneously in order so screen for multiple disease indicators and analytes[14,15]. Here, the miniaturization concept of nanotechnology comes into play, since it grants down-scaling of sensing structures and thus boosts the number of sensors on one chip. Driven by the semiconductor industry, electronic building blocks can be scaled down to feature sizes down to 5 nm on large scale[16], which can be additionally utilized as sensor elements, *e.g.* field effect transistors (FETs) and capacitors. In the scientific community, nanosized biosensorics gained greatly attention during the last decade offering miniaturized sensors able to detect even single molecules[17]. In the following chapter, the latest accomplishments in these research areas are presented.

1.2 State of the art

The current generation of sensors is mainly based on nanostructures since they offer higher sensitivity due to the high surface-to-volume ratio of sensing elements as well as low background noise due to ballistic electron transport. In detail, semiconducting (*e.g.* silicon nanowires) and metallic (*e.g.* gold nanowires) nanostructures are prominent examples for materials settled in the focus of research in biosensorics due to their excellent electrical properties for biosensing applications, *i.e.* in FET and impedance setups, respectively[18,19]. A detailed description about the transition from the microdimension to the nanodimension with respect to the sensing geometry will be explained in *Chapter 2.1*. In the following, the current state-of-the-art achievements from the last decades of

i) **Silicon Nanowire FETs**
ii) **Impedance Sensing**

are presented.

The utilization of silicon nanowire field effect transistors (SiNW FETs) plays a central role as essential detection element in current research of biosensorics since the first decade of the 2000s. During this time, the work group of Charles Lieber demonstrated the excellent electrical characteristics, namely their mobility and transconductance, of SiNW FETs for their usage in nanoelectronics and label-free biosensing purposes[20–23]. Due to their close relation to industrial-relevant technology, both their electrical responses and geometry optimizations allow high signal-to-noise ratio and stable signal responses over time, making them perfect for investigations with respect to biosensing[24–26]. In this, detection of biomolecules and biospecies became possible at ultra-low analyte concentration based on their highly-specific interaction on the semiconductor surface by *e.g.* immobilized antibodies or aptamers, thereby changing the channel conductance of the FET[27]. In the last decades, a high amount of excellent works has been published, demonstrating the utilization of SiNW FETs as label-free sensing platform. In the following, the achievements during the last years are presented.

Table 1: Authors, year of publication and the detected biological species of state-of-the-art achievements of SiNW FET sensing during the last decades

Authors	Year of Publication	Detected species	Detection Limit
Shehada et. al.[28]	2015	Volatile organic compounds	5ppb
Sivakumarasamy et. al.[29]	2018	Various ion species	µM range
Kim et. al.[30]	2007	Prostate specific antigen	30 aM
Puppo et. al.[31]	2014	Rabbit antigen interaction	5 fM
Presnova et. al.[32]	2017	Prostate specific antigen	0.7 fM
Nuzaihan et. al.[33]	2016	DNA-DNA hybridization	10 fM
Hahm et. al.[34]	2004	PNA-DNA hybridization	10 fM

In 2015, Shehada et. al.[28] demonstrated detection of gaseous volatile organic compounds (VOCs) at ultra-low concentrations down to 5ppb using SiNW FETs. Here, special silane coating of the nanowires allowed discrimination between VOCs originated from environment and VOCs in the exhaled breaths from gastric cancer patients. Very recently in early 2018, the utilization of a SiNW FET as a selective ion-sensor has been demonstrated, able to sense various ion concentrations in a complex medium. Here, the transistor represented a single nanowire transistor with only 30 nm x 40 nm in dimension, therefore referred as "0D-transistor". This geometry allowed different sensitivity towards ions in complex solutions, namely Na^+, K^+, Ca^{2+} and Mg^{2+}, without any signal influence based on the pH value of the solution. Despite the relative high detected ionic concentrations (in range of micromolarities), simultaneous label-free detection of single ions in mixed solution was presented the first time[29]. Furthermore, SiNW FETs are widely used for detection of biomarkers, *e.g.* proteins and enzymes. Kim and co-workers[30] demonstrated ultra-sensitive detection of *prostate specific antigen* (PSA) using SiNW FETs with a detection limit of 30aM. Here, the nanowires where equipped with anti-PSA, a highly-specific antibody for PSA, immobilized by standard silane chemistry. Here, binding of PSA to anti-PSA led to significant alterations in the conductivity of the FET even at ultra-low concentrations. While this experiment was carried out in defined medium (namely phosphate-buffered saline (PBS) buffer), high selectivity and sensitivity of SiNW FETs in complex medium has been successfully demonstrated. Here, Puppo and co-workers[31] demonstrated femto-molar sensitivity towards artificially introduced rabbit antigen molecules in human breast tumor extract. Additionally, the sensitivity of SiNW FET can be increased by utilization of a hybrid strategy, namely the equipment of the nanowires with metallic nanoparticles. Presnova et. al.[32] demonstrated in 2017 that immobilization of 5 nm gold nanoparticles on the nanowires leads to higher pH sensitivity and electric performance of the transistor devices. Here, the antibodies for detection were immobilized directly on the gold nanoparticles via thiol-groups. Doing so, their device was able to sense concentrations of down to 0.7 fM. Another strategy of enhancement of SiNW FET sensitivity was developed by Regonda et. al. in 2013[35]. Here, instead of nanochannel or nanowire geometries, they introduced silicon nanograting structures, able to increase the device's electrical performance including single variations between devices, higher on/off ratio and higher current. Next to gaseous, ionic and protein-sensing, SiNW FET are also capable of detecting short DNA or peptide nuclear acid (PNA) chains, an artificially created DNA-analogue, where the sugar-phosphate backbone is replaced with a pseudo-lipid. Here, the detection is based on the self-organized binding of single DNA (ssDNA) strains to its complimentary chain, covalently bound to the semiconductor surface. Nuzaihan et. al[33] demonstrated in 2016, that conventional SiNW FETs are capable to sense the binding of ssDNA to its complimentary strain in liquid environment, bound to the nanowire surface. In this, changes in their drain current, electrical conductance and resistance was observed upon ssDNA binding. The detected ssDNA only consisted of 27 pairs of nucleotides and could be detected down to a detection limit of 10 fM. Applying the same binding strategy, Hahm and Lieber[19] were able to distinguish wild type and mutant PNA chains based on successful and unsuccessful binding of the PNA polymer to the receptor-PNA. Till now, detection of analytes was either carried out by solution dropping on the sensor or in microfluidic single-phase, *i.e.* delivery sample to the sensor via single microfluidic channels, containing only one type of liquid. Till now, there are no reported results on SiNW FET responses using multiple phases of liquids.

Next to the SiNW FET methodology, where conductance changes are the measured parameter, electric capacitive structures can be utilized to measure modifications at surfaces or in the chemical environment. In this, adhering or growing microorganisms or induced changes of surface properties are tracked by application of an AC voltage over a range of frequencies, called *electrical impedance spectroscopy* (EIS)[36,37]. Further, in the last decades, the throughput of this technique was dramatically improved by fixing the frequency to distinct values and using microfluidic channels for dynamic sample delivery. Here, the detection is based on the modulation of the impedance of the system based on the dielectric properties of the passing analyte, mimicking the conventional flow cytometry methodology and thus called *electrical impedance cytometry* (EIC)[38,39]. The methodology of impedance cytometry and their maturation towards a functional biosensor will be discussed in detail in *Chapter 2.3*. In the following, latest achievements and the current state-of-the-art results in this field are presented.

In electrical impedance cytometry, recent results report on successful detection of several kinds of inorganic micron-sized compounds and biological species during the last decade. In 2009, Holmes and co-workers[40] demonstrated analysis of leukocytes, or white blood cells, using a microelectronic EIC setup combined with an integrated fluorescent double detection. Here, the cells were guided through a thin microfluidic channel equipped with two pairs of opposing microelectrodes, independently actuated at different AC signal frequencies. Additionally, the analyte stream was confined in the middle of the main channel by two co-flowing parallel liquid streams. The double detection at different frequencies allowed isolation of inner analyte parameters, *i.e.* its membrane capacitance and cytoplasmic conductivity. These characteristics are captured by the division of the cell's impedance at different frequencies, called "*opacity*". Based on this strategy, differentiation of leukocytes, namely monocytes, neutrophils and lymphocytes was successfully demonstrated. One year later, the setup was further improved by Holmes et. al.[41] by introduction of cell specific antibody-conjugated beads which alter the electrical properties of the respective cell type. By specifically modifying a distinct subpopulation of the leukocyte population, the T-lymphocytes, their identification in whole human blood was successfully demonstrated. In the field of human blood analysis by EIC, Han and co-workers[42] demonstrated a combined EIC setup and cell lysis geometry later in the year 2011. Here, human whole blood was initially purified from its erythrocyte population by application of a special lysis buffer protocol in microfluidic environment, followed by detection of the various subfamilies of leukocytes, comparable with the previous approach using a double detection and the opacity of the measured impedances. By comparison with hospital cell counts, the characterization of the used blood samples was in good agreement.

Furthermore, EIC was utilized for differentiation and identification of micron-sized single cell organisms. For instance, Haandbæk and co-workers[43] demonstrated successful differentiation of the genotype of yeast cells by EIC. Here, two pairs parallel facing microelectrodes were utilized to detect single yeast cells in a confined liquid stream in a microfluidic channel. By application of high-frequency signals around 250 MHz, probing of the subcellular morphology became possible, successfully describing differentiation of wild type and mutant yeast cells. In addition, they demonstrated later in 2016 their sensor's sensitivity not solely on the analyte's genotype, but also its phenotype. In this, yeast cells replicate themselves by formation of budding cells, attached to the parent cell during DNA replication. In this, the presence and the orientation of the budding cell, when the parent cell is passing the sensor, gave rise to distinguishable impedance signals of the sensor, proved by a double detection using image capturing by a high-speed camera[44]. Furthermore, in the spirit of single-cell detection using EIC, detection of parasitic protozoa based on species and viability was demonstrated in early 2017[45].

Finally, in the year 2017, Chiu and co-workers[46] successfully detected several species of circulating tumor cells (CTCs), namely haptic, oral and lung CTCs. Basically describing a Coulter Counter (see *Chapter 2.3.2*), the cells are pushed through a thin microfluidic constriction tube, while the impedance is measured in liquid by electrodes prior and after the orifice. Finally, even maturation of mesenchymal stem cells and their abundance compared to their adult cells, the osteoblasts, in dependence of the time has been demonstrated[47]. In the following table, a short overview of latest achievements in the research field of the impedance cytometry can be seen.

Table 2: Authors, year of publication and the detected biological species of state-of-the-art achievements of impedance cytometry during the last decade

Authors	Year of Publication	Detected species
Holmes et. al.[40]	2015	Leukocyte sub-populations
Haanbaek et. al.[44]	2016	Single yeast cells
McGrath et. al.[45]	2017	Parasitic protozoa
Chiu et. al.[46]	2017	Circulating cancer cells
Song et. al[47]	2016	Mesenchymal stem cells

1.3 Scope of this thesis

The main goal of this work is dedicated to the development and technical improvement of nanoscaled sensing platforms for various types of analytes ranging from molecules to whole cells. Depending on the appearance of the analyte of interest, two main approaches were considered including prototyping, evaluation and optimizing of technological efforts in SiNW FET and EIC biological and chemical sensing.

The aim of this work is organized into two main parts, where the first part deals with the integration of droplet microfluidics in FET technology. Till now, there are no investigations in this direction and detection of various analytes was either carried out by pipetting liquid drops on the sensor area or delivery of analyte liquid using microfluidic single phase liquids. Here, the separation of analyte solution into distinct nanoliter regimes opens the route towards higher sensitivity to analytes at low concentration by minimization of interactions of dispersed liquid to channel walls (due to channel wetting of the continuous phase) and related contaminations. Second, changes in the liquid environment, *e.g.* molar concentrations of ions or pH value changes induced by chemical reactions, become traceable by dramatically decrease of the analyzed volume. Third, in the spirit of miniaturization and automatization, droplet microfluidics is an excellent tool to detect analytes in ultra-small volumes, mimicking several working steps in the laboratory by droplet fusion, incubation and splitting at ultra-high throughput. Finally, up to now, microfluidic droplets are mainly detected using optical detection schemes, *e.g.* by fluorescence, and therefore require bulky detection devices which can lead to possible false analysis by introduction of secondary detection molecules[48–51]. Combination of SiNW FETs and droplet microfluidics opens the route towards label-free sensing of miniaturized droplet environments.

Further, EIC has been proven to evolve into a miniaturized version of conventional flow cytometry without the need of bulky devices and labeling, while reducing costs and effort in this field. Here, no investigation towards nanogeometries as sensing element has been made till now. The replacement of microelectrodes with nanoelectrodes allows to boost the sensitivity of EIC devices to a new level, making it competitive to state-of-the-art laboratory biological and biomedical techniques and assays. The second part of this work is dedicated to develop a novel prototype of a chip suitable for EIC using nanosensing elements. After the introduction, the thesis is composed of 5 chapters:

The 2nd chapter will cover the theoretical background of the methodologies of semiconducting electrical building blocks, metallic capacitive sensing and microfluidics for better understanding of the following chapters. Here, the focus will be on the working mechanism of MOSFETs (metal-oxide-semiconductor field effect transistor) and ISFETs (ion-sensitive field effect transistor) and the reduction of the sensing area from the micro- to the nanodimension. For metallic capacitive sensing, the chapter will demonstrate basic definitions and application towards biosensing. The main focus is set on the development of EIC devices. Further, an introduction to biologically and medical relevant physical and chemical sensing parameters, related to this work, are presented.

The 3rd chapter will cover the experimental procedures and protocols for the development of the novel sensor platforms, mainly focusing on surface patterning for fabrication of nanowires and microelectrodes. Additionally, it explains the concept of the various laboratory fabrication techniques of micropatterns for microfluidic integration into channel geometries.

The 4th chapter demonstrates the results on the conjunction of SiNW FET and droplet microfluidic technology. After demonstrating the proof-of-principle working mechanism using aqueous water droplet at different sizes and velocities, special attention is dedicated to the usage as a biosensor, namely its sensitivity towards pH values and various molar concentrations of passing droplets. The highlight of this work shows the successful demonstration of a label-free tracing of a chemical reaction of passing droplets on the sensor.

The 5th chapter is dedicated to the prototyping of a novel nanowire based sensor platform for EIC from scratch. Firstly, theoretical simulations using *COMSOL Multiphysics*® are presented to determine optimal nanowire geometries, their assembly and working conditions. Following, the strategy for fabrication is presented using electron beam lithography (EBL) and optical lithographic approaches. Special attention is drawn towards electrical characterization of the sensor, investigations of the sensor area on the sensitivity and its calibration using inorganic microparticles. The highlight demonstrates the successful label-free differentiation of healthy human PBMC cells and PBMC cells from a donor diagnosed with acute myeloid leukemia (AML). Further, a machine learning algorithm was developed for automated analysis and representation of obtained data. Finally, the limit of the developed sensor platform is explored using different bacterial strains.

The 6th chapter summarizes the work done in the two main topics of this thesis. Finally, conclusions and future prospects, based on the scientific work in this thesis, are done.

2 Fundamentals

This chapter explains the various methodologies used in this work. First, a detailed overview of the historical evolution of electrical building blocks, with the focus on transistor technology, from the microdimension to the nanodimension is described. Following, the working principles of transistor technology as an electrical building block is presented as well as their maturation towards utilization as sensing elements in current biosensors. Next, the history of impedimetric biosensors is presented with respect to the methodologies of *electrical impedance spectroscopy* (EIS) and *electrical impedance cytometry* (EIC) having their early beginnings in the late 1960s. After a detailed introduction of the microfluidic technology with special attention to multi-phase microfluidics (*i.e.* droplet microfluidics), an overview of the analytes, detected in this work, will be presented and why their detection is important for current societies.

2.1 Sensors at the nanoscale

During recent years, a broad variety of miniaturized sensing elements have been utilized to detect various biospecies, ranging from bacteria, eukaryotic cells and viruses to proteins and enzymes, DNA or gaseous molecules. In general, ISFETs/MOSFETs and capacitors enable label-free detection of various analytes, perfectly down-scalable on small feature sizes at very high numbers on a single chip. Here, the combination and interaction of differently doped MOSFET geometries (n-type or p-type) on a chip substrate is named *complementary metal-oxide semiconductor* (CMOS) technology, which is used to construct integrated circuits utilized in *e.g.* microprocessors and logic circuits[52]. One essential point in the development of novel sensors is the transition of CMOS geometries to nanoscopic devices, the nano CMOS technology. Firstly visionized by the famous talk “There’s plenty of room at the bottom” by Richard Feynman in 1959[53] and driven by technological progress in micro- and nanopatterning techniques during the last decades, the concept of miniaturization of electronic building blocks came more and more into focus of today’s research and industry interests. In 1965, Gordon Moore published an article, often referred as “Moore’s law”, stating a doubling of electronic components in an integrated circuit every year[54]. This law appears to be in good agreement with the evolution of transistor packaging, currently reaching 7 nm feature sizes[16] on industrial scale. Next to Moore’s law, the “More than Moore” law represents a central issue in scientific community, namely added values and incorporating functionalities next to their miniaturization.

In current research, in the development of novel devices and improvements of existing platforms, the trend goes towards miniaturization of electrical building blocks. Here, the transition from microelectromechanical systems (MEMS) to nanoelectromechanical systems (NEMS) and CMOS technology in academic research and industry describes a major step in platform optimizations with respect to low power consumption, density of building blocks on a surface (following Moore’s law), scalability and accompanied higher device performances[24,55,56]. In biological and biomedical research and development fields, the research area of point-of-care (POC) diagnostic is coming more and more into focus. Apart from already commercial non-nanosized handheld devices, application of functional nanosensing geometries grants higher sensitivity and selectivity towards analytes due to enhanced surface to volume ratio and strong electric field enhancement at the nanostructures at low power consumption[57]. In this, research concentrates on different kinds of nanogeometries, e.g. nanoparticles[58], nanowires[25], nanorods[59], nanotubes[60] and nanosheets[61]. This combination of features, granted by nanosensing geometries, packaged into a space-saving device which allows easy transportation, can boost the field of point-of-care diagnostic to the next generation. In this, detection of biological or chemical species is due to specific binding of the analyte on the sensing geometry via immobilized receptor molecules, like antibodies, aptamers, single-stranded DNA or RNA, enzymes and microorganisms[62–64], or due to changes in the physical and chemical surrounding of the sensing element[65,66]. Via interaction of the analyte with the receptor, the properties of the sensor are changed which can be transduced to an electrical signal. A broad variety of nanosized sensors were described where the macro-sensing geometry was either transferred to the nanodimension or even whole laboratory protocols were transferred on a chip. For instance, utilization of nanosized elements was demonstrated in the research fields of surface-plasmon resonance (SPR)[67], cantilever sensors[68], surface enhanced Raman scattering (SERS)[69] and fluorescence resonance energy transfer (FRET)[70], thereby demonstrating low detection limits at low volumes.

In summary, the transition from state-of-art laboratory techniques and protocols and micron-sized devices to the nanodimension dominates today's research in the point-of-care diagnostics granting low detection limits at low volumes as well as high density of sensors on transportable platforms at low power consumption and less effort of sample preparation.

2.2 Transistors technology

Transistors (from the terms **trans**fer and res**istor**[71]) are semiconducting building blocks allowing the control of electrical currents and voltages. Nowadays, transistors are the fundamental building block in all modern electronic devices, *e.g.* computer systems, power electronics and circuit technology. In general, transistors are made of a semiconducting material, most commonly silicon, with a minimum of three terminals, where the electric potential or current of one terminal controls the electric current between the other pair of terminals. In current electronic standards, different types of transistors are used for various types of applications[72]. In order to understand the working mechanism of transistors, the following paragraph will initially deal with the principle of p-n junctions, representing the fundamental working principle in transistors. Further, the working mechanism of the different types of electronic building blocks based on the principle of p-n junctions will be explained, putting the focus on the of MOSFET and ISFET architecture.

2.2.1 p-n junction

A p-n junction represents the interface between differently doped types of a semi-crystalline material, *i.e.* n-type (excess of electrons, *e.g.* phosphorus) and p-type (excess of holes, *e.g.* aluminum) in silicon. During impurity doping processes, foreign atoms are implemented into the intrinsic semiconducting material by ion implantation or diffusion processes[73]. In intrinsic silicon crystals, foreign atoms like phosphorus and aluminum atoms can be introduced selectively into the material to create n-type and p-type regions, respectively. In this, at the surface region between n-type and p-type regions, electrons from the n-type region tend to diffuse into the p-type region, filling the holes and thus creating negative ions. In contrast, holes diffuse into the n-type region, forming positive ions by recombination. The depth of electron and hole diffusion and recombination and the formed electric field is also known as *depletion layer* or *space charge region*[72] (see Figure 1, panel A). So, no electric current flow is possible crossing the p-n junction, thus acting as an electrical barrier for electrons.

In total, several strategies of electrical contacting the p-n junction opens the route for a wide variety of electronic building blocks. In the following, only a very narrow selection of potential electronic geometries will be described, namely the MOSFET and ISFET.

2.2.3 The MOSFET

The MOSFET represents one of most common transistors in digital circuits and is a type of field-effect transistors (FET). It consists of differently doped conducting bulk material regions with ohmic contacts applied to different potentials (S: source and D: drain). Here, lateral electric current between source and drain is controlled by a vertically controlled electric field via a third terminal, the gate (G). In the case of MOSFETs, the gate terminal is additional isolated by an oxide layer, *e.g*. Al_2O_3 or SiO_2 (see Figure 1, Panel B), from the bulk. In this, different bias on the gate electrode leads to accumulation or depletion of electrons or holes at the semiconductor-oxide interface, depending on the doping of the semiconductor, thus allowing formation of a conducting channel between the source and drain terminals[72]. This effect is dedicated to the geometry of the controlling electric field, generated by the metal-oxide-semiconductor (MOS) capacitor. For further description, the focus will be set on the characteristics of a n-channel MOSFET. Here, if a positive bias is applied to the gate electrode (V_{GS}), electrons from the bulk p-substrate are attracted to the interface to the isolating oxide (forming the *accumulation layer*) and vice versa for negative bias of V_{GS} forming a *depletion layer* at the interface layer. Additionally, if V_{GS} is further increased in the negative regime, the concentration of interface-near holes might surpass the concentration of electrons. In this case, the charger carrier type of the semiconductor changes and the MOSFET is working in *inversion mode*. By application of a positive bias to the gate, the n-channel MOSFET shows electric current (I_{SD}) at an applied voltage (V_{SD}) between the terminals if the gate bias is set above a certain threshold voltage ($V_{GS}>V_T$) due to electron trapping in unoccupied states between the oxide and bulk materials, driven by one type of charge carrier, since no p-n junction has to be crossed. MOSFETs represent a type of non-linear electronic building blocks, meaning they have no linear correlation between applied electric voltage and observed current of all three terminals[72]. Here, in the IV characteristic of V_{SD} and I_{SD} a clear saturation

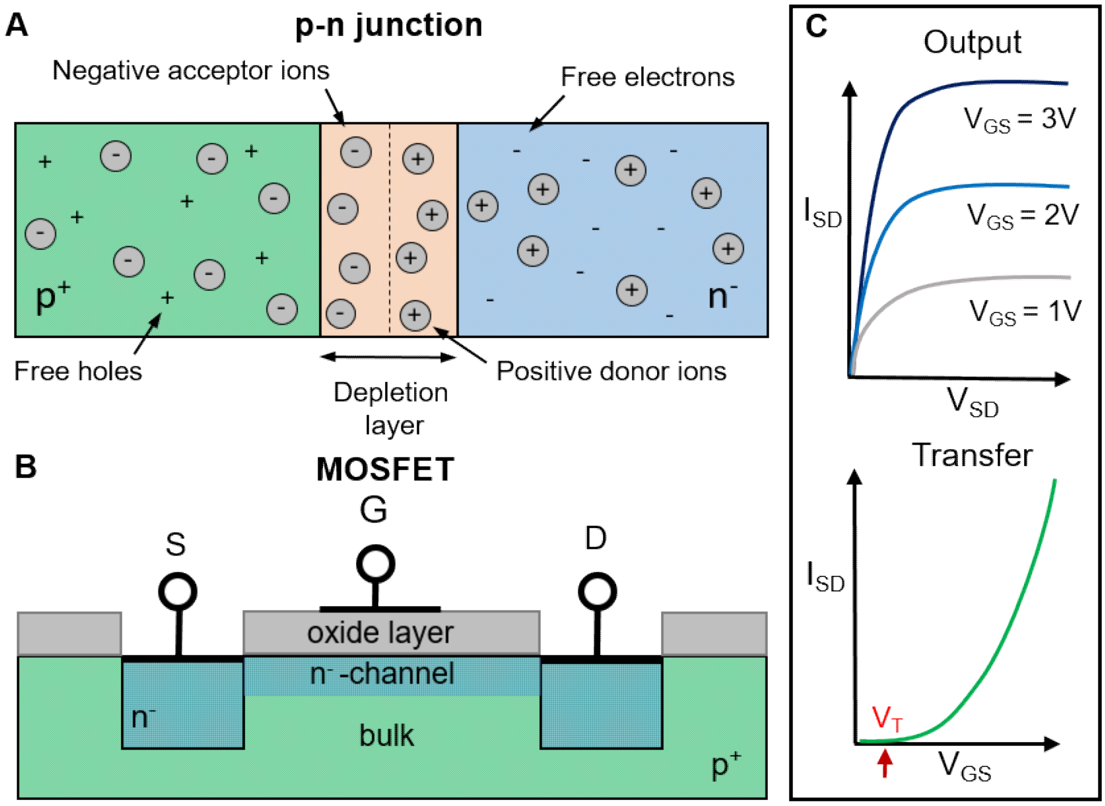

Figure 1: Overview of differently doped semi-crystalline regions and their possible working areas: **(A)** The p-n junction: At the interface between differently doped regions, a depletion layer is created by diffusion of both electrons and holes to the opposite region, thereby recombining with each other. Fixed lattice ions are creating in the layers. **(B)** n-channel MOSFET side view appearance: The MOS capacitor or gate (G) regulates the width of the conductive channel and therefore the current between source (S) and drain (D). **(C)** Schematic illustration of the output characteristics of a n-MOSFET in dependence of different gate voltages (top) and of the transfer characteristic (bottom).

level can be observed at constant V_{GS} values, also called the *output characteristics* of a MOSFET. This saturation is due to a decreased conduction channel width at the drain electrode, since this width is based on the potential difference between the gate and the channel. Here, linear increase and saturation level formation is dependent on the *transfer characteristics* (I_{SD} in dependence of V_{GS}) of MOSFET, in detail only possible if $V_{GS}>V_T$, which appearance is set by the conduction type of the transistor[74]. In the following Figure 1, panel C, the schematic electrical behavior of a n-type MOSFET can be seen. Here, the transfer characteristics show a positive current of I_{SD} for positive gate voltages, if V_{GS} exceeds the threshold values V_T. Further, a linear and ohmic current increase of I_{SD} in the output characteristics can be observed, followed by a saturation with increasing V_{SD}. Here, the plateau signal is greatly dependent on the gate voltage and the respective width of the conduction channel.

2.2.4 The ISFET and BioFET

MOSFETs are vastly used in computer industry due to their ability to switch their on-off state by external potentials (namely V_{GS}) and can thus be utilized as electrical element for logical operations (*e.g. OR, AND* and *XOR*) in very large scale integration (VLSI) integrated circuits[75]. In parallel, FET technology rose in the last decades as sensing element for biological and chemical species in the current field of biosensors, the *BioFETs*. In this paragraph, the principle of the utilization of these FETs for biosensing will be described. Next to MOSFET technology, where the gate electrode is separated by an isolating oxide layer from the conduction channel, several strategies exist for control of the conduction channel width. Among others, BioFETs represent a potentiometric sensor geometry where the detection principle is based on potential differences between the working electrode and gate electrode. In this, the MOSFET's capacitor control can be replaced by the utilization of an electrochemical gating effect *in solution*, applied for devices called ISFETs. Here, two main configurations are present: 1) ISFET with dielectric insulator, where the capacitive coupling is mainly due to the gate dielectrics and 2) ISFETs without isolating layers, where the coupling is dominated by the creation and composition of the capacitance of the electrical double layer (EDL). This effect is solely due to ion redistribution of the solution near the semiconductor surface and is labeled as the electrical double layer capacitance (EDLC) (see Figure 2, panel A). In this configuration, ISFETs are suitable to be utilized as biological and chemical sensors, since the EDLC (and its effect on the conduction channel width) is sensitive to the solution ion

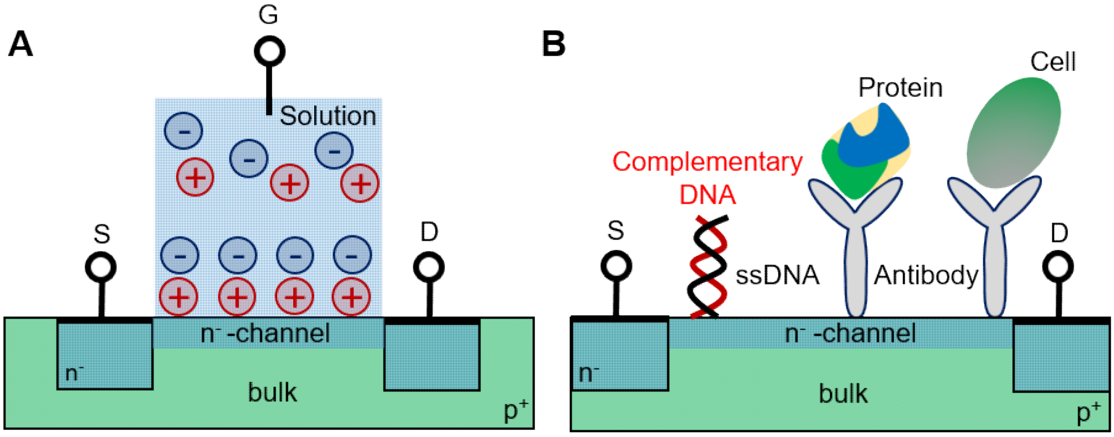

Figure 2: Utilization of BioFETs for biosensing. **(A)** Appearance of the electrical double layer capacitance (EDLC) by accumulation of positive charges at the semiconducting surface (V_{GS}: positive). **(B)** Functionalization of the surface with receptors (ssDNA or antibodies) grants selectivity to biospecies, *e.g.* complementary DNA, proteins or cells.

concentration (and thus its pH value). Furthermore, via functionalization of bioreceptors (*e.g.* DNA, antibodies and aptamers) to the semiconductor surface and the selective binding of the analyte of interest (*e.g.* cells, proteins and complementary DNA) lead to alterations of the EDLC, directly reflected in the conductivity of the channel (see Figure 2, panel B)[76–78]. During the last decades, a great number of publications were published demonstrating the usage of ISFETs for sensing specific analytes in medium, giving it the name BioFET. Here, by functionalization of the surface, detection of cells[79] (or their medium alternating metabolism, discussed in *Chapter 2.5.2*), proteins[80], molecules[81] and DNA[78] were successfully demonstrated. A major improvement towards sensitivity marks the implementation of nanoscaled semiconducting materials, as discussed in *Chapter 2.1*, with a broad variety of 1D materials (nanowires, nanotubes) and 2D materials (nanosheets), including silicon nanowires[27], graphene[82], molybdenum disulfide (MoS_2)[83], carbon nanotubes[84] and indium oxide nanowires[85].

2.3 Impedance measurements for biodetection

2.3.1 Electrical impedance spectroscopy

Electrical Impedance Spectroscopy (EIS) represents a powerful and non-invasive technique for electrical characterization and sensing of molecules and micron-sized analytes, utilized in *e.g.* food products analysis[86], medical diagnostics[87,88], quality control of electronic structures[89,90] and coatings[91]. In this technique, the detection is based on alterations of dielectric properties of electrical systems in alternating currents at various frequency ranges. Usually, these systems are composed of both resistors and capacitors[92] with up to four electrodes, where the applied frequency depends on the main goal of the experiment, ranging from the µHz regime for corrosion measurements up to several MHz in biological assays[93]. Most important in (bio)medical context, EIS can be utilized to detect adhering or growing biological species on electrode surfaces. Here, the biological biomass or biofilm with its own electric properties (*i.e.* resistance, capacitance and dielectric constant) forms a coating film on or between electrode surfaces thereby altering the electronic response of the circuit[94,95]. Furthermore, the presence of biological species can be additionally detected by alterations of the ionic environment by secretion of ions or metabolites from living bacteria and cells[96]. Despite its high sensitivity towards changes on and around the electrodes, the *static* detection mode of EIS limits the technology to long-term investigations, *e.g.* in cell culture experiments or slow settling of microorganisms on the surface. Thus, in order to increase the information throughput, *dynamic* mode sensing at fixed frequencies will be introduced in the following paragraph.

2.3.2 Electrical impedance cytometry

In addition to EIS, the frequency can be set to concrete states, introducing the electrical impedance cytometry (EIC) principle. In this, application of *e.g.* microfluidic delivery systems and fixation of the excitation frequency greatly improves the throughput, mimicking the flow cytometry principle. Like in EIS, this technique probes the dielectric and impedance properties of both biological and non-biological analytes applied by an externally electrical field between two electrodes[97]. Here, the single-shelled spherical model can be used for theoretical approximation of the output impedance response, describing the analyte (*e.g.* particle or cell) on the capacitive sensor, represented by a parallel RC-circuit, by its inner electrical resistance and capacitance (see Figure 3, panel A). Based on this model, the presence of a cell or particle on the sensor can be represented in the equivalent circuit as a parallel RC element connected to the original sensor equivalent circuit (see Figure 3, panel B). The in-series connected capacitance C_p and resistance R_p of the analyte will introduce a change in the impedance characteristics of the circuit. Here, this model has been proven to be correct being in good agreement in terms of single cell impedance cytometry experiments[98,99].The first demonstration of a device able to detect and count single cells was developed by Coulter in 1956, giving it the name Coulter counter, where blood cells were guided through a small orifice with an applied electric current[100]. While cell passing, the change of resistance was recorded based on the size of the passing cell and the resulting displacement of the electrolyte solution. Around 30 years later in 1997, the first realization of the Coulter counter

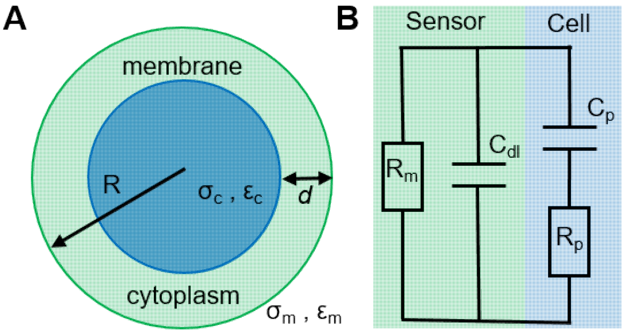

Figure 3: EIC basic principle: **(A)** Biological cell representation by the single shell model with radius R, membrane thickness *d*, cytoplasm and membrane conductivities σ_c and ε_c and dielectric constants and σ_m and ε_m. **(B)** Simplified equivalent circuit in the presence of a cell. The cell adds a parallel RC-element with cell specific values in series to the original sensor equivalent circuit.

on the micron-scale was demonstrated, namely the microchip Coulter Particle Counter (µCPC)[101]. Although no data was presented in this work, the device design consisted of a silicon-etched microchannel, vertically focusing the analyte liquid through a gold-based orifice. Based on this work, successful detection of sub-micrometer particles was demonstrated using the Coulter Counter technique several years later by Saleh and Sohn[102]. Here, latex particles down to 87 nm were detected as they pass through a small orifice thereby displacing the electrolyte solution. During the last decades, the concept of µCPC was further improved with respect to sensitivity, downscaling of the orifice to the nanoscale and throughput towards instruments capable of single molecule detection and DNA/RNA sequencing[103].

While µCPC relies on direct current and low-frequency for size measurements, the strategy of measuring in alternating current at various frequencies offers an alternative way to measure, next to the size, the membrane capacitance and cytoplasm resistance of passing cells, called *electrical impedance cytometry*[38]. This improvement was firstly demonstrated on chip in 2001, capable of differentiation of micron-sized particles and erythrocytes (red blood cells) and their ghost cells (removed inner content of the cells) between two coplanar microelectrodes[104]. In the last 20 years, the principle of EIC was further optimized with respect to enhanced sensitivity and stable signals by reduction of detection area by focusing liquids[105] and squeezing cells through microfluidic channel bottlenecks[106,107]. Furthermore, information output was additionally improved by application of a two-frequency impedance data collection of passing single cells allowing determination of membrane capacitance and cytoplasm conductivity independently[108] or as a ratio (*i.e.* the *opacity*) to demonstrate alterations in the cell membrane[40]. In conclusion, EIC provides high-throughput detection of organic and inorganic nano- and microspecies based on their electric properties like membrane capacitance and cytoplasm resistance but is still influenced by the analyte's size and the experimental setup, *i.e.* the electrodes and the microchannel design. However, Zhao and co-workers[109] successfully demonstrated classification of cells based on their membrane capacitance and cytoplasm conductivity using a constriction channel, but at low detection frequency (around 1Hz). Here, further investigations have to be done in order to combine the detection of the pure electric properties of the cells at the high-throughput kHz regime. Further, in order to be able to successfully classify the different development states of cells, *e.g.* stem cells, further electrical characterization of the different progenitor cells have to be done since their capacitance can alter during maturation[110,111]. Finally, there are no investigation towards the utilization of nanosized electrodes as detection elements, which can enable a more sensitive detection of cells with different intrinsic electrical properties (*see Chapter 2.1*).

2.4 Microfluidics

2.4.1 Definition

Microfluidics represents a technology for controlling and manipulating liquids (in the range of 10^{-10} to 10^{-18} liters) in confined channel geometries typically sizing from tens to hundreds of micrometers. These channel systems offer several advantages in both chemical and biological assays compared to conventional laboratory devices, *e.g.* short analysis times, low sample consumption and costs and parallel operations at high sensitivity and resolution[112–114]. Here, dominating forces in macroscopic fluids like inertial forces, gravity or turbulent forces, are dominated by laminar flow, diffusion, surface tension and surface area to volume ratio[115,116]. In this, the transition from turbulent flow to laminar flow can be described by the Reynolds number (*Re*). The dimensionless number describes the ratio of inertial and viscous forces of a fluid and is defined by:

$$Re = \frac{\rho v d}{\eta} \tag{1}$$

with ρ as the density of the liquid with velocity v in the length dimension d divided by the dynamic viscosity η of the liquid. Subsequently, if inertial forces, described by the nominator, dominate over the viscous force, described by the denominator, the system becomes turbulent ($Re > 2300$). In contrast, for shrinking influences of inertial forces, *e.g.* for smaller channel dimensions d or slower velocities v, the system becomes laminar ($Re < 2300$)[115]. In microchannels, the liquid flow usually shows laminar behavior, demonstrating parallel stream layers to the surface, where mixing only occurs by diffusion or introduction of special geometries[112,115,117]. Here, the fluid flow can be obtained passively by capillary and evaporation phenomena[118,119] or actively by manipulation of the flow by active pumping of the liquids[120,121]. Nowadays, microfluidics represents a powerful tool in multidisciplinary fields, *e.g.* in (bio)chemistry, biotechnology, biomedicine and nanotechnology in the spirit of drug screening assays[122,123], analyte and sample delivery to sensing structures[124–127] and direct sensing[128,129]. By tuning of the channel system, additional features can be inserted into the microfluidic system, *e.g.* mixing of analytes by structures inducing turbulent flow[130], focusing of liquid streams[131] or separation of the analytes or particles in the channel by droplet formations. In current research, the most prominent structures are the *flow-focusing* and *t-junction* structure, where two immiscible liquids are guided to the systems enabling the formation of a controlled emulsion in the following channels[51]. The principle and the theory of droplet formation or stream breakage are described in the following paragraph.

2.4.2 Droplet-based microfluidics

Droplet microfluidic deals with the formation and manipulation of droplets in an immiscible carrier liquid in microchannels. Over the last years, by the possibility of encapsulation of biological species or chemical components in these droplets increases its impact as an alternative route in various biological assays by its ultra-small volumes (in the range of pico- and nanoliters), automatization and parallelization possibilities at high-throughput (up to several kilohertz)[50,132,133]. In this configuration, every discrete droplet can be seen as an *e.g.* individual well in a microtiter plate including the possibilities of sample processing. In detail, droplet mixing[134], controlled fusion or merging[135], splitting[136] as well as long-time storage of microfluidic droplets[137] has been successfully described and, due to its high-throughput, drastically increases the data output for biological and chemical assays at low experimental times and costs. Next to parallelization and miniaturization, this methodology offers additional advantages compared to single-phase flow microfluidics, namely enhanced mass transfer and mixing within droplets, higher sensitivity due to lower volumes and thus shorter times in general for analysis and detection assays[51,133]. Droplet generation can be categorized into two main categories, *i.e.* active and passive generation. In passive mode, droplets are generated by introduction of a liquid phase in an immiscible continuous liquid, thereby destabilizing the continuous flow, *i.e.* by dripping, jetting, squeezing, tip-streaming and tip-multi-breaking[138]. In contrast, in active mode the natural breakup of droplets can be influenced by introduction of external forces like electrical, magnetic or thermal factors[51]. In the following, the forces, influencing parameters and appearance of passive droplet generation geometries, are described in detail for two most common droplet microfluidic structures, the flow-focusing structure and the t-junction (see Figure 4, panel A and B). For simplicity, the dimensions of all channel structures are set to the same values in the following examples, namely their heights and widths. In the flow-focusing structure a liquid, *e.g.* deionized water as the dispersed phase, is actively pumped from the left microfluidic channel with a flow velocity Q_d. Additionally, an immiscible liquid, *e.g.* mineral oil as the continuous phase with the flow velocity Q_c, is pumped through the channel coming from top and bottom (see Figure 4, panel A). In this 3-channel configuration, the dispersed phase is phase is squeezed between the two flows of the continuous phase, resembling a hydrodynamic focusing effect. Following, as the dispersed phase propagates in the channel, it forms a cylindrical shape thereby becoming unstable by capillary instability, firstly described by Rayleigh in the year 1879 and thus labelled *Rayleigh-Plateau instability*[139,140]. Subsequently, the breakup at the neck of the emerging droplet takes place driven by inertia and surface tension. In this, the size of the droplet is dependent on the flow rates and viscosities of the two liquids as well as the channel geometry[141]. A closer look at the second droplet generation structure, the t-junction, allows clear identification and determination of the different physical forces which contribute to the droplet formation. Here, the geometry is a simple 2-channel geometry, where the dispersed phase is pushed

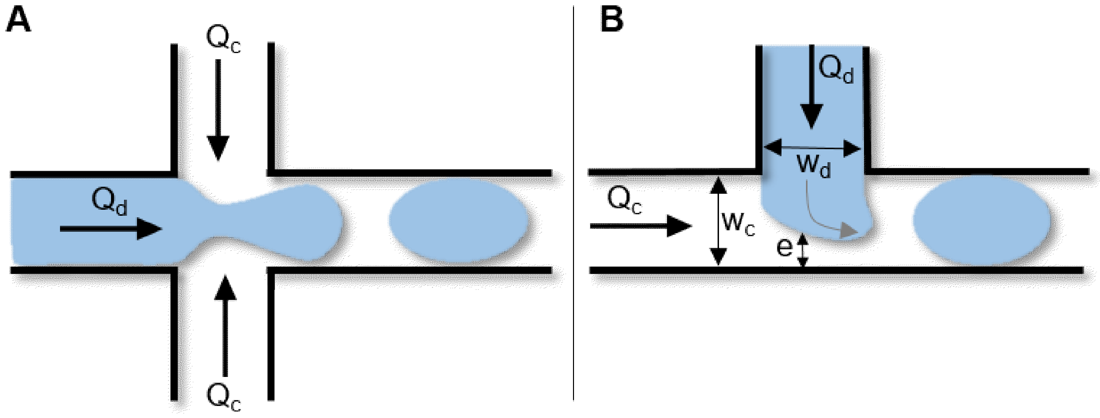

Figure 4: Most common droplet microfluidic geometries: **(A)** Flow-focusing structure: The dispersed phase (blue) with the velocity Q_d is squeezed between two streams of immiscible continuous liquid phase with the velocity Q_c. By occurring capillary instabilities during dispersed phase, a cylindrical shape is formed which is following cut by inertia and surface tension forces. **(B)** T-junction structure: As the dispersed liquid is penetrating into the channel with the continuous liquid, a combination of surface tension force, shear stress force and flow resistance force result in droplet fission and propagation in the downstream channel.

from the top while the continuous phase is pushed from the left (see Figure 4, panel B). In this, the dispersed phase penetrates into in the channel with the continuous phase, forming a droplet in the downstream direction. During dispersed phase penetration, its upstream interface of with the continuous phase is reaching the downstream edge of the dispersed phase channel, since the dynamic pressure upstream of the droplet is drastically increasing, resulting in droplet fission. As soon as the dispersed phase penetrates into the channel with the continuous phase, the combination of different forces starts to act on the dispersed phase, resulting in droplet breakup. Firstly, as the droplet's stabilizing force, the surface tension force is introduced:

$$F_{\gamma} \approx \gamma \mathrm{h} \tag{2}$$

where γ is the interfacial tension coefficient and h the height of the channel. Next, the destabilizing shear stress force on the dispersed phase tip, exerted by the continuous phase as it flows through the gap between the tip and opposing channel wall, is defined by:

$$F_{\tau} \approx \mu_c Q_c \frac{w_c}{e^2} \tag{3}$$

where μ_c is the viscosity of the continuous phase, Q_c the speed of the continuous phase, , w_c the width of the carrier channel and e the thickness of the gap between droplet tip and opposite channel. The second destabilizing force, the flow resistance force, describes the resistance to the flow of the continuous phase when the dispersed phase blocks the cross section of the channel, defined by:

$$F_{\mathrm{R}} \approx \mu_c Q_c \frac{w_c^2}{e^3} \tag{4}$$

In summary, during droplet formation in t-junction geometries, two destabilizing forces for droplet breakup and one tip stabilizing forces are present. Here, the destabilizing forces F_{τ} and F_{R} have different temporal impacts in the formation. While F_{R} has a higher impact in the net force acting on the droplet, when it is penetrating into the main channel, the impact of F_{τ} increases more during droplet maturation, when the thickness e is decreasing and the droplet is moving within the main channel[141–143].

2.5 Biomarkers for sensing applications

In the following paragraph, the probed chemical parameters and biospecies in the spirit of biosensing experiments are presented. Here, detection of chemical parameters like the pH value of a medium or ionic concentrations of buffers can be utilized to identify metabolism of living microorganisms and to track the kinetics of a chemical reaction leading both leading to time-dependent alterations of the ionic composition of the medium. The utilization of the pH value and ionic concentrations in sensing experiments will be discussed in detail in the following paragraph. Additionally, a compact overview of one family of leukocytes are presented and why their detection and accompanied composition analysis has a high impact in the fields of biomedicine and medical assays.

2.5.1 Peripheral blood mononuclear cells (PBMCs)

Every higher-developed living organism has a developed system, namely the immune system, for defense against pathogenic intruders which enter an organism through its interactions with the environment. In humans, this system consists of two different branches: The static innate non-specific immune system and the adaptive immune system having high specificity and memory against pathogens. In both branches, all cells (also called leukocytes) of the immune system develop from a shared omnipotent stem cell in the bone marrow[144]. During development, two ways of cell differentiation can be observed: the myeloid development of *e.g.* granulocytes and monocytes, which main task is phagocytosis of pathogenic intruders. Second, T- and B-lymphocyte maturation, responsible for antigen recognition, can be found in the lymphoid development. In the following, the focus will be set on one family of immune cells, the peripheral blood mononuclear cells (PBMCs), which act in the adaptive immune response branch and consist of lymphocytes and monocytes. Lymphocytes consist of three populations: B- T- and natural killer (NK) cells. Here, the nomination is based on the spatial origin of differentiation, namely *Thymus* for T cells and *Bursa Fabricii* for B cells (only found in birds, located in the bone marrow in humans). The main task of B cells is the secretion of immune globulins upon recognition of the antigen thereby maturing in plasma cells. On the other hand, T cells are divided into several sub-groups fulfilling several tasks in the adaptive immune response, including maturation of B cells, activation of cytotoxic T cells, destruction of infected cells, immune response memory and many more. Further, NK cells have the task to activate cells of the phagocytosis system upon infection as well as destruction of virus-infected cells. Finally, monocytes are progenitors of macrophages, responsible for destruction of foreign pathogens as well as presentation of protein-antigens upon digestion[145]. Here, analysis of transcription and translation levels of PBMCs as well as their percentage composition of its subfamilies grant insight into the detection and identification of diseases, *e.g.* several types of cancer[146–148], infections[149,150] and various auto-immune diseases[151].

For instance, several types of leukemia, a type of cancer located in the bone marrow, can be detected by analysis of the PBMC subpopulations. The disease affects the composition, appearance and functioning of white blood cells causing a malfunctioning and weakened immune system with an increased risk of infections of the diseased person[152]. Over 350,000 new leukemia cases are estimated worldwide and it represents the 10th deadliest cancer type with over 265,000 deaths worldwide, most dominantly in developed countries[153]. The general origin of leukemia is mostly unknown and only few hypotheses try to point out the multiple factors, *e.g.* ionizing radiation and exposure to benzene and anti-cancer drugs[154]. Within the four main types of leukemia, *acute myeloid leukemia* (AML) represents the most abundant type with around 80% of cases[155] and is classified by a heterogeneous disorder caused by the loss of differentiation ability of haemopoietic progenitor cells[156] and accompanied reduced white blood cells count and performance[157]. Symptoms include anaemia, leukopenia und accompanied higher rate of infections. AML patients only have a five-year survival rate of 20-30%, strongly reduced for aged patients over 65 years even with clinical treatment[154,155].

2.5.2 Physical parameters

Next to detection of nano- and microscopic biological and molecular species, detection and determination of ionic concentrations, *i.e.* molar concentrations of ions and molecules as well as the pH value, represents a substantial liquid parameter with high biological relevance. In this, biological living and accompanied correct functioning of chemical reactions, metabolism, protein folding and interactions and enzyme function depend on the ionic concentrations of the surroundings[158,159]. Thus, precise determination of these liquid parameters plays an important role in biotechnology, biomedicine, pharmaceutics and biochemistry. Here, the pH value is used for determining the acidity or basicity of aqueous solutions, ranging from pH 1 (acidic) to pH 14 (basic) and is defined by the negative decimal logarithm of the hydrogen ion activity[160]:

$$pH = -log_{10}(a_{H^+}) \tag{5}$$

With respect to biological systems, the pH value both acts as a regulator and parameter in various fields. During development, maturation and metabolism of both eukaryotic and prokaryotic cells, chemical parameters of their surroundings play an important role in case of correct information pathways, induced changes of the surroundings during development or metabolism of the cells. For instance, the extracellular pH value, or the concentration of H^+ ions in a medium, has a dramatic effect on bacterial and fungi growth rates[161,162], metabolite production and consumption[161,163] and correct maturation of stem cells[164]. Next to the importance of the aqueous pH values, the molar concentration, or molarity, plays an important role for correct function of chemical reactions as well as survival conditions for biospecies in solution. It represents the concentration of a chemical in solution per unit volume ($\frac{mol}{L}$) and is defined by:

$$c = \frac{m}{VM_W} \tag{6}$$

Where m is the mass and M_W the molecular weight of the solute and V the volume of the solution. It is the driving parameter for the solution's compatibility to be suitable for cell incubation since it defines the osmotic pressure acting on suspended biospecies. Thus, if the ionic concentration of the solution is too high or low compared to the inner cell ionic concentration, bursting or shrinking of the suspended cell will follow[165]. Thus, precise determination of the molar concentration has to be done for correct incubation of prokaryotic and eukaryotic cells. Further, the molar concentrations of chemicals have to be precisely set in order to guarantee correct environment conditions for many chemical reactions.

In conclusion, detection of above mentioned liquid parameters represents an important technique to guarantee the successful operation of various laboratory assays in biomedicine, pharmaceutics and biochemistry. Additionally, these parameters define the survivability of microorganisms in suspension and thus efficiency of cell survival in biological assays as. Thus, determination of liquid parameters is substantial for a wide variety of scientific and industrial protocols, where their values have to be precisely set.

3. Material and methods

This chapter is dedicated to the introduction of the various experimental protocols used in this work. After a short overview of the used chemicals and their providers, the strategies for the cleaning of surfaces for later experimental procedures are presented. Following, the main focus is set on the various kinds of lithographic techniques, utilized for controlled patterning of surfaces from the nano- to the millimeter dimension. In this, the concept of electron beam, optical and soft lithography are introduced as well as the applied protocols used in this work. Following, experimental procedures subsequent to lithography are presented, *i.e.* thermal deposition of metals and surface silanization. Finally, after introduction of the general experimental measurement setup, the protocols for analyte cultivation, *i.e.* for bacteria and PBMCs, are presented.

3.1 General

3.1.1 Materials and chemicals

Table 3: Chemicals and Materials and their suppliers used in this work

Chemical / Material	Supplier
Acetone Isopropanol Ammonia solution (25%) Bacto nutrient broth	VWR International GmbH
Hydrochloric acid Sodium hydroxide (3-Aminopropyl)triethoxysilane (APTES) Succinic anhydride 1-Ethyl-3-(3-dimethylamino-propyl)carbodiimide (EDC) N-Hydroxysuccinimide (NHS) Disodium hydrogen phosphate Potassium dihydrogen phosphate BactoTM peptone Mineral oil M5904 Span® 80 Phosphate buffered saline (tablets)	Sigma Aldrich Inc.
Hydrogen peroxide (35%) Ethanol	Carl Roth GmbH + Co. KG

UV-resist AZ5215E	Merck KGaA
Developer AZ 351(B)	
Dimethyl sulfoxide (DMSO)	
Poly(methylmethacrylate) (PMMA)	Microchemicals GmbH
TI Prime	
Cr-Etchant	
UV-resist SU-8 2010	Microchem Corp.
mrDev 600	Micro resist Technology GmbH
Chromium rods	Goodfellow GmbH
Gold pellets	Kurt J. Lesker Company Ltd.
Chromium masks	ROSE Fotomasken
Sylgard® 184 (PDMS)	Dow Corning Inc.
Developer AZ726MIF	AZ Electronic Materials plc
Ficoll-Paque Plus	GE Healthcare SC
RPMI 1640 medium	Thermo Fisher Scientific Inc.
Fetal bovine serum	Invitrogen AG
PBMC antibodies	BD Biosciences Company

3.1.2 Surface cleaning

With respect to the required cleanliness of a surface or the appearance of unwanted influences of cleaning chemicals on deposited materials on a surface, substrates were washed in organic solvents, RCA cleaning solutions or in radical oxygen plasma. The individual procedures for different cleaning protocols are described in the following table.

Table 4: Cleaning procedures using different (combinations of) chemicals depending on the desired cleanliness of the substrate

Cleaning Procedure	Used Mixture	Duration	Temperature	Removes
Acetone / Isopropanol	Pure	5 min each	RT	organic contaminations
RCA-1	$H_2O:NH_4OH:H_2O_2 = 5:1:1$	15 min	80°C	organic contaminations
RCA-2	$H_2O:HCl:H_2O_2 = 7:1:1$	15 min	80°C	metallic contaminations
O_2 plasma treatment	-	10min	RT	organic contaminations

3.2 Lithography

Common lithography in nano- and micropatterning approaches have the aim to pattern an artificial structure on the substrate. These structures hold various kinds of applications, *e.g.* electrode geometries, sacrificial layers for lift-off strategies of metals, etching masks or master structures for soft lithography. In the following subsections, the experimental procedures of different lithography approaches are described. Prior to covering, the substrate was cleaned according to the needed cleanliness and compatibility with the cleaning reagents, described in the previous paragraph.

3.2.1 Electron beam lithography

Electron beam lithography (EBL) is a technique for nanostructuring electron beam sensitive layers down to sub-10 nm dimensions and is based on the scanning electron microscope (SEM) technique. In this, SEM represents a mapping method, which uses electrons for visualization of a specimen instead of the usage of photons, utilized in optical microscopy. During visualization, the specimen is scanned with an electron beam, emitted from a field emission source or thermally heated cathode, accelerated to an energy usually in the range of single kilo-electron volts (keV) and focused by electromagnetic lenses[166,167]. While in conventional SEM technology, the electron beam is scanned over the specimen, EBL allows the guidance of the beam in arbitrary patterns, thus only exposing specific areas.

Here, the specimen, usually a planar substrate coated with an electron-sensitive layer, is exposed to a focused electron beam (accelerated up to 100keV[168]) in an arbitrary pattern. By this partial exposure, the exposed areas are chemically modified, drastically altering their solubility. Here, the layer (*i.e.* resist) becomes either soluble (positive tone) to its developers or chemically resistant to its removal agents or developers (negative tone) during its exposure. Since the pattern is directly written in the resist, EBL represents a *maskless* nanopatterning technique[167]. The patterning of these small features requires consideration of several experimental parameters, since the resolution of generated patterns is a combination of various factors. On the one hand, the quality of patterns is greatly dependent on correct focusing of the electron beam, as well as high positional accuracy. While these device-related issues are nowadays covered by commercial automated EBL systems[169], unavoidable electron scattering events in the resist can influence the resolution of the pattern, namely the *proximity effect*[168]. This effect is due to interactions of beam electrons with both resist and substrate, namely scattering of primary electrons, backscattered electrons and induced diffusion of secondary electrons[170]. Here, the magnitude of scattering and diffusion events is greatly dependent on the electron acceleration voltage, beam dose on one spot (settling time of the beam), beam current, thickness of the resist and substrate material. Thus, the optimal parameters for a high-yield and high resolution patterns have to found empirically since the delicate combination of all these parameters is hard to predict. During the last decades, various theoretical and experimental investigations were made trying to explore, understand and minimize the electron scattering in a range possible parameter combinations[170–173]. During application of EBL, the fabricated structure can be used as a mask to transfer its features to other materials, depending on the type of utilized resist on the substrate. In this, negative resists on a surface can be used as an etching mask to directly transfer the structure to underlying materials, while positive resist can be utilized as sacrificial layer to pattern the exposed parts of the substrate after development, *e.g.* during metal lift-off methods (see Figure 5). There is a broad range of commercial available EBL resist from which the

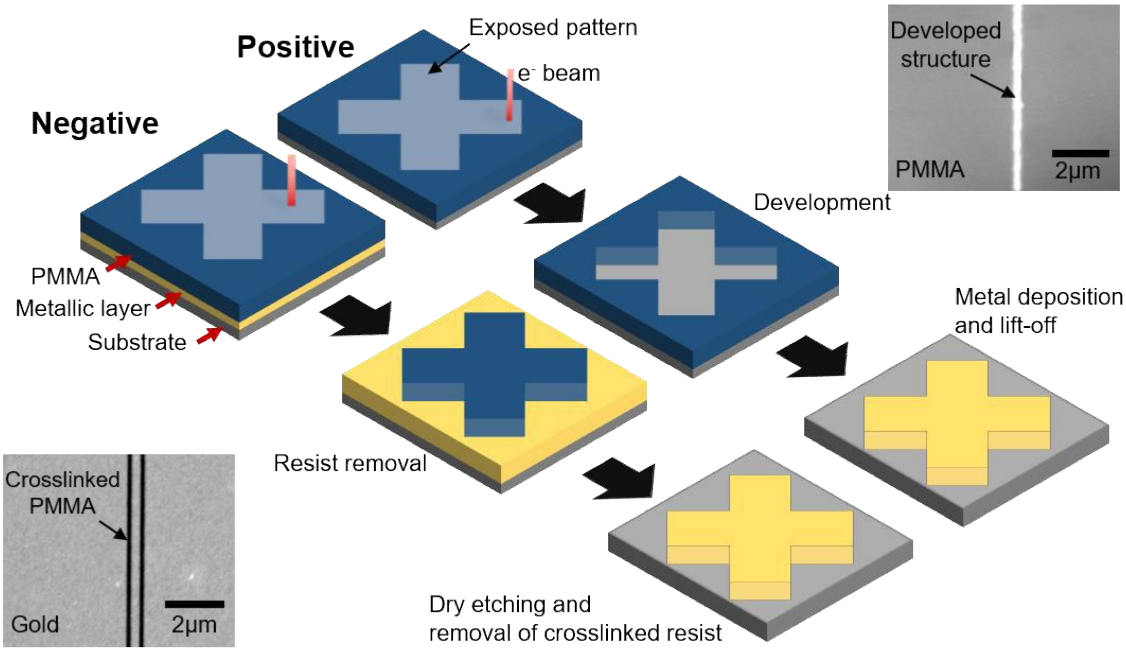

Figure 5: PMMA negative and positive tone behavior. During exposure, both processes of chain cross-linking and chain scission take place. For lower energy, chain scission dominates, rendering PMMA positive during exposure (top path). The resulting pattern can be used in *e.g.* metal-lift off processes. For higher beam energy, chain crosslinking becomes dominant, switching the response of PMMA to negative tone (bottom path). The crosslinked layer can be used as *e.g.* etching mask for underlying layers.

most suitable can be chosen for experimental work with respect to tone, resolution, thicknesses, etch resistances and many more[174,175]. In the following, one of the most prominent EBL resist, Poly(methylmethacrylate) (PMMA), will be introduced. The polymer PMMA is a positive high-resolution and easy to process organic resist which feature sizes reach down to 5 nm[176,177]. During electron beam exposure, PMMA undergoes simultaneously chain crosslinking and chain scission, where the latter dominates the process and thus leads to a positive behavior of the resist. Interestingly, by exposure of a 10x higher electron dose, chain crosslinking becomes dominant and PMMA switches its response to negative tone. Here, instead of chain fragmentation during exposure with lower doses, the chains will crosslink, making them insoluble to removal agents[168,178–180]. In the presented work, PMMA in negative tone was utilized for nanopatterning of the capacitive sensing structure in EIC.

In this work, PMMA 950k was used as a negative resist by drastically increasing the exposure dose by 10- to 100-fold magnitude. The substrate was chosen to be a common transparent glass slide for later observation during measurements by light microscopy. Firstly, the glass substrate was cut into half with a diamond pen. Before the substrate was covered with 5 nm Cr and 50 nm Au (process described in *Chapter 3.3*), it had to be cleaned very thoroughly for archiving a homogeneous and contaminant-free covering of the surface. The cleaning protocol involved supersonic agitation in acetone and isopropanol for 5 minutes to remove bigger dust particles and contaminants on the surface. Next, smaller organic and metallic contaminants were removed by substrate immersion into RCA-1 and RCA-2 cleaning solutions for 15 minutes at 80°C each and gently blown dry by a nitrogen stream. Next, the substrate was dry cleaned in atmospheric oxygen plasma (Zepto System, Diener electronic GmbH, Germany) for 5 minutes at 100 W and 0.3 mbar. Now, the substrate was carefully fixed on the evaporation holder by carbon pads and put into the evaporation device for thermal metal deposition. After deposition, the substrates were removed from the chamber and cleaned in acetone, isopropanol and in oxygen plasma with the same parameters. After plasma treatment, a 70 nm thick layer of PMMA 950k was spincoated using a spinning speed of 4000 rpm/s for 50 seconds (RC8, SÜSS MicroTec SE, Germany). After baking at 130°C for 5 minutes the substrate was transferred to the SEM with an integrated EBL module (ELPHY32, Raith GmbH, Germany). By applying high beam doses (in the mC/cm^2 regime) with an acceleration voltage of 30keV and a beam current between 100 - 200 pA, the exposed parts of PMMA were highly crosslinked. After exposure, unexposed PMMA was removed by immersion in acetone for 3 minutes. Now, unprotected gold and chromium layer were dry etched using dry radical ion etching (RIE) in argon atmosphere for 5 minutes (IonSys500, Mayer Burger AG, Germany). Finally, the PMMA protection layer was removed by oxygen plasma treatment for 5 minutes at 100 W at 0.2 mbar.

3.2.2 Laser lithography

Laser lithography represents a powerful tool to structure a surface in a maskless fashion. In the used device (DWL 66FS, Heidelberg Instruments Mikrotechnik GmbH, Germany), a diode laser with a wavelength of 405nm is guided in a scanning mode over the substrate thereby writing a structure on a laser-sensitive surface[181]. This structure was designed *in silico* using a vector-based program, *i.e. WieWeb's CleWin*[182]. This method was used to fabricate mask for following UV lithography approaches. Here, up to 9 different structures for microfluidic master structures or electrode designs could fit in an area of a 5inch wafer and written overnight directly on a mask. This commercial available mask consisted of a glass-lime substrate coated with a chromium layer. On top of the chromium, a layer of laser-sensitive resist was coated (AZ1518). After writing, the mask was developed in a mixture of AZ351(B) developer and deionized water in a ratio of 1:4 for 3 minutes. Following, the developed structure was checked under the

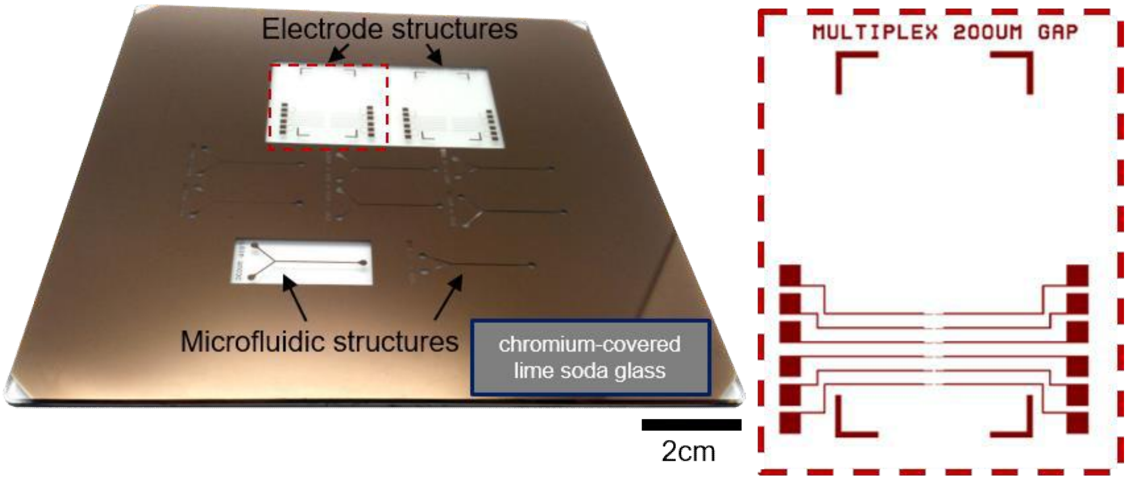

Figure 6: Ready-to-use mask defined by laser lithography. It contains two structures for electrodes (top part) and several geometries for microfluidic purposes (bottom part). On the right side, the corresponding designed pattern of an electrode design can be seen.

microscope for proper development. If needed, the mask was immersed into the development solution for additional 10 seconds and checked again. This step was repeated until the structure was developed correctly. Following, the mask was immersed in Cr-etchant for 1 minute. After rinsing with water and drying with nitrogen, residual resist was removed in acetone for 1 minute in supersonic agitation. On Figure 6, a typical ready-to-use chromium mask can be seen. On the mask, two electrode designs were patterned while several microfluidic patterns can be seen at the bottom part. On the right side, the corresponding pattern *in silico* is depicted.

3.2.3 UV lithography

Like in EBL, optical lithography is a method to pattern resist-coated planar samples. Here, the main differences are the use of photons to locally alter the light-sensitive resist. During exposure, the sample is placed below a patterned mask (defined by laser lithography, as described in the previous chapter), which partially covers the sample. The light source usually a mercury arc lamp since its shows strong emission in near- mid- and deep-UV[183]. Here, light passes through the mask, thereby only reaching the exposed areas of the resist below. Depending on the tone of the resist, it is altered towards sensitivity or resistivity to its developer (see Figure 7). As a prominent example for UV-sensitive negative resist, the polymer SU-8 will be introduced. SU-8 is an epoxy-based resist which, upon UV-catalyzed acid formation in the resist between 350-400 nm, highly crosslinks at elevated temperatures. In this, UV-light is not absorbed by SU-8 itself, but only by the dissolved photoinitiator (up to 10 wt%) resulting in acid generation upon photon absorption. Consequently, released H^+ ions locally open the ring structure of SU-8, allowing high crosslinking of its monomers under emergence of additional H^+ ions thereby continuing the chemical reaction. Since one photon causes hundreds of reactions, SU-8 is classified as a *chemical amplified resist*[184–186]. Thus, its grants high aspect ratios of the developed pattern with up to 200 µm film thicknesses[187], since UV-light is only absorbed by a small fraction (the photoinitiator) in the resist mixture. Due to its high thermal and physical robustness[188,189], vertical side walls even with high aspect ratio[190] and low dielectric constant[191], SU-8 represents an excellent resist for patterning surfaces for microfluidic channels[188] and in MEMS technology[191]. Next to direct microfluidic channel fabrication in SU-8, channel structures can be fabricated using a template structure negatively replicated with a thermo-responsive polymer (see Figure 7, left path), *e.g.* PDMS. The details of this technique, called *soft lithography*, will be discussed in the following paragraph. Next to fabrication of microfluidic patterning of surfaces using optical lithography, another focus in this technique is set on the fabrication of microelectronic patterns. Here, structured UV-sensitive polymers are used either as a protective mask for underlying layers during etch processes or as sacrificial layer during lift-off processes. In this, the patterned surface is evaporated with *e.g.* metals, followed by removal of metal-covered resist. Thus, only the areas where the metal was evaporated will remain on the surface (see Figure 7, right path). The resistive characteristics of SU-8 disqualifies it to be the resist of choice of these protocols, *i.e.* as protective and sacrificial layer, since it cannot be gently and easily removed from the protected layer or from the substrate. Further, for lift-off processes, vertical side walls are not preferred since it can easily cause defects during resist removal since the metallic layer is continuously covering the substrate leading to limited penetration of removal solvent into the resist. Here, resists showing undercut structures at their edges are preferred since they circumvent continuous metal coating, making lift-off more reliable[192]. In the presented work, the resist

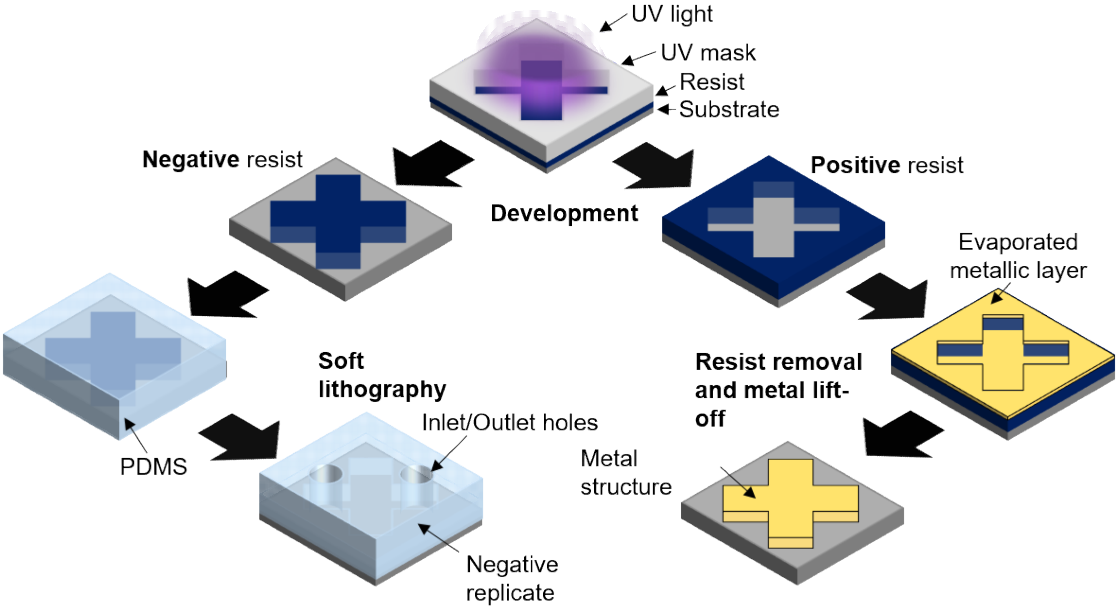

Figure 7: Optical lithography protocols for fabrication of PDMS-based microfluidic channels (left track) and metallic electrode deposition (right track). **Left track:** Usage of negative tone SU-8 as master structure and PDMS as channel material. Here, PDMS forms a negative replicate of the channel structure which can be sealed on *e.g.* glass or silicon substrates. **Right track:** Fabrication of a sacrificial layer via the resist AZ5214E, followed by thermal metal deposition. After resist removal, only metal areas remain which were directly evaporated on the substrate.

AZ5214E was utilized for metal lift-off processes, since it showed adequate undercut edge at reasonable height, while SU-8 was used as template structure for microfluidic channels. AZ5214E resembles a mixture of novolak resin and naphthoquinone diazide making it usable in both positive and negative tone[193]. Next, the experimental procedure for micropatterning of these two resists is described.

3.2.3.1 Microelectrode patterning

For microelectrode patterning, substrates were coated with the image-reversal resist AZ5214e at 3400 rpm for 1 minute resulting in an approximately 1.5 µm thick film. After baking for 1 minute at 110°C the resist was illuminated through the respective mask for 1 second (MJB4, SÜSS MicroTec SE, Germany). Subsequently, the substrate was heated at 120°C for 2 minutes. Following flood exposure for 30 seconds and development in pure AZ726MIF solution for 30 seconds patterned the resist in a negative fashion.

3.2.3.2 Microfluidic patterning

Table 5: Baking protocols for SU-8 based UV lithography on silicon substrates

Pre Baking Temperature	Time	Post Bake Temperature	Time
65°C	1 min	65°C	2 min
Up to 95°C	3 min	Up to 95°C	3 min
95°C	3 min	95°C	6 min

In order to fabricate master structures for soft-lithography procedures, a common silicon wafer was cut into proper geometries using a diamond and cleaned afterwards thoroughly with acetone and isopropanol. Firstly, the substrate was coated with the adhesion promotor TI-Prime at 4000 rpm for 60 seconds and baked at 110°C for 1 minute. Following, a 15 µm thick layer of SU-8 was spincoated on the silicon substrate, prebaked at 95°C for 3 minutes and exposed to UV light for 7.5 seconds. After subsequent baking at 95°C for six minutes, the resist was developed in pure mrDev600 solution for three minutes. Finally, the structure was postbaked at 150°C for 1 hour. On table 5, a detailed description of the baking times can be seen.

3.2.4 Soft lithography

Soft lithography represents a lithographic technique for manufacturing nano- and microstructure by replica molding at low costs. Here, the central point depicts the fabrication of a patterned elastic stamp, formed from a negative master structure, *e.g.* UV-lithographically patterned SU-8 on a planar substrate. During fabrication, the stamp's material is poured over the master structure and crosslinked, forming a negative replicate of the structure. The most prominent elastomeric stamp material is Poly(dimethylsiloxane) (PDMS) since it is fluid at room temperature, can be easily crosslinked and is able to replicate features down to 30 nm[194]. Next to a broad range of applications for utilization of these stamps for *e.g.* pattern transfers, microcontact printing and replica molding[195], they can be directly used as microfluidic channel structures. Its simple processing protocols as well as chemical and mechanical properties makes this polymer suitable for microfluidic applications with respect to fabrication of MEMS and biomedical applications[196,197]. It is biocompatible, non-fluorescent, transparent, permeable to gases as well as chemically inert and thermally stable[198]. A big advantage to use PDMS in microfluidics is its ability to conform to surfaces thereby tightly sealing the channels. Further, its hydrophobic nature by exposed methyl groups on its surface can be altered to ultra-hydrophilic behavior by treatment in oxygen plasma. This plasma-induced formation of –OH groups on the PDMS surface can be additionally utilized for permanent sealing of a channel system on silicon-based surfaces by covalent bonds formed during condensation reaction when both treated surfaces come into contact[199,200] under the emergence of water. On the following figure, a schematic illustration of the covalent bonding mechanism of plasma-activated PDMS on a common SiO_x glass surface can be seen.

In this work, the master structure, fabricated by UV-lithography, is replicated using the polymer PDMS. By pouring PDMS over the master structure with a following curing step at elevated temperatures, a negative replicate was created. For the fabrication of the microfluidic channel geometry, PDMS was mixed with its curing agent in a 6:1 ratio, granting high stability and less probability for channel collapse during alignment procedures, and mixed well using a plastic stirrer. Subsequently, the mixture was vented in the vacuum oven for 10 minutes to remove air bubbles occurred during mixing. Now, degassed PDMS mixture was poured over the master structure. To prevent leakage of the liquid PDMS, a self-made metal frame was put around the replicated structure. After pouring, it was cured overnight at 70°C on a hotplate. After hardening, cured PDMS was removed from the silicon wafer and cut into proper geometry using a scalpel and channel in- and outlets are punched through the cell using a biopsy needle. Finally, the microfluidic channels were cleaned by a rinsing step in isopropanol and gently dried using a nitrogen stream. Following, both PDMS and substrate were activated in oxygen plasma for 5 seconds at 40 W and 1 mbar. Next, the two surfaces were carefully pressed together, triggering the condensation reaction of activated Si-OH on the PDMS and substrate surface, forming a covalently Si-O-Si bond.

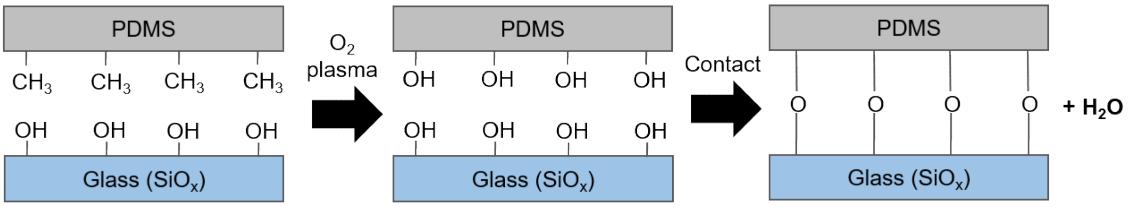

Figure 8: Plasma-activated covalent bonding of PDMS to glass. Here, oxygen plasma generates -OH groups on the surface of PDMS. If the two surfaces are brought into close contact, a spontaneous condensation reaction takes place, thereby forming a covalent oxygen bond between the silicon atoms of both substrates under the emergence of water.

3.3 Thermal deposition of metals

Substrates were cut into the proper geometry using a diamond pen. Following, they were cleaned thoroughly using the cleaning protocols with acetone, isopropanol, RCA1 and RCA2. Prior to thermal evaporation, substrates were additionally cleaned in oxygen plasma for 5 minutes. After preparation, they were fixed on a metal holder and transferred to the evaporation device. At high-vacuum conditions (5-7x10^{-7} mbar) a thin Cr adhesion layer was evaporated (5 nm) at a deposition rate of 0.1 Å/s followed by an Au layer (50 nm) with a rate of 0.5 Å/s (Univec 300, Leybold Dresden GmbH, Germany). After the evaporation process, the substrates were additionally heated at 200°C on a hotplate for 2 hours to additionally clean the surface and remove organic residues and microcracks in the gold layer.

Additionally, after metal deposition including a sacrificial resist layer, the substrate was carefully removed from the metal holder and immersed in acetone. By gently shaking on a tilting table for 30 minutes, the resist was stripped off. Following, the substrate was cleaned in isopropanol and gently dried using nitrogen. Lastly, the newly deposited metal layer was annealed for 2h at 200°C in low vacuum conditions.

3.4 APTES functionalization

Oxide surface were functionalized to enable new properties for later experiments. In this, they were either activated in oxygen plasma (100W for 30 seconds) or incubation in 1 M NaOH for 1 hour. After cleaning and surface activation, the surfaces were incubated in liquid solution, containing the active molecule. In this work, APTES was used to grant the surface higher hydrophobicity and lower surface energy. APTES solution was mixed with deionized water and ethanol in a ratio of EtOH: H_2O: APTES = 100: 5: 2 and left at room temperature for 10 minutes. Following, the activated substrate was immersed into the silanization mixture for 1 hour under gentle shaking. Next, the substrate was washed three times with pure EtOH and left for 15 minutes at 130°C on the hotplate. For APTES functionalization of microfluidic channel, the PDMS-substrate chip was carefully flushed with APTES solution after bonding at saturated environment.

3.4.1 Fluorescent labeling of APTES

In order to label APTES, the silanized surface was incubated for 1 hour in 10mg/mL succinic anhydride firstly dissolved in dimethyl sulfoxide (DMSO) and diluted 1:10 in 200 mM boric buffer. This incubation resulted in an opening of the ring structure. Following, the substrate was carefully rinsed in borate buffer and activation was carried out by incubation for 10 minutes in 10mM 1-Ethyl-3-(3-dimethylaminopropyl)carbodiimide (EDC) and 5mM N-Hydroxysuccinimide (NHS) both dissolved in 1x PBS buffer. Subsequently, the surface was incubated for 1 hour in 1x PBS with 20 µM of FITC-labeled DNA. Finally, the functionalized surface was washed again with fresh PBS and observed under the fluorescence microscope.

3.5 Measurement devices

In this work, two main approaches for microfluidic integration of nanostructures for sensing are presented. Namely, the conjunction of droplet-based microfluidics and silicon nanowire field effect transistors and the dynamic impedimetric detection of microanalytes using gold nanowires. In the following, the measurement setup for these two fabricated device are presented.

3.5.1 SiNW FET measurements

SiNW FETs were contacted by connection of the respective contact pads (gate (G), source (S) and drain (D)) using micromanipulators equipped with tungsten needles, connected to a sourcemeter (see Figure 9, panel A, middle). Here, the chip was placed under a stereomicroscope for simple contact pad connection via the manipulators and for observation of droplet formation and propagation. A sourcemeter (2604B, Keithley Corp., USA) was utilized to generate and measure currents and potentials passing through the micromanipulators and the connected FET (see Figure 9, top, right). It was controlled by a MatLab code for acquiring time-dependent I_{SD} measurements at constant V_{GS} as well as transfer characteristics at constant V_{SD}. For FET characterization measurements, V_{GS}

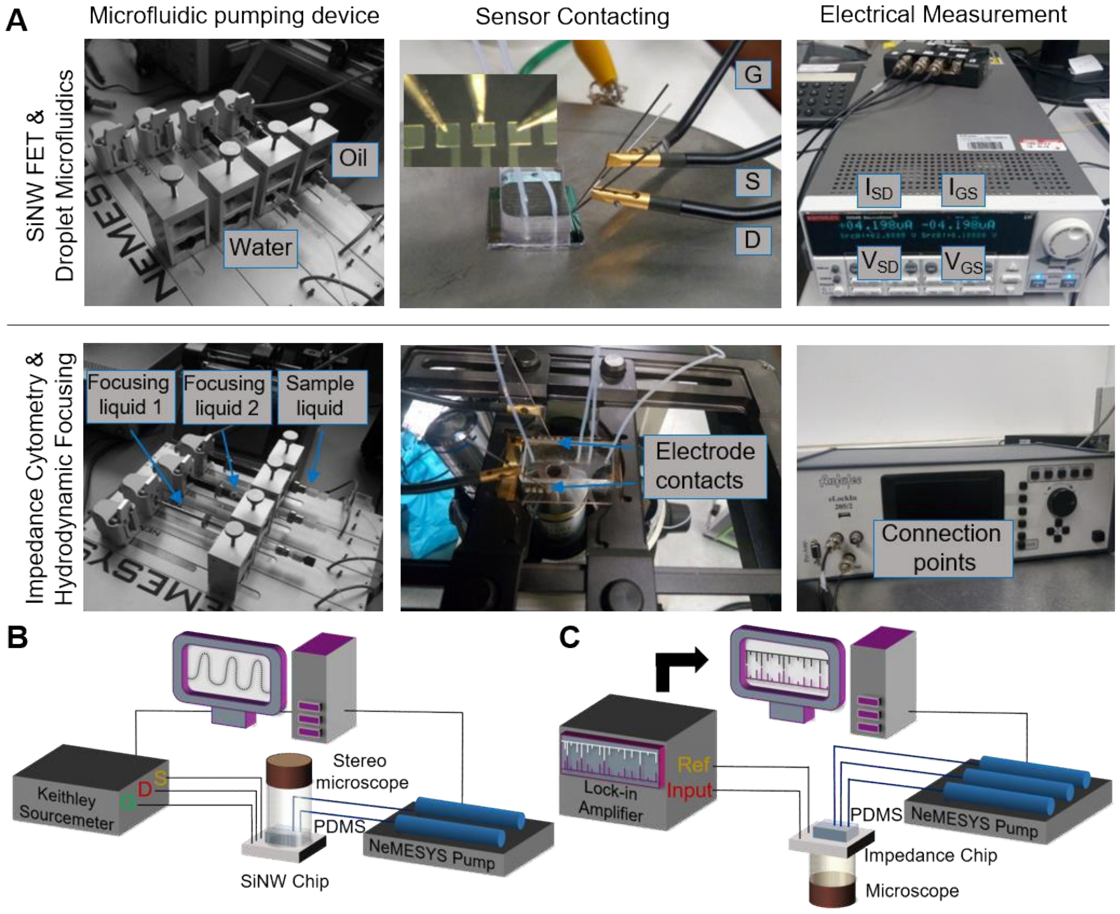

Figure 9: Measurement setup for SiNW droplet detection and EIC detection of micron-sized objects. In both setups, liquids are actively manipulated using a micropump device and the connection was carried out using micromanipulators. **(A)** Electric signal generation and response capture was carried out using a sourcemeter, connected to a computer and controlled by a MatLab code for SiNW FET measurements (top). For impedance output data collection, a lock-in amplifier was used for direct readout and data capture (top). Following, the data was transferred to the computer for analysis. **(B)** Schematic illustration of electrical and microfluidic connections to SiNW sensors and for **(C)** impedance sensors.

was swept from -2 V to +2 V in both directions, while droplets were detected at constant V_{GS} = 1 V and V_{DS} = 0.25 V in the time domain. Liquids (disperse aqueous phase and continuous immiscible phase) were actively pumped using a syringe pumping device (neMESYS 290N, Cetoni GmbH, Germany) which is able manipulate 4 syringes independently using a computer (see Figure 9, top, left). Syringes were connected via teflon tubes to the PDMS channel system, attached to the FET chip (see Figure 9, panel B).

3.5.2 Electrical Impedance cytometry measurements

EIC structures were contacted using micromanipulators connected to a lock-in amplifier (eLockIn205/2, Anfatec Instruments AG, Germany) able to generate an AC signal of arbitrary input amplitude and frequency (see Figure 9, Panel A, right panel). As for FET chip contacting, micromanipulators were utilized for connection to the electrode pads. Here, the chip was additionally placed under an optical microscope for contacting the electrode pads and for observation of the microfluidic focusing system (see Figure 9, panel A, middle). For characterization of the device in EIS mode, the AC frequency was swept between 50 Hz and 20 MHz at fixed amplitude input signal (V_{in} = 0.5 V). Here, the deviations of the impedance amplitude and phase shift were recorded in two parameters as the variables V_{out} and *Phase*. Further, data collection of time-dependent signal deviations in both amplitude and phase shift was applied in dynamic measurements at constant V_{in} = 0.5 V and fixed frequencies of 100 kHz and 500 kHz. As in the previous device, liquid manipulation was actively carried out using a pumping system (see Figure 9, top, left) using 3 independently controlled syringes for the focusing streams and analyte stream. After the experiment, data was transferred via an USB stick from the lock-in amplifier to the computer for analysis (see Figure 9, panel C).

3.6 Bacteria and cell cultivation

3.6.1 PBMC purification and treatment

PBMCs from healthy donors (25-32 years old, female and male) and one patient diagnosed with acute myeloid leukemia (74, female) were obtained from Ethylenediaminetetraacetic acid (EDTA)-venous blood samples. Written informed consent was provided by the patient. Cell separation and experiments were performed immediately after blood drawing. PBMCs were purified from whole blood using Ficoll-Paque PLUS density gradient centrifugation. After isolation, PBMCs were cultured in RPMI 1640 medium containing 1% antibiotic-antimycotic mixture and 10% heat-inactivated fetal bovine serum. Different staining for flow cytometry analysis were performed to detect the main PBMCs subpopulation on human ex vivo immune cells. Fluorescein isothiocyanate (FITC)- anti-CD3+ (SK7 clone) for T cells, phycoerythrin cyanine7 (PE Cy7)- anti-CD20 (L27 clone) for B cells, allophycocyanin (APC)- anti-CD56 (B159 clone) for NK cells and phycoerythrin (PE) conjugated anti-CD14 (Mϕ9 clone) for monocytes.

3.6.2 Bacteria cultivation

Prior to cultivation, culture media and equipment was autoclaved at 121°C. The bacteria strains *Bacillus subtilis, Escherichia coli, Lysinibacillus sphaericus* and *Sporosarcina ureae* were propagated on individual agar plates (15 g/L agar, 8 g/L NB-medium Bacto Nutrient Broth) over night at 30°C. On the next day, three to five formed colonies were transferred to 15ml liquid media (5 g/L Bacto^{TM} Peptone) over night at 30°C under aerobic conditions and gently shaking. The next day, the grown bacteria were centrifuged for 5 minutes at $3000\,\mathrm{rpm/s}$ and the nutrition media was exchanged with 0.1x PBS solutions. After re-suspension by short vortex intervals and manual shaking, the bacteria solution was ready to use and could be transferred to the microfluidic system.

4. Compact nanosensors probe microdroplets

4.1 Overview

In the first part of the results, the fabrication, characterization and utilization as a biosensor for a novel platform, comprising droplet microfluidics and SiNW FET technology, is presented. Microfluidic droplets were created directly on chip using a conventional PDMS-based microfluidic channel system (see Figure 10). For the first time, electronic and optics-less detection of propagating aqueous droplets using SiNW FETs was demonstrated. After proof-of-concept experiments including detection of deionized water droplets with various volumes at different speeds, the droplet's content was changed to a physiological relevant environment. Here, the aqueous phase was altered to PBS buffer solution at different pH values and ionic concentrations. In this, sensitivity towards physiological pH values (pH 4-8) and various molar concentrations of PBS buffer could be demonstrated. Finally, the novel sensing platform was utilized to track the kinetics of a chemical reaction, taking place in propagating droplets.

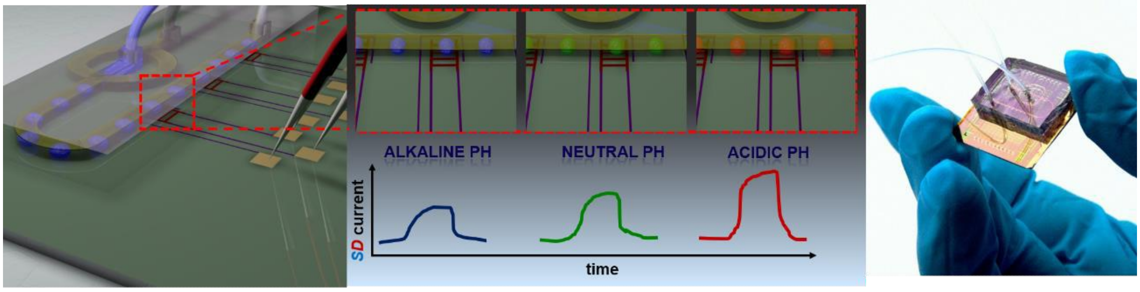

Figure 10: Schematic illustration of the sensor device. The PDMS-based microfluidic system was covalently bound on the chip substrate, allowing formation and guidance of nanoliter droplets directly on the chip. After formation, the droplets were guided to the main channel, aligned over the SiNW FET devices for label-free and optics-less sensing. Here, the signal of the droplets was dependent on the pH value. Low pH values (acidic) of the droplets resulted in higher I_{SD} current changes, when the droplet was passing the SiNW FET and *vice versa* for high (alkaline) pH values.

4.2 Fabrication

4.2.1 SiNW FET fabrication

The fabrication and characterization of the sensing device, namely the SiNW FET chip, was carried out and described in detail in the work of Pregl et. al[201] in cooperation with the NamLab gGmbH Dresden[202]. Briefly, the silicon nanowires were grown using gold nanoparticles (19 nm in diameter) as seeds on a silicon substrate by chemical vapor deposition. Following, they were transferred by contact printing technique on the silicon chip substrate resulting in parallel aligned arrays of nanowires. Next, the contact electrodes, consisting of nickel, were deposited on the substrate by lift-off strategy. Here, the geometry consisted of interdigitating finger electrodes which contacted the silicon nanowires to the source and drain. Next, an atom-sharp $NiSi_2$-Si Schottky junction was formed by a silicidation process within in the intrinsic nanowires. These Schottky barrier-FETs showed a preferred p-type polarity, demonstrating a Schottky-barrier height of 0.66 eV for electrons and 0.45eV for holes. Finally, the device was passivated by a 20 nm thick Al_2O_3 layer (see Figure 11, panel A and B).

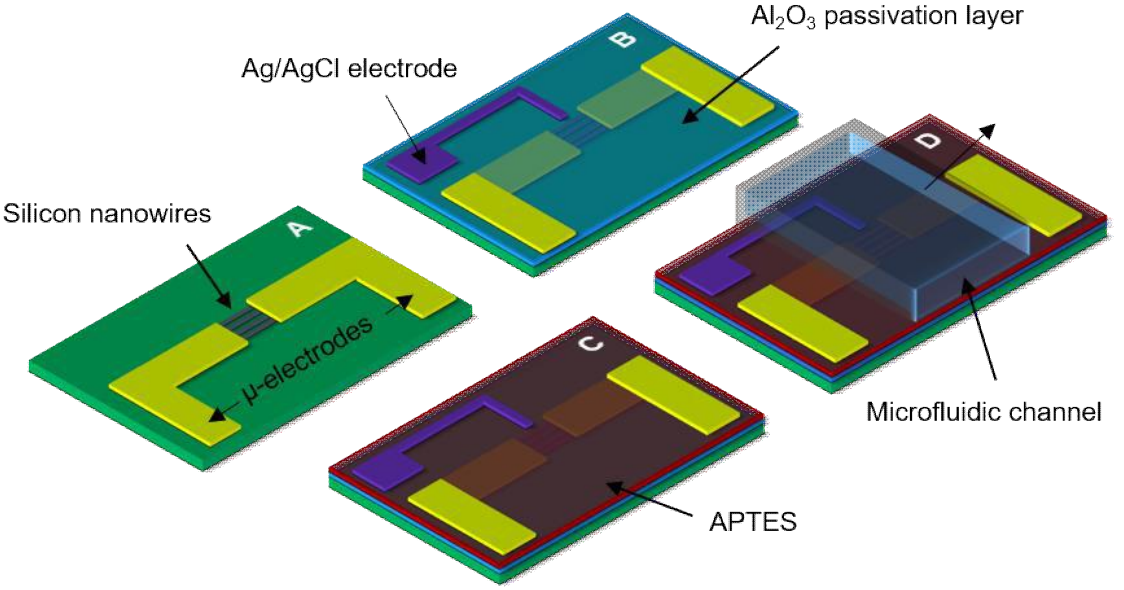

Figure 11: General Fabrication of the SiNW FET: **(A)** Silicon nanowires were transferred on the substrate and contacted by nickel electrodes. **(B)** CVD deposition of the Al_2O_3 oxide layer with a thickness of 20 nm and equipment with an Ag/AgCl top-gate electrode. **(C)** APTES silanization for improved pH sensitivity. **(D)** Microfluidic integration of the chip.

4.2.2 SiNW FET modification for top-gate sensing

In order to measure a stream of discontinuous liquids, guided over the FET, the gate electrode was directly deposited near the source-drain electrodes on the passivation layer, consisting of a 5 nm Cr adhesive layer and 50 nm Ag layer, deposited by thermal evaporation. Following, the deposited silver on the surface was transformed into silver chloride (AgCl) by applying an electrochemical reaction. Here, the silver electrode was covered with a drop of 0.1 M KCl solution and connected to the sourcemeter while the droplet was connected by a platinum wire. Applying a constant current of 1 μA for 1 minute, the chloride of the solution diffused into the silver, forming a layer of AgCl at the electrode surface (see Figure 11, panel B). Further, the chip was functionalized with APTES since it additionally improves the sensitivity towards alterations in the pH value of the environment by (de-)protonation of its amino-group[203] when functionalized on the SiNW FET chip (see Figure 11, panel C). Thus, pH values changes in the environment also modulate the charge density based on the amino-group of APTES thereby influencing the conduction channel formation of the FET. Finally, the chip was equipped with a microfluidic channel for direct formation and detection of microfluidic droplets on chip (see Figure 11, panel D).

4.3 Electrical characterization

Prior to droplet sensing, the response of silicon nanowire field effect transistors was tested in dependence of different liquid environments, which were used as continuous and dispersed phase in droplet configuration, namely mineral oil and deionized water. In addition, the effect of the additional Ag/AgCl top-gate electrode was evaluated being in contact with the liquid phases. On the following figure, the transfer characteristics of both back-gated (right) and top-gated SiNW FETs, covered by a drop of conductive (deionized water) and non-conductive (mineral oil) media, can be seen. For top-gated FETs, a clear difference in the transfer characteristics for gate voltages (V_{GS}) between +2 V and -2 V could be observed. Here, the source-drain current of the conductive medium (green, deionized water) showed a clear difference from non-conductive medium (black, mineral oil). This effect is attributed to the impact of the medium conductance which influences the efficiency of surface charge accumulation of

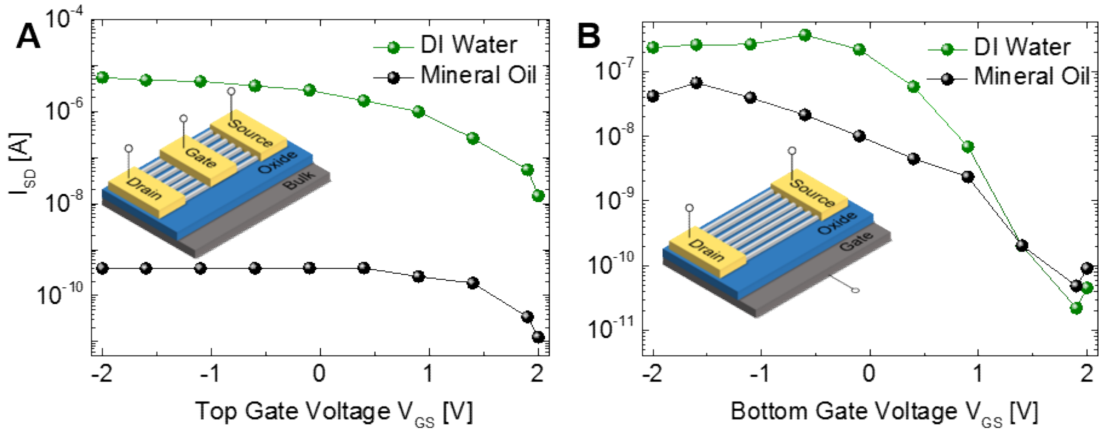

Figure 12: Transfer characteristics of top-gated and back-gated SINW FETs covered with a drop of conductive (water) and non-conductive (mineral oil) medium: **(A)** Source-drain current in dependence of the top-gate voltage. A clear difference for conductive (water) and non-conductive (mineral oil) media could be observed. **(B)** Source-drain voltage in dependence of the bottom gate voltage. The impact of the surrounding medium is less pronounced; the FET demonstrated p-type behavior.

the electrical double layer and modulates therefore the conductivity of the FET. In the top-gate configuration, the ionic phase influences the effect of channel opening as soon as a gate voltage was applied. In this, the SiNW FET stood in on-state for deionized water and in off-state for mineral oil over the complete range, given by the different conductivities of the liquids. In contrast, if the FET was controlled via back-gate, the covering liquid was barely influencing the transfer characteristics of the FET, since the electron channel opening was controlled from the bulk, representing a MOSFET configuration (see Figure 12, panel B). In this, the SiNW FET showed excellent p-type switching behavior in *off- and on* state over four magnitudes. For following experiments, top-gate modulated FETs were used due to their higher sensitivity of surrounding media by direct contact of the gate electrode to the medium.

4.4 Flow-focusing droplet generation

4.4.1 Flow-focusing geometry

For droplet generation, a flow-focusing structure was employed which geometry enables cutting of the droplet phase by arising capillary instabilities of the stream caused by the continuous liquid flow. After the flow-focusing geometry, a rhombus structure was placed to see a clear droplet formation for later characterization. Following, long microfluidic serpentine structures for a better observation and characterization of moving droplets were introduced, ending in an outlet structure (see Figure 13, panel A and B). Microfluidic structures were fabricated in PDMS by standard soft-lithography approach with a channel width of 300 µm and channel height of 15 µm using the UV-photoresist SU-8 (see Figure 13, panel C), as described in *Chapter 3.2.3 and 3.2.4*. Finally, the chosen substrate for simple observation and characterization was a common borosilicate-based microscope slide. Here, both PDMS channel system and glass were covalently bound using oxygen plasma treatment (see Figure 10, panel D). Further, in order to guarantee stable droplet formation and propagation through the system, all channel walls had to be homogeneously rendered hydrophobic to minimize interaction between the aqueous droplets and the channels. For this, the channels were directly flushed after sealing with a solution containing 2% APTES in ethanol (described in detail in *Chapter 3.4*). Doing so, the channel walls (comprised of glass and PDMS) were functionalized with the aminosilane since they remained activated by the plasma treatment. Here, the surface was homogeneously rendered

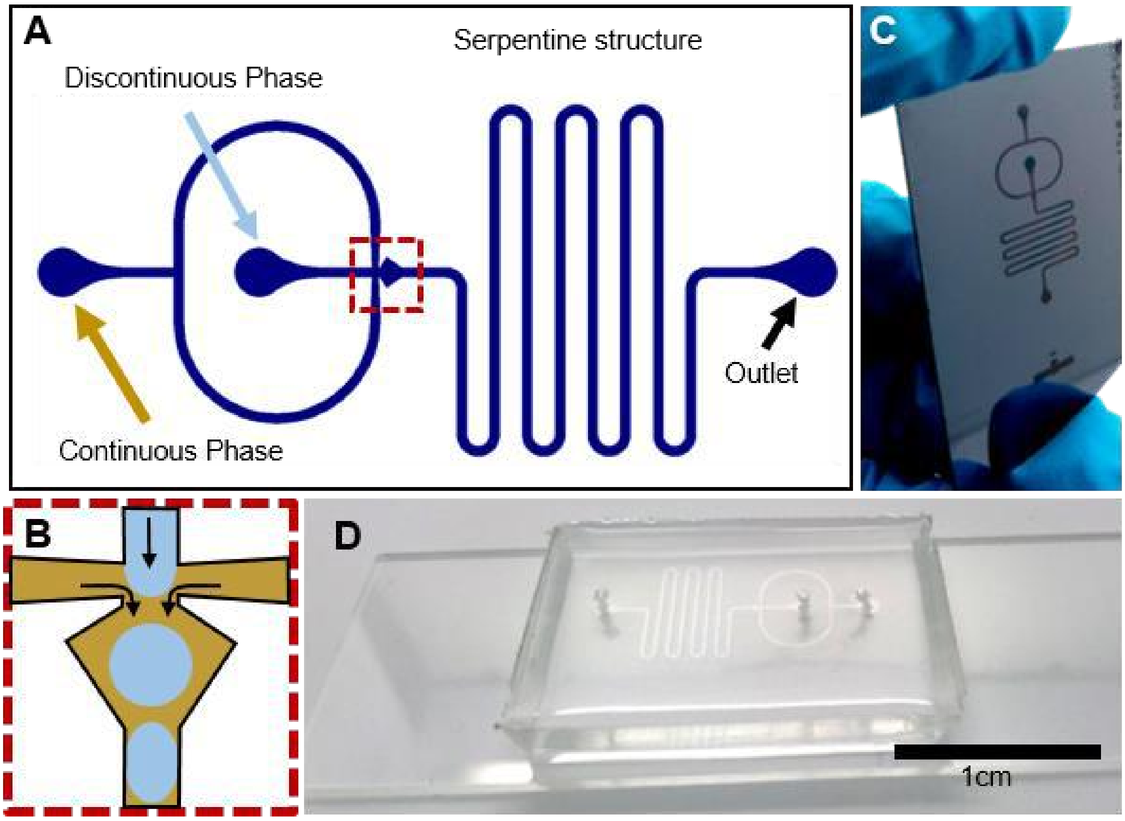

Figure 13: Droplet microfluidic design **(A)** Microfluidic channel system designed by WieWeb's CleWin with a channel width of 300 µm. Injection of continuous phase (yellow arrow) and discontinuous phase (blue arrow) by larger round geometries. **(B)** Close-up of the flow-focusing structure. The discontinuous stream (blue) is cut into homogeneous droplets by the discontinuous stream (yellow) coming from left and right. **(C)** SU-8 based master structure on a common silicon wafer with a height of 15 µm. **(D)** PDMS channel system fabricated by soft lithography. The negative replicate was covalently sealed to the glass substrate by oxygen plasma treatment.

Hydrophobic by exposed amino-groups on the channel walls, which could later be observed by low interactions of aqueous phase and the channel walls. Prior to its integration on the SiNW FET chip, the behavior of the designed microfluidic structure was evaluated with respect to the general capability to generate droplets at various speeds and volumes. Here, special attention was drawn onto its capability to generate aqueous droplets at reasonable volumes and corresponding lengths (compared to the FET structure length) as well as homogeneity of the individual droplets, without unwanted droplet splitting or trapping within the channels. For this, the functionalized ready-to-use flow cell (see Figure 11, panel D) was placed under a conventional inverted microscope and its inlets were connected to syringes with the respective liquids via teflon tubes. The following figure depicts a close-up of the flow-focusing region of the microfluidic geometry (top) as well as one propagating droplet in the serpentine structure (bottom). In this, the water phase (Figure 14, panel A, blue arrow) was actively pushed towards the crossing structure, where mineral oil is pushed from the bottom and top channel (yellow arrows). Additionally, the mineral oil phase was probed with a surfactant agent, namely Span-80® at a concentration of 2%. The stabilization of the liquid surfaces allowed homogeneous and stable droplet formation as well as controlled droplet propagation within the channels without breakage or fusion of single droplets even if they came in close contact. In the presented example, both flow rates were set to 1 µl/min. By occurring capillary instability of the water phase as it is pushed through the crossing structure by the oil phase, the aqueous phase is cut into homogeneous isolated droplets one after another (as described in *Chapter 2.4.2*). Utilizing this geometry and flow rates, emerging droplets were formed within approximately 1.5 seconds, moving at a speed of 15 µm/ms through the serpentine structure. Here, the droplet formation rate was approximately at 1 Hz and could be increased up to 10 Hz (see *Chapter 4.5*) by increase of the absolute values of both flowrates. Further, the water droplet propagation can be seen on Figure 14, panel B. Due to usage of a surfactant agent and hydrophobization of the channel walls, droplets showed a semi- circular and well-defined flow profile as they move in the channel.

A Water Droplet Formation

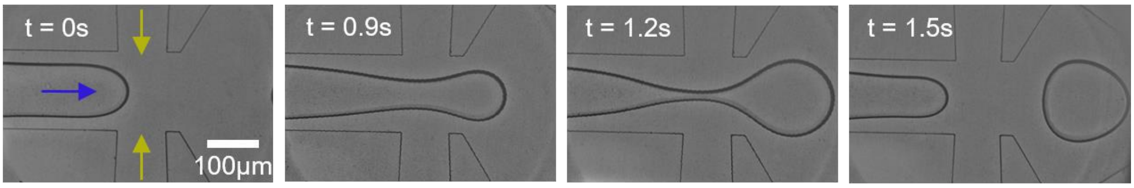

B Water Droplet Propagation

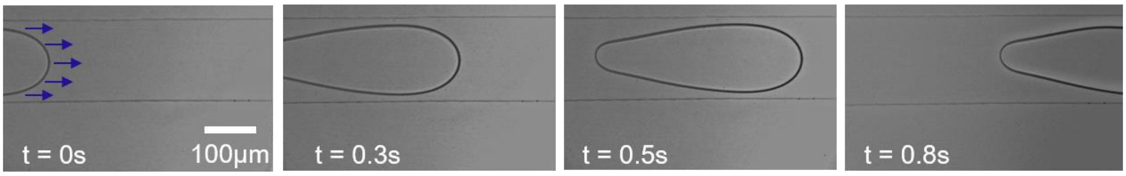

Figure 14: Microfluidic droplet formation and propagation: **(A)** Droplet formation of the deionized water phase (blue arrow) were cut into homogeneous and isolated droplets by the oil phase (yellow arrows). **(B)** Droplet propagation in the channel. Channel surface hydrophobization led to formation of a defined semi-circular flow profile of the droplet.

4.4.2 Flow-focusing droplet characterization

In order to evaluate if the aqueous droplets, generated by the microfluidic structure, were feasible for being detected by the SiNW FET, the range of droplet volumes which could be generated was analyzed. Here, the FET sensing area was located at 380 µm length x 425 µm width. For this, the microfluidic cell was filled with deionized water and mineral oil as described in the previous chapter. Since volumes of emerging droplets are only dependent on the flow ratio between water and oil streams (Q_{water}/Q_{oil}) at fixed channel geometries, only the ratio was altered in order to manipulate the droplet volumes. After generation, droplets were recorded as they propagate through the channel system and analyzed with image processing software “Fiji Is Just ImageJ” (Fiji)[204]. For each applied flow ratio, the volumes of 20 droplets were measured, taking into account a constant height of the droplets of 15 µm in the channels. The length of the droplet was measured from the very edges of the droplets, *i.e.* from the front apex till the tail of the moving droplet. In the following figure, both volume and length dependence on the applied flow ratio of water and oil streams Q_{water}/Q_{oil} can be seen for flow-focusing structure with a channel width of 300µm. As expected, both volume and

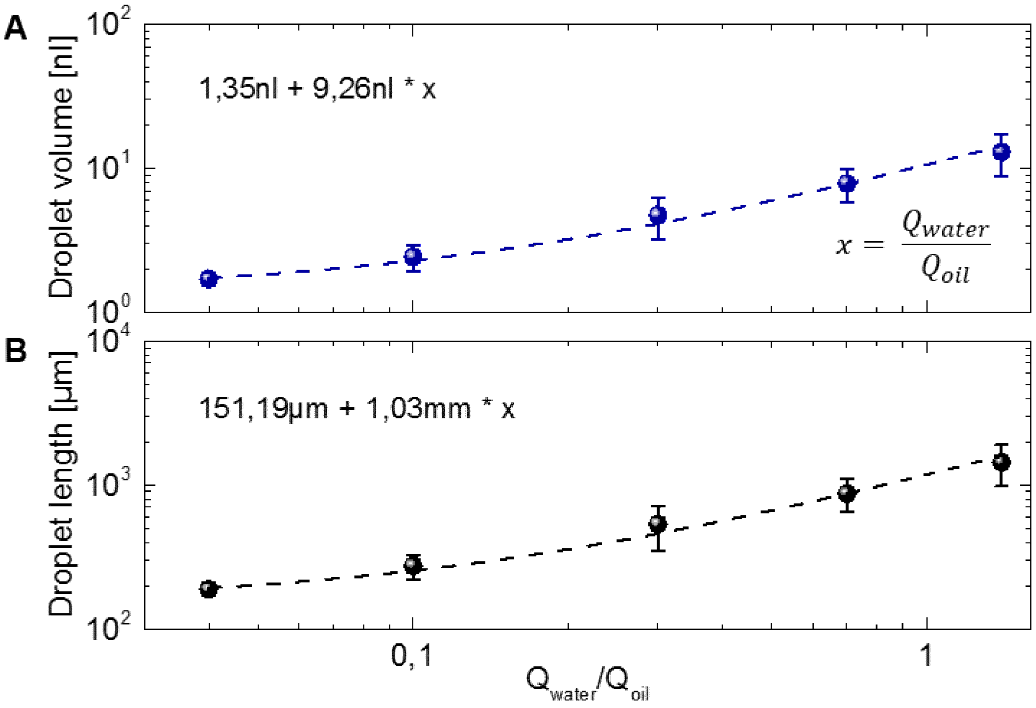

Figure 15: Dependence of droplet volume and length on the flow ratio of continuous and dispersed phase. Each data point represents the mean value of 20 measured droplet volumes and lengths. **(A)** Reproducible droplet volumes ranged between 1.7 nl for the smallest ratio (0.04) to 12.9 nl for the highest ratio (1.2). **(B)** Corresponding droplet lengths of the propagating droplets, ranging from 189.4 µm to 1443.4 µm for the smallest and highest applied ratios, respectively.

length of the droplets increased if the ratio was increasing, at low deviations within the same applied ratio over the full range (depicted as the standard deviation). Here, the smallest droplet volume which could be observed and generated at reasonable reproducibility, was found at 1.7nl for $Q_{water}/Q_{oil} = 0.04$, while the highest reasonable volume was located at 12.9nl for $Q_{water}/Q_{oil} = 1.2$ (see Figure 15, panel A). In this, the lengths of droplets were directly proportional to the droplet volume, since they moved in a channel with fixed values for height and width. They ranged from 189.4 µm to 1443.4 µm for the mentioned smallest and biggest volume, respectively (see Figure 15, panel B). In conclusion, the designed and fabricated droplet-based microfluidic geometry demonstrated its capability to be integratable on the SiNW FET chip, since it offers stable droplet generation at low volume deviation between single droplets of the same applied ratio. Further, it granted reasonable volumes and lengths of emerging droplets as they passed through the serpentine structure when compared to the dimension of the SiNW FETs.

4.4.3 Microfluidic integration

Subsequently, the microfluidic system was directly integrated on the SiNW FET chip for label-free sensing microfluidic droplets. The fabricated chip consisted of an array of SiNW FETs, aligned in the middle of the chip, having their contact pads on two sides of the substrate. Additionally, large arrays of test structures were present on the substrate, which have not been used in the experiment and were removed from the design *in silico* for simpler demonstration. Further, the initial microfluidic design was slightly modulated, *i.e.* the serpentine structure was replaced by a straight channel, which was precisely aligned over the FET structure (see Figure 14, panel A). In this, the aligned main channel geometry covered both in interdigitating finger electrodes for source and drain, connected by silicon nanowires, and the surrounding Ag/AgCl top-gate electrode (see Figure 13, panel A, B and C). Here, a strong attachment of the PDMS polymer and the Al_2O_3 passivation layer for a correct droplet formation and prevention of liquid leaking had to be guaranteed. Experiments demonstrated, that the condensation reaction of Al_2O_3 and PDMS surface was possible, but less efficient than on common glass slides or silicon wafers and required overnight incubation at elevated temperatures. Thus, channel hydrophobization by immediate flushing after oxygen plasma treatment became impossible since the microfluidic cell showed strong leakage after contacting to the chip. Thus, the substrate had to be functionalized prior to plasma treatment. Since APTES does not to every single exposed –OH group on oxide surfaces[205], plasma activation and covalent binding of PDMS still remains possible. After oxygen treatment of both the APTES-functionalized FET chip (*see Chapter 3.4*) and PDMS channel system, the main channel was carefully aligned using a stereo microscope and the substrates were pressed together. In order to increase the strength of the covalent binding by the condensation reaction when the surfaces come in contact, the integrated microfluidic chip was kept at 75°C overnight on the hotplate and fixed with a little weight to ensure contact of the two surfaces. This strategy allowed direct droplet formation and sensing of propagating droplets on the chip (see Figure 16, panel D). Further, efficiency of APTES silanization on the SiNW FET substrate was tested by fluorescent labeling of the silane (see *Chapter 3.4.1*). In addition, it was essential to demonstrate that APTES did not bind to the top-gate electrode material (Ag), since it could influence the gate coupling of the gate electrode. Thus, an Al_2O_3 covered silicon wafer, partially covered with a 50 nm thick silver-

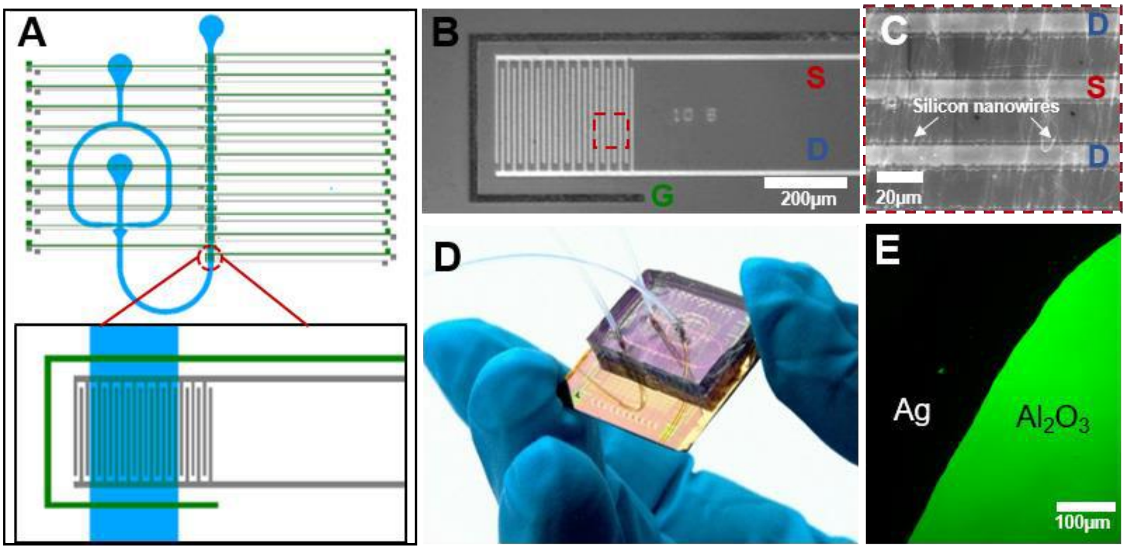

Figure 16: Integration of droplet microfluidics and SINW FETs: **(A)** Alignment of the modified channel geometry on the chip. The main channel was carefully aligned over the FET structure, covering both source and drain electrodes (grey) and top-gate electrode (green). **(B)** Microscopy image of the SINW FET. Source and drain electrodes (white) had an interdigitating geometry for a better connection of the silicon nanowires. The gate electrode structure was surrounding the source and drain electrodes and appears black after functionalization to Ag/AgCl. **(C)** SEM image of the interdigitating microelectrodes source and drain, connected by vertically aligned silicon nanowires **(D)** Real-life appearance of the integrated chip. Droplets could be directly generated and sensed on chip. **(E)** APTES fluorescent labeling with an amino modified fluorescent DNA (sequence: 5' – NH_2-(CH2)6-CAC ACT CTG TCA ACC TAC – 3' – FITC) of a blank Al_2O_3 and silver-coated Al_2O_3 surface. APTES was able to bind only on Al_2O_3 (right side) but not on silver-covered parts (left side).

layer, defined by common optical lithography, thermal evaporation and following lift-off technique, was silanized with APTES, labeled and imaged under the fluorescence microscope (see Figure 14, panel E). The pattern clearly showed, that APTES is able to bind on Al_2O_3, but is not able to bind on the silver-coated surface.

4.5 Deionized water droplet sensing

In order to evaluate the FET's response when the surrounding medium was altered, namely the propagation of an aqueous microfluidic droplet in an oil carrier phase, a single big droplet was formed in the flow-focusing region. In the following figure, the response of the FET can be seen when the droplet comes into contact with the FET. Additionally, the impact of the top-gate electrode was evaluated by comparison of the FET response controlled by the back-gate. In both gate configurations, the current between source and drain electrode (I_{SD}) was measured in real-time at constant gate voltage (V_{GS} = 1 V) and source-drain voltage (V_{SD} = 0.25 V). In the top-gate configuration, the FET showed a stable baseline when covered with non-conductive mineral oil at approximately 2.4 µA (see Figure 16, top panel). As soon as the droplet arrived, a short positive peak could be observed which then equilibrates in a plateau signal, when the water droplet was completely covering the FET, located at approximately 2.5 µA. Here, the origin of the peak was based on the required time for the top-gate electrode to build up a potential in the new phase. Finally, when the droplet left the FET, the signal went back to its initial baseline value. For back-gated FETs the impact of changing the liquid environment could also be observed but less pronounced, since the gate electrode (in this configuration the bulk) was not in contact with the liquid environment and is thus not modulated by the electrical properties of the surrounding medium. Here, the oil baseline signal was found to be at 5 nA while the water signal was at around 7 nA (see Figure 17, bottom panel), showing a low signal-to-noise ratio. In this configuration, the control via the bulk turned out to be less efficient than from the top-gate electrodes, resulting in a measurement state of the FET in off-state configuration. During the experiment, it was not possible to switch the FET to the on-state, resulting in only few I_{SD} modulations upon different ionic environments, which were only able to alter the current by direct interaction of ions in solution on the silicon nanowires. Because of the overall low current level and high noise, the top-gate geometry was used in all later experiments.

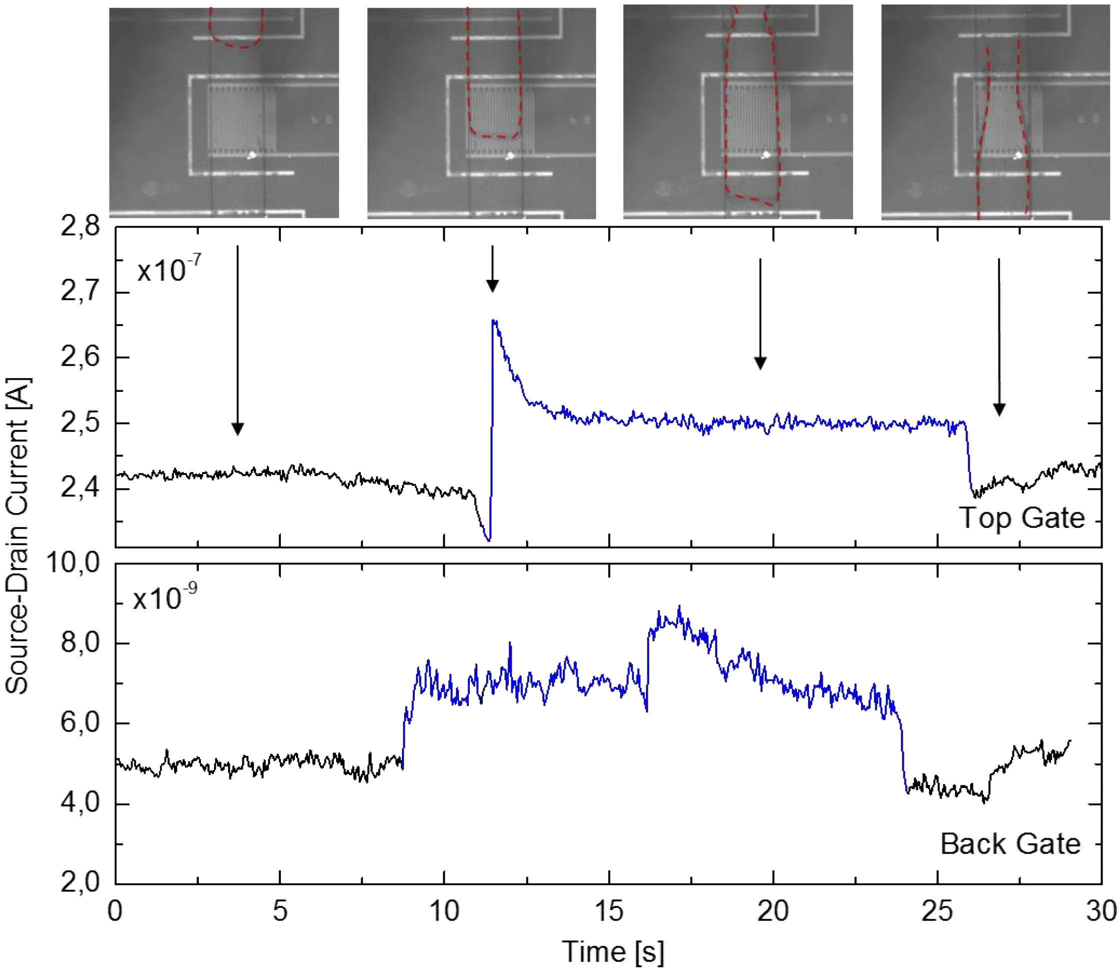

Figure 17: SiNW FET (top-gated, top; back-gated, bottom) response in the presence of non-conductive (mineral oil, black) and conductive phase (deionized water, blue). I_{SD} of top-gated FETs shows a short positive peak when the water phase is arriving on the sensor and equilibrate into stable plateau when the water is completely covering the FET and is going back to its initial baseline signal when the phase is exchanged. Back-gated FETs show the same behavior (except the peak) but at very low current levels and low signal-to-noise ratio.

Next, flowrates of continuous and dispersed were set to adequate flowrates (0.5 – 1 µl/min) for creation of water droplets in the nanoliter regime at frequencies of 1-2 Hz while detection was carried out in parallel. In this, the effect of volume and velocity of the droplets was investigated. On Figure 18, detection events of droplets with different volume and velocity can be seen. The droplet's volume was altered by changing the ratio of water and oil flow rates resulting in droplet volume of 9.9 nl and 2.5 nl for ratios of 1 and 0.1, respectively. While the signal for higher volumes showed the characteristic peaks and plateaus, the plateau was not able to form for smaller droplets (see Figure 18, bottom, left). Here, the presence of the water droplet on the FET was too short and the top-gate electrode was not able to form a potential in the new phase. Thus, only the peak formation could be seen. The effect of peak and plateau formation dependent on the time period of the droplet on the sensor will be discussed in *Chapter 4.6.2*. Following, the effect of velocity was investigated. Here, the highest velocity, which could be obtained without breaking of the system, was located at 12,7 µm/ms. With a flow rate ratio of 1, a frequency of approximately 2 Hz could be observed with a droplet detection efficiency of 100%. Keeping the flow rate ratio constant, lower velocities reduced the frequency to approximately 0.5 Hz with the same detection efficiency. Further, the capability of the device to a higher throughput was demonstrated by detection of droplets at different frequencies. In this, droplet frequencies up to 10 Hz could be achieved by carefully increasing both water and oil stream flow rates (see Figure 19). However, at higher frequencies, only the peak signal of the droplets could be observed. Applying higher flowrates causing more than 10 Hz droplet formation caused defects in the droplet formations by oil leakage into the water inlet and non-homogeneous droplet formation. While the SiNW FET was able to detect every droplet at every achieved frequency, the throughput limit is set by the microfluidic design. In order to achieve faster droplet formation, the microfluidic channel geometry has to be optimized.

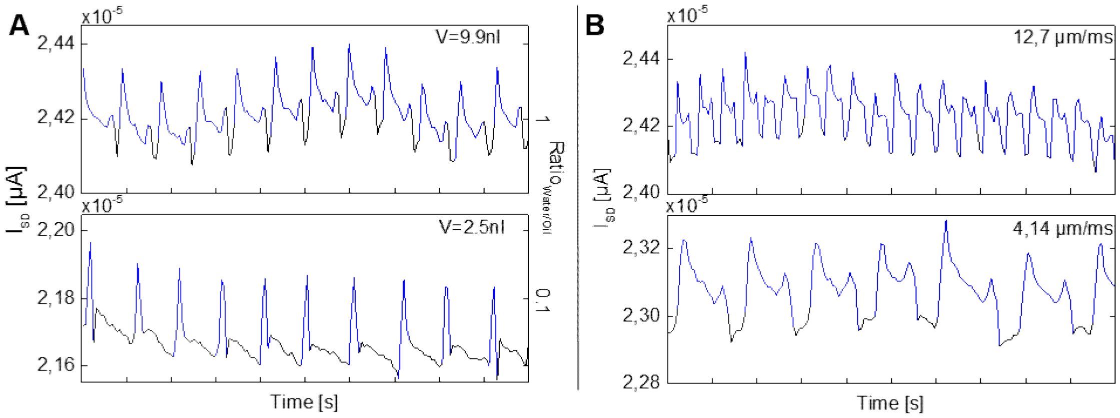

Figure 18: Effect of droplet volume and velocity on the detection signal: **(A)** Effect of droplet volume: While for bigger droplets both peak and plateau signal could be seen, the plateau was not able to form for small droplets. **(B)** Effect of droplet velocity: Also for the highest observable flow rate, a complete droplet signal was observed, if the droplet was big enough. The detection efficiency was located at 100%.

4.6 Phosphate-buffered saline (PBS) droplet sensing

4.6.1 Influence of the droplet's ionic concentration

In order to optimize the droplet detection and to strengthen the platform's impact in biological assays, the droplet's liquid was exchanged from deionized water to conventional buffer liquid, namely phosphate-buffered saline (PBS). PBS is commonly used in biological assays and research, which is able to establish a constant pH in liquid environment and consists of disodium hydrogen phosphate (Na_2HPO_4), sodium chloride (NaCl), potassium chloride and potassium dihydrogen phosphate (KH_2PO_4). The most common ionic concentration is set at 10 mM (1x), which matches the ionic environment of the human body, where the strongest impact is caused by NaCl (137mmol/l). The comparison of one single droplet detection of deionized water and 0.1x PBS can be seen on the following figure. For deionized water, the plateau signal for the droplet was not well defined and had a negative tendency to the oil baseline level till the droplet was leaving the sensor. In comparison, the increase of the ionic concentration in the droplet phase caused a quick and stable formation of the droplet signal after few tens of milliseconds (see Figure 20). Here, the arrangement of a stable baseline was based on the formation of a stable potential between the Ag/AgCl top-gate electrode and the semiconducting nanowires. With a liquid layer between them, the accumulation of charges/holes at the oxide surface was dependent on the ionic strength of the liquid layer and became strongly stabilized by the presence of ions in the liquid. While for deionized water no ions were present, there was a high amount of ions in PBS, mainly introduced by the salt NaCl. Thus, this

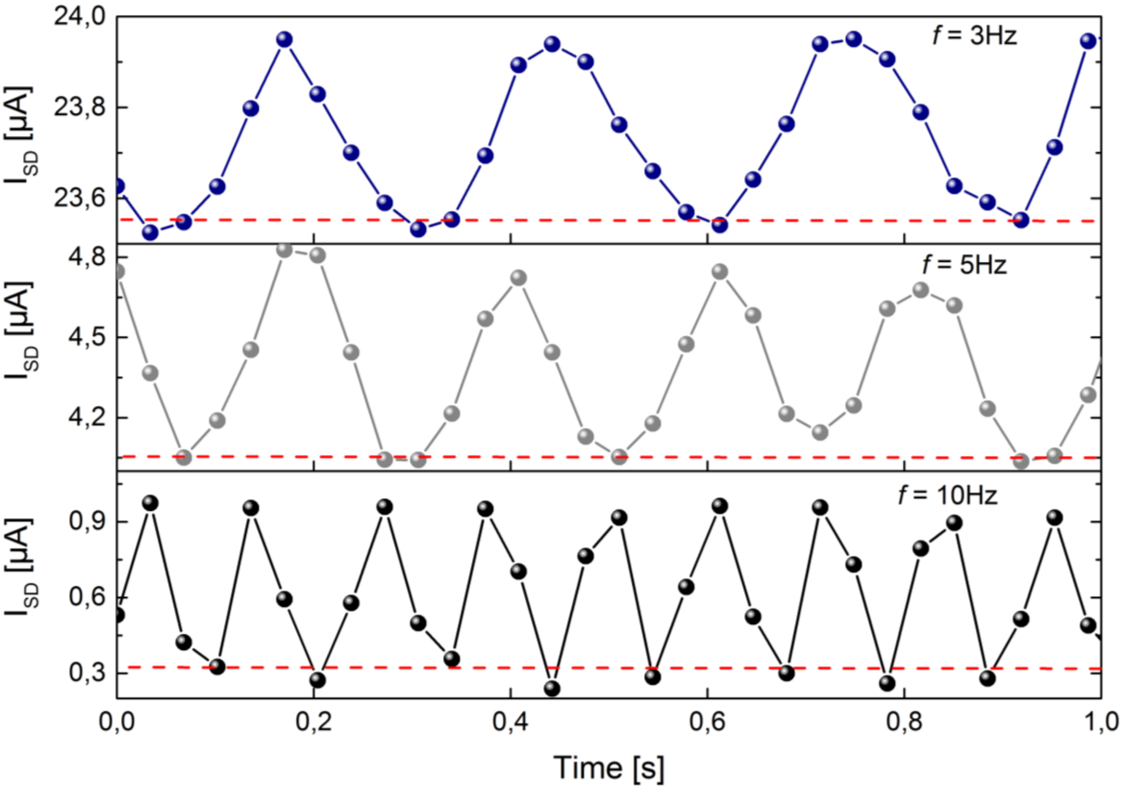

Figure 19: Droplet detection at frequencies ranging from 3 to 10Hz. In this, the microfluidic channel geometry was not able to achieve higher droplet rates and it is thereby the limiting factor in the spirit of high-throughput detection.

introduction of ions into the droplet phase granted defined formation of the droplet signal and increased the impact of the developed platform in the spirit of biological assays, tests and research. In the following, the droplet size and velocity was analyzed in context of stable plateau formation. Here, the combination these two parameters can be expressed as the time of the droplet on the sensor.

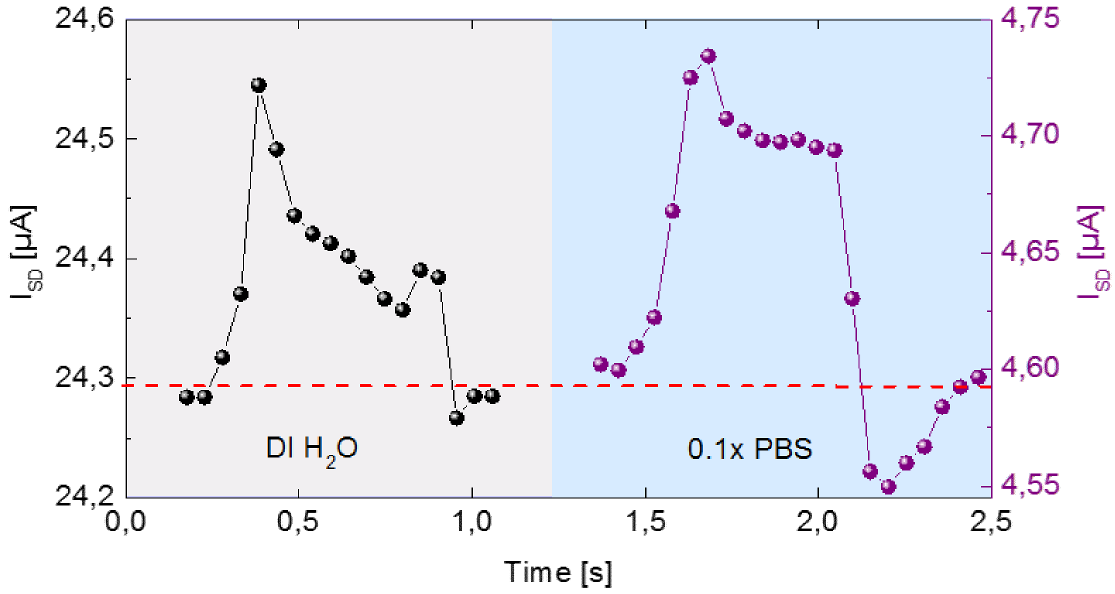

Figure 20: Direct comparison of droplet plateau formation with different ionic concentrations of the dispersed phase. While no stable plateau signal formation could be observed for non-ionic liquids (deionized water, left side), a stable plateau formation after few tens of milliseconds could be observed for higher ionic liquids (0.1x PBS, right side). The formation of a stable plateau signal was related to the formation of a stable potential between top-gate and source electrode. Here, the gate coupling to the semiconductor was strongly improved for ionic liquids.

4.6.2 Plateau formation in dependence of the droplet's settling time

Subsequently, the impact of the time duration of the dispersed phase on the FET sensor was evaluated. Here, this time was directly proportional to the droplet size at fixed velocity. For deionized water, three different droplet volumes were analyzed with respect to the ratio of plateau signal and peak signal. In this, the volume could be also expressed in length of the droplet since they are confined in a fixed geometry (300 µm channel width and 15 µm height). The analyzed volumes can be seen on the following figure and were set to: 1.9 nl, 3.7 nl and 9 nl. With respect to the sensor geometry, 1.9 nl droplets were approximately as long as the sensor, 3.7 nl droplets were slightly longer, while 9 nl droplets were able to cover the whole FET for a longer period, indicated by the yellow area in Figure 21, panel A. In this, the ability to cover the FET completely directly reflected the formation of a plateau signal. In the sensing event, 1.9 nl droplets were only able to cause a short peak in the source-drain voltage (I_{SD}) and left the FET, before a stable potential in the new gate configuration was achieved. In contrast, 9 nl droplets were able to form a plateau since the droplet's presence was long enough for an efficient gate coupling. Droplets, which were slightly longer than the sensor length (3.7 nl) resembled a transition point with a very weak droplet plateau signal. In order to quantify these observations, the peak-to-plateau ratio was calculated. This parameter defines, if the droplet plateau signal is formed by demonstrating a stable appearance (see Figure 21, panel A, blue and red arrows). For deionized water a strong drift from higher to lower ratios was observed. For very small droplets, the ratio was rather high (1.016) showing that the plateau signal was very low and close to the baseline of the continuous phase. This ratio was decreasing for bigger droplet volumes demonstrating the formation of a plateau signal (see Figure 21, panel B, blue data points). For deionized water, no stable plateau signal for adequate droplet sizes was achieved since the peak-to-plateau ratio was shifted even for droplets with higher length and got only stabilized for droplets, which were present for tens of seconds on the sensor (see *Chapter 4.5*, Figure 18). In contrast, droplets with higher ionic concentrations, namely 1x PBS droplets, were able to form a stable baseline independently from their droplet size (see Figure 21, panel B, red data points). Here, even for droplets which were shorter than the sensor, the ionic contribution was strong enough to

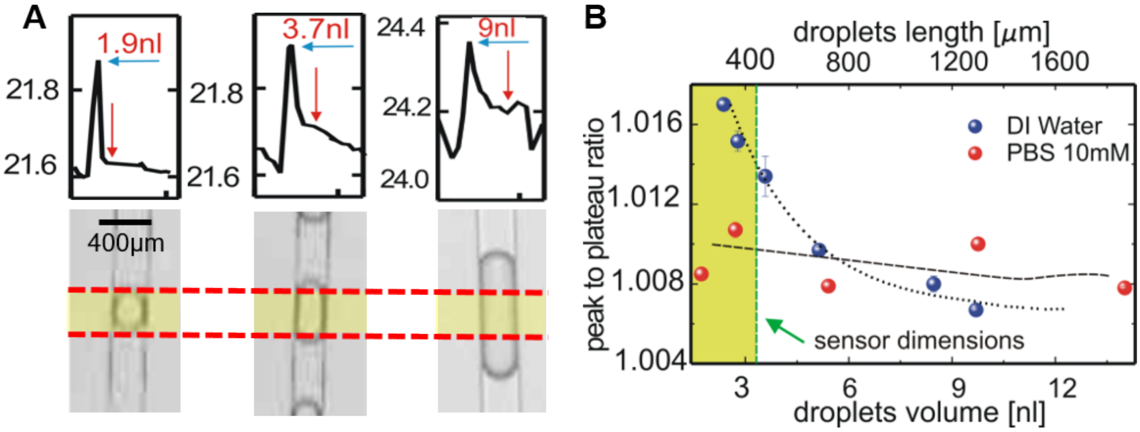

Figure 21: Analysis of the droplet size on the sensing efficiency: **(A)** Resulting signal of deionized water droplets of different sizes. Here, small droplets were not able to form a plateau signal of the droplet phase. **(B)** Accompanied visual comparison between droplet and sensor length. Here, 1.9nl droplets were as long as the sensor, 3.7nl droplets were slightly longer and 9nl droplets were able to fully cover the FET for longer time. Calculations of the peak-to-plateau ratio of both deionized water and PBS droplets demonstrated no stable baseline for deionized water droplets, while PBS droplets formed a stable plateau signal independently of their sizes. In this, the trend lines are only a guide for the eye.

form a stable droplet plateau, reflecting in a stable peak-to-plateau ratio. Here, the PBS droplet detection was not limited by the microfluidic system but by the electrical performance of the FET. In conclusion, introduction of ions in the dispersed phase resulted in a stable droplet plateau signal and greatly enhanced the efficiency of the developed sensor platform. Further, for an efficient sensing of the interior droplet composition, the droplets had to form a reasonable plateau after the peak, which reflected the real signal of the droplet phase. Thus, following sensing experiments were carried out in a flow ratio of 1, resulting in PBS droplets of approximately 10nl.

4.6.3 Droplet analysis by their ratio

In order to strengthen the evaluation of the FET response towards propagating droplets, the current change of the nanowire FET platform was expressed in a dimensionless ratio between the current levels of the droplet signal and the mineral oil baseline signal. This strategy allowed analysis of microfluidic droplets independently of possible signal drifts during the measurement. A representative analysis can be seen on the following figure. Here, plateau signals of droplets (blue stars) were divided by the oil baseline signal (yellow stars) (see Figure 22, panel A). Doing so, a representative ratio representation of the two phases could be achieved. The calculation of the ratio was carried out using a histogram plot of 20 independent droplets in row. In this, the droplet's plateau signal and the oil baseline signal could be identified based on their degree of presence: aqueous signal plateau level (see Figure 22, panel B right side) since the ratio remains stable in a distinct composition of droplets (Here: 1x PBS) and mineral oil level

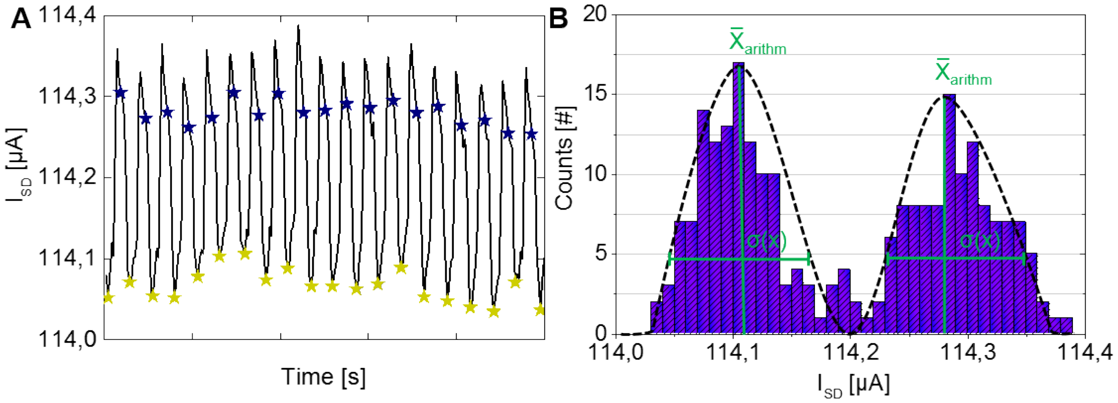

Figure 22: Representative calculation of the dimensionless ratio between droplet phase and oil carrier phase. **(A)** Raw data signal of 1x PBS droplets (blue stars) in mineral oil carrier phase (yellow stars) in a 1:1 flow ratio. **(B)** Accompanied histogram of the raw data. The peaks represent the signal values for mineral oil carrier phase (left) and droplets (right side).

(left side). Next to the change of the alteration of the droplet's liquid to a biological buffer, the sensitivity of the device with respect to chemical parameters was explored, namely various pH values and molar concentrations of droplets in physiological environments. Here, pH changes in liquid bacterial environments can give insights into the metabolic activity of living organisms and act as an indicator of bacteria or cell survival (see *Chapter 2.5.2*). Here, a sensitivity towards different pH values of passing droplets on the sensor give rise to explore the survival of single isolated bacteria or several bacteria in droplets in presence of *e.g.* antibiotics or toxins. Second, tracking of the kinetics of chemical reaction, which alter the pH of the solution, can be achieved. Third, tracking of ionic concentrations represents a measurement method to track metabolites in solution as well as observation of bacteria and cell destroying components causing lysis of microorganisms. By this lysis, the highly ionic cell or bacteria cytosol[206] will be exposed to the liquid media of the droplets causing an increase in the ionic concentration. In the following, both pH values and ionic concentration sensitivities were explored in physiological environments.

4.6.4 Dependence on pH value

For the evaluation of the FET response dependency on the pH value of droplets, different aliquots of 1x PBS solution (initial pH: 6) were modified with respect to their pH values by addition of either NaOH for higher pH values or HCl for lower pH values. Here, PBS aliquots were set to physiological relevant pH values ranging from 4-8. Following, the individual liquids were guided to the microfluidic system and the signal was recorded. In order to minimize contamination, which could influence the signal, approximately 25 µl of the individual PBS aliquots were pulled in a long teflon tube one after another and the experiment was carried out in one single run by continuous pushing of the droplet phase in the microfluidic system. Like in the previous droplet sensing experiments, the response signal of the FET (I_{SD}) was recorded in dependence of the time at constant $V_G = 1$ and $V_{SD} = 0.25$. A composite plot of droplets with different pH values can be seen on the following figure (see Figure 23, panel A). Here, droplets with the highest pH value (pH 8) demonstrated the highest baseline level. As soon as the pH value of the droplets is decreasing, the baseline equilibrates at lower values, namely ~114.2 µA for pH 8 and ~112.25 µA for pH 4. In this, all tested pH values showed different baseline values, making the device sensitive to the amount of H^+ ions in solution and giving rise to act as a biosensor. Further, also the numerical difference of discontinuous and continuous phase should be dependent on the pH values. Thus, the ratio of the plateau signal of the droplets with different pH values to the oil phase was calculated (see Figure 23, panel B). Here, a clear trend of the ratio in dependence of the pH values could be observed. As soon as the droplet's pH values is increasing, the ratio of plateau to baseline was decreasing from a value of 1.0018 for pH 4 to 1.0013 for pH 8. By pure analysis of the ratio, the shift of the baseline can be neglected, giving rise to a distinct classification of pH values in droplets. Here, the difference of the sensor's response to various pH values was additionally based on the device' functionalization with APTES. In this, the silanization of the sensor caused a layer of exposed NH_3 groups on the surface. In presence of lower pH values, this group was protonated to NH_4^+ causing a shift of the energy bands between source and drain in the band diagram. Here, the bands were lowered causing a lower activation energy for electrons to travel from source to drain. This effect will cause an increase in the signal strength for lower pH values. In conclusion, the platform showed reliable sensitivity towards alterations of pH values in moving droplets and can thus be utilized for *e.g.* bacteria survival assays in droplets.

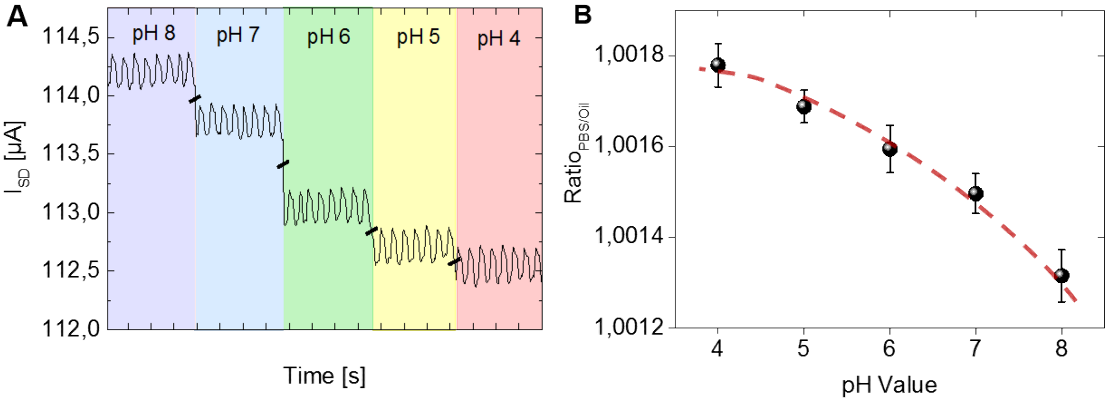

Figure 23: Dependence of sensor response on the pH value of passing PBS droplets: **(A)** Higher pH values give rise to elevated baseline of the source-drain current of the FET. As soon as the droplet pH value is decreasing, the baseline is also shifted to lower levels. **(B)** Ratio analysis of droplets with different pH values by division of the plateau signal and its corresponding oil signal baseline. Here, droplets with higher pH values cause a decrease of the ratio.

4.6.5 Long time pH sensing experiment

The developed combination of droplet microfluidics and silicon nanowire field effect transistors additionally supported long-time experimental data collection, as shown on the following figure. Here, the full data set from the experiment in the previous chapter can be seen, where PBS droplets with various pH values were guided to the SiNW FET in one single run. Within a timespan of nearly one hour, the complete liquid phase was guided to the microfluidic system, cut into individual droplets and detected by the FET. Starting from a pH value of 8, the signal was significantly dropping when the next phase was guided into the system. Because of the absence of separation layers, the signal was gradually changing to the new level because of occurring diffusion between the phases in the tube. In total, around 6300 droplets were captured with a rate of approximately 1 Hz. In this, the individual pH value levels were clearly visible, separated by a drifting region between the pH values. The experiment demonstrated that the sensor was able to be used in long-time experiments, essential for biological assays. After the measurement, the chip could be cleaned and reused several times.

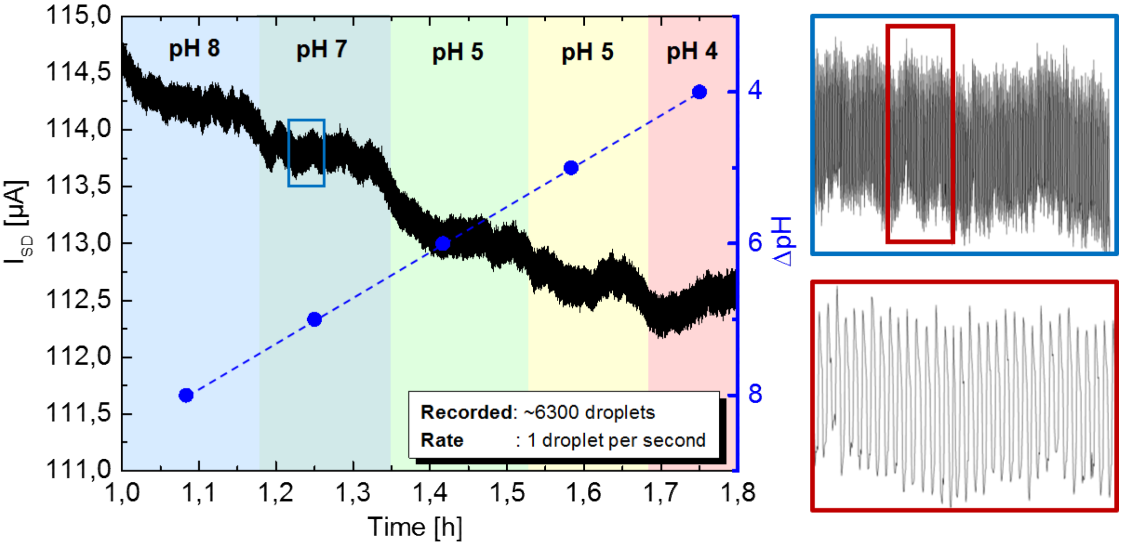

Figure 24: Longtime experiment of droplet sensing using SiNW FETs. In total, ~6300 droplets were detected with a rate of 1 Hz in nearly one hour. The represented data showed the droplet signal for a series of PBS buffers with different pH values. Here, the signal was changing to the new phase level because of the lack of separation layers between the phases in the tube. Reference pH value of the individual phased was measured in advance with a conventional pH meter.

4.6.6 Dependence on ionic concentration

In addition to the evaluation of the sensor response in dependence of the droplets' pH value, the influence of the ionic concentration on the FET response was evaluated. For this, PBS solution with a concentration of 10mM was diluted to 1 mM, 0.1 mM and 0.01mM with deionized water (0.1x, 0.01x and 0.001x, respectively). Like in the pH value sensitivity experiment from the previous chapter, probes of the different aliquots were pulled in a long tube, guided to the droplet phase and the sensor signal was recorded in dependence of the time at the same FET configuration. On the following figure, the sensor response can be seen for the different ionic concentration of PBS droplets. Here, the lower the molar concentration, the higher current level was, namely ~5 µA for 0.001x, ~4.5 µA for 0.01x, ~4.4 µA for 0.1x and ~4 µA for 10 mM (see Figure 25, panel A). This effect was related to the Debye length in ionic environments. Here, higher ionic liquids formed a shielding layer around the semiconducting elements of the FETs by electrical attraction and repulsion of ions in the solution. In total, less charge carriers were present, when the ionic concentration was increasing, hindering an efficient gate coupling between gate and source electrode and resulting in a decrease of the current between source and drain[207,208]. This effect could be additionally seen in the analysis of the ratio between droplet phase and oil baseline signal. Here, the lower the ionic concentration, the higher the absolute difference between the two phases from a ratio value of 1.004 for 1x PBS to 1.0204 for 0.001x PBS (see Figure 25, panel B). In summary, both pH value and ionic concentration of the microfluidic droplets had an impact of the sensor's signal output, forming the backbone of an adequate sensor platform for biological assays, where these two parameters play an important role.

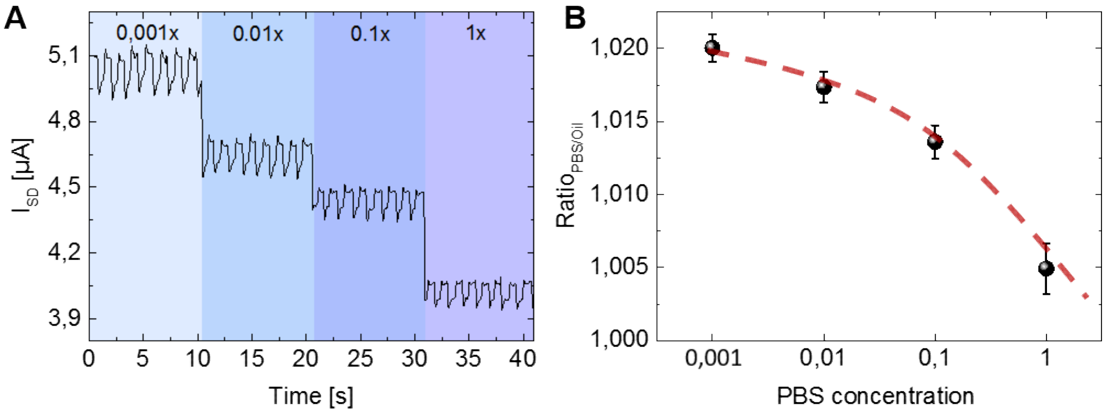

Figure 25: Dependence of the sensor response of passing PBS droplets with different ionic concentrations. **(A)** The lower the ionic concentration of passing droplets, the higher is the absolute sensor signal level. Stepwise increase of the concentration showed stepwise decrease of the signal level. **(B)** Ratio of passing droplets and their corresponding mineral oil baseline level was also dropping, if the ionic concentration is increased. Here, higher ionic liquids resulted in a larger Debye-length between the gate and the silicon nanowire, causing a drop in the overall conductance of the FET.

4.7 Tracking of reaction kinetics in droplets

4.7.1 *Principle and setup of the glucose oxidase (GOx) enzymatic test*

In order to demonstrate the impact of the developed sensor platform for biochemical and biological assays, the kinetics of a chemical reaction in propagating droplets was tracked, namely the glucose oxidase (GOx) assay for the detection of glucose. The enzymatic reaction principle can be seen on Figure 26. In the presence of oxygen, the enzyme GOx hydrolyzes glucose to D-gluconic acid, leading to a time-dependent acidification of the surrounding buffer. Next, this enzymatic reaction was coupled to a second reaction for a parallel optical observation. This reaction involved horseradish peroxidase (HRP) which oxidizes a chromogenic substrate like 3,3’,5,5’ tetramethylbenzidine (TMB) into $TMBH_2$ in the presence of hydrogen peroxide (H_2O_2) formed during the initial reaction. This oxidation resulted in a color chance from clear to blue. For evaluation, the droplet phase was probed with glucose, GOx, TMB and HRP, and guided into the droplet inlet of the microfluidic system. Here, formed droplets from this solution were guided to the FET structure and the signal was recorded. For detection, the SiNW FET chip was replaced with a silicon-based FET chip, where the source and drain electrodes were not connected by straight silicon nanowires, but with honeycomb-structured silicon nanowires (HCNW), provided by our research collaborators at Pohang University of Science and Technology (POSTECH), “Department of Creative IT Engineering”[209]. In short summary, this platform consisted of 50 nm wide HCNW, defined by EBL on a SOI wafer, which was

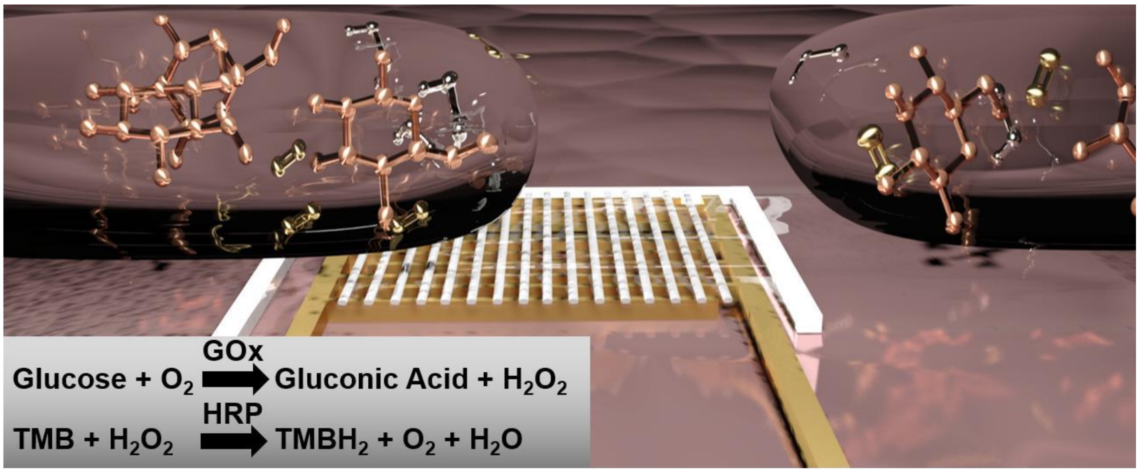

Figure 26: Enzymatic reaction principle in microfluidic droplets. The droplet phase was probed with glucose, glucose oxidase (GOx), horseradish peroxidase (HRP) and TMB. The reaction caused an acidification and a color change from clear to blue of moving droplets, where each droplet represents one specific time step of the reaction, when it passes the sensor.

connected to source and drain electrodes by 100 nm thick As-doped top-silicon. Further, the devices were equipped with a 200 nm thick silver gate electrode and passivated by a 500nm thick SiO_2 layer. This geometry gave rise to higher current stability and higher signal-to-noise ratio at the exponential subthreshold voltage regime[210–214]. Since the reaction was continuing in droplets and they passed the sensor one-by-one, each droplet represented an individual time step of the reaction.

4.7.2 GOx enzymatic assay

Initially, the droplet phase was probed with 2 mM glucose in deionized water and 2mM TMB in a ratio of 1:1 in phosphate citrate buffer (pH 7) containing 3.3% GOx and 1.6% HRP. Here, the percentage of enzyme was chosen to be at the same level by equilibration based on their enzymatic activities. Doing so, formed droplets in the microfluidic systems contained 1mM glucose and 1mM TMB. In advance, a reference measurement was carried out containing the signal collection of reference droplets with phosphate citrate buffer without GOx enzyme at different pH values and accompanied ratio calculation $R_{Droplet/Oil}$ (see Figure 27, panel B black line). In order to examine the pH value shift during the reaction, $\Delta R_{Droplet/Oil}$ was calculated by subtraction of $R_{Droplet/Oil}$ of passing droplets during the reactions from the initial droplet-to-oil ratio before the reaction (R_0). In this, R_0 was only valid for the observed reaction and possess positive values for alkalization processes and negative values for acidification processes (R_0 = 1.085, corresponding to a pH value of approximately 6) (see Figure 27, panel B blue line). Based on these calculations, the kinetics of the chemical reaction could be observed, containing a significant acidification of droplets when the reaction was happening as well as a re-equilibration to the initial pH value because of the buffer system. Here, the reaction and re-equilibration lasted for approximately 100 seconds with a change of 2 pH values (see Figure 27, panel A and B). Regarding the parallel readout, a cold spectrum LED was focused onto the transparent fluorinated ethylene propylene (FEP) tubing containing the emulsion. For readout, a fiber coupled spectrometer was used for measurement of the absorbance. Here, the time-dependent color change of the solution acted as a filter blocking the yellow wavelengths of the LED causing a decrease in intensity (see Figure 27, panel C). Finally, the proof that the signal change was exclusively accompanied by the decomposition of glucose, the effect of the glucose

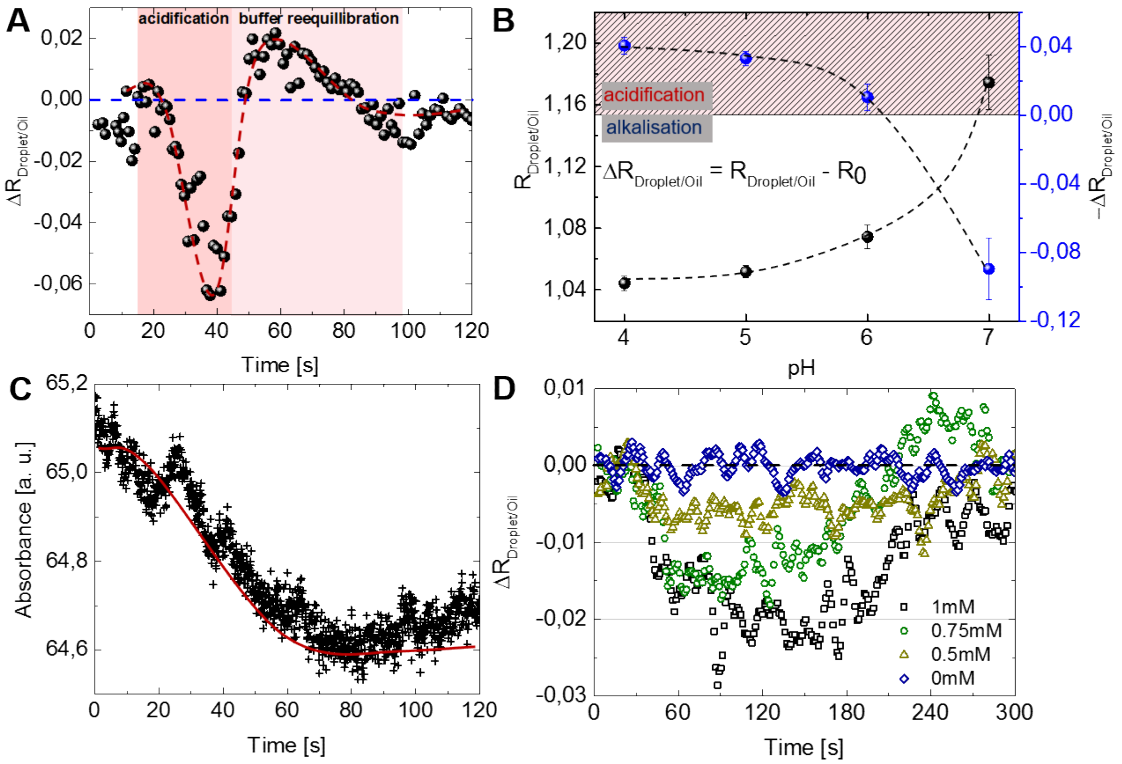

Figure 27: Label-free tracking of GOx reaction in multiple droplets: **(A)** Time-dependent change of pH in droplets, probed with the various chemicals, represented by the change of droplet-to-oil ratio. Enzyme-driven reaction of glucose to gluconic acid leads to an acidification of the droplets (pink region), followed by a re-equilibration of the pH by the buffer system. **(B)** Reference droplet -to-oil ratios of droplets with various pH values ($R_{Droplet/Oil}$) and calculated pH changes in dependence of the droplet-to-oil ratio before the reaction ($\Delta R_{Droplet/Oil}$) **(C)** Accompanied color change of the solution in optical absorbance readout. **(D)** GOx assays in presence of various concentrations of glucose.

concentration was evaluated in the range from 0 mM and 1 mM. Here, a clear dependency of the magnitude of pH changes to the concentration could be seen. While the highest concentration resulted in the most pronounced pH change, it was shrinking when the concentration was lowered (see Figure 27, panel D).

4.8 Stable baseline by conductive carrier phase

Further improvement of the combined platform included the formation of a stable baseline to improve sensitivity towards quick and large pH changes of propagating droplets. Since the level of the baseline of the described sensor was dependent on the pH value of the present droplet, it could not differentiate between *e.g.* two subsequent droplets with large differences in their pH values, since the baseline needed to equilibrate in the first place. Instead, a stable baseline guaranteed the detection of different pH values since only the height of the droplet peak changed in accordance with the pH value of the droplet. In order to achieve a stable baseline, a stable gate coupling in the continuous phase was mandatory, requiring the change to a conductive continuous liquid immiscible with water. Here, orthodichlorobenzene (oDCB) was chosen due to its immiscibility with water, as well as its higher electrical conductance compared to mineral oil. On Figure 28, the signal for PBS-in-oDCB droplets with different pH values (4, 6 and 8) can be seen. Here, using oDCB as continuous phase, a stable droplet formation could not be achieved as can be seen on the irregular droplet signal. However, the efficient gate coupling in the carrier phase led to a stable baseline between PBS droplets with different pH values, where their differentiation was based only on the height of the droplet signal. Thus, using a conductive carrier phase allowed formation of a stable formation of the sensor baseline enabling sensitivity towards fast pH alterations in propagating droplets.

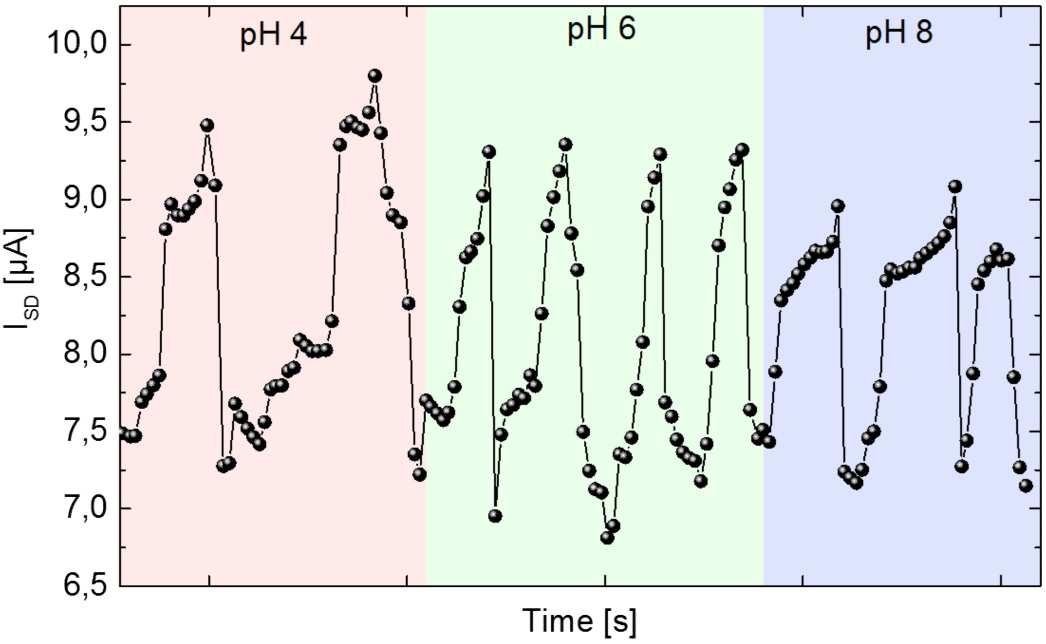

Figure 28: FET sensor response to PBS-in-oDCB droplets with different pH values. The introduction of a conductive continuous phase caused a stable baseline allowing improved sensitivity towards fast pH alteration in propagating droplets. In this, a trend could be observed of the droplet ratio in dependence of the pH values: the higher the pH value, the smaller the ratio becomes.

5. Impedance-based flow cytometer on a chip

5.1 Overview

In disease diagnostics, a broad variety of various methodologies can be found, which allow detection of various kinds of disease markers. For instance, the majority of today's medical and biochemical diagnostics and detection of cells, bacteria or molecules is based on optical detection by *e.g.* (immuno-)fluorescence (IF) or fluorescence-activated cell sorting (FACS) (see Figure 29, panel A). However, the trend in current investigation in the biological sensing community goes towards optics-less sensing, since it does not require expensive labels and bulky microscope analysis, granted by *e.g.* electric impedance spectroscopy (EIS) and electric impedance cytometry (EIC) (see *Chapter 2.3*). In the second part of the results, the prototyping of a complete sensor platform from scratch is demonstrated. Here, the sensor is based on the EIC methodology on a lab-on-a-chip format. It resembles the conventional flow cytometry principle, but offers several advantages including electrical and optic-less detection of micron-sized analytes without any labels at low sample preprocessing. The platform consists of an array of interdigitating nanowire electrodes over which the analyte solution is comprised via a microfluidic hydrodynamic focusing system (see Figure 29, panel B). During operation, the sensing mechanism is purely based on the electric properties of the passing analytes, *i.e.* their impedance and dielectric properties, as well as their sizes. It is the first time, that EIC is used in combination with nanostructured sensing geometries, allowing a higher sensitivity of the detection of passing analytes.

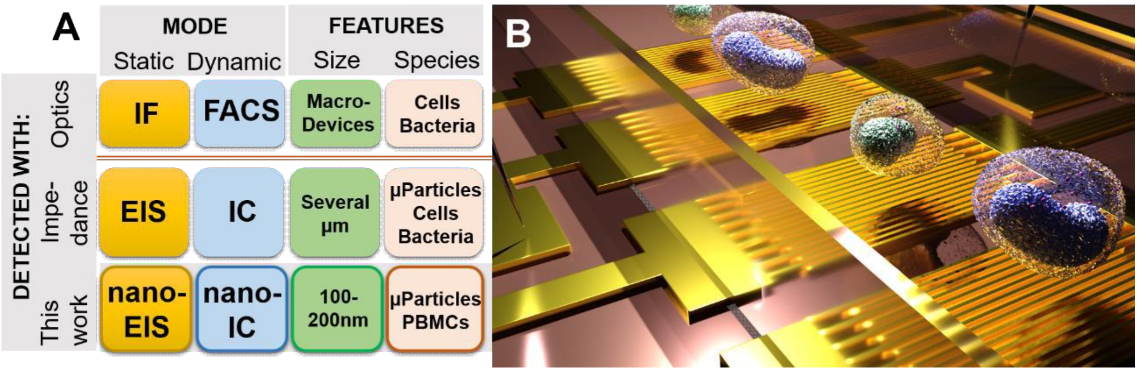

DETECTED WITH:	MODE: Static	MODE: Dynamic	FEATURES: Size	FEATURES: Species
Optics	IF	FACS	Macro-Devices	Cells Bacteria
Impe-dance	EIS	IC	Several µm	µParticles Cells Bacteria
This work	nano-EIS	nano-IC	100-200nm	µParticles PBMCs

Figure 29:. **(A)** Contribution of the nanowire sensor platform to previously reported and state of the art techniques, *i.e.* (immuno-)fluorescence (IF), fluorescence-activated cell sorting (FACS), electrical impedance spectroscopy (EIS) and impedance cytometry (EIC). **(B)** Scheme of PBMC detection by nanoimpedance cytometry.

5.2 Overview of the fabrication of the sensor device

This subsection focuses on the demonstration of the general fabrication steps in an overview fashion. The detailed procedures for every step will be demonstrated and discussed in the following paragraphs. The general steps in the fabrication of the small scaled sensor platform consist of the patterning of the nanosensing structure using EBL (A), its development and pattern transfer using dry etching technology (B), the contacting of the nanostructure with microelectronic structure (C) and the integration into microfluidic geometries (D) (see Figure 30). In the presented work, each step was developed, evaluated and optimized to meet the requirements for the correct function as a biosensor. In the following list, a more detailed demonstration of the various steps is shown, *i.e.* the nanofabrication of the sensor element (I), its connection to the microelectrode geometries (II) and the microfluidic integration (III).

(I) Fabrication of the nanosensing geometry

  a. COMSOL Multiphysics® simulations for evaluation of the most adequate sensing structure, nanowire arrangement, electrode distances, working potential and number of nanowires.
  b. Electron-sensitive resist patterning using EBL, its parameters, development and optimal protocols for high-yield patterning, as well as its transfer to underlying metallic layers.

(II) Contacting of nanostructures to microstructures for connection access

  a. Sensor design for contacting of multiple sensing structures.
  b. Optical lithography strategy and parameters for efficient contacting of the structures.

(III) Microfluidic integration

  a. Hydrodynamic focusing design to guarantee analyte delivery to the sensing structures.
  b. Integration of the channel geometry on the sensor and its fabrication steps.

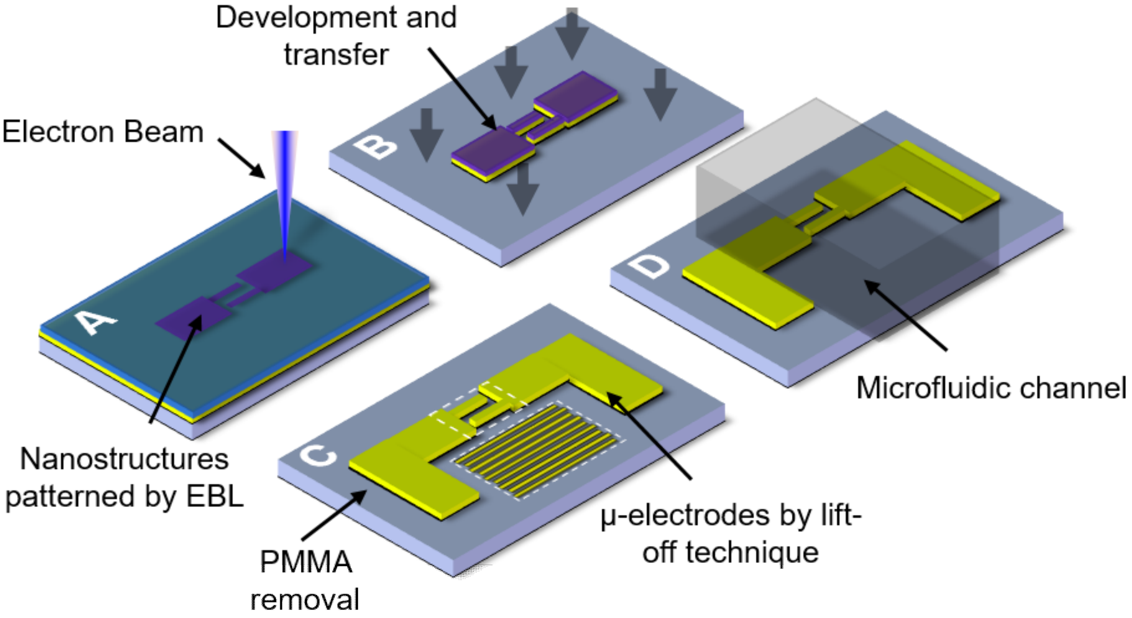

Figure 30: General fabrication steps of the sensor platform: **(A)** EBL patterning of electron-sensitive resist in negative fashion. **(B)** Pattern transfer of the pattern to the underlying layer using dry etching technology **(C)** PMMA etch mask removal and subsequent contacting with microelectronic structures for later positioner contacting. **(D)** Microfluidic integration of the channel system directly on the chip using radical oxygen plasma treatment.

5.3 COMSOL simulation of sensing area

5.3.1 Prototyping of the sensing geometry

In order to evaluate the most suitable nanoelectronic design for sensing, the electrical behavior of various micro- and nanogeometries were simulated using COMSOL Multiphysics®. In this, the aim focused on the development of a geometry showing a homogeneous and strong electric field in order to guarantee reliable and identical signal alterations, when same types of analytes were present in the area of influence. In the following figure, four different designs can be seen, which were analyzed towards their capability to be used as a sensing element by numerical simulation of the electric field, when an electrical potential was applied. In the simulation, a potential of 1 V was set between the electrodes (left: 1 V right: ground) and a color map indicates the strength of the arising electric field and the potential drop to the ground. The electrodes material was set to gold, while the substrate was defined as borosilicate glass. Firstly, a geometry of two opposing microelectrodes were investigated with 30 µm in length and 35 µm in width, separated by a 10 µm gap. These values were chosen, since analytes were visionized to have their diameters close to the gap size, passing a longer detection “channel”. In this configuration, the potential dropped homogeneously between the source and ground electrode, indicated by the color code change from red to blue. However, the applied potential only created a weak electric field, which strength was mainly found at 1x10^5 V/m (see Figure 31, panel A). At the edges of the electrodes, a small increase in its strength could be observed (1.2x10^5 V/m), adding inhomogeneity the electric field distribution. Thus, the microelectrode setup was not suitable to be used as a sensing geometry. Next, the gap between the microelectrodes was increased to 50 µm and single opposing nanowire geometries (width of 100 nm) were introduced in the center (see Figure 31, panel B) at the same gap distance of 10 µm. By using nanosized geometries, the magnitude of the strength of the electric field could be doubled, reaching 2x10^5 V/m. However, this field strength was only located at the very tips of the nanowires, while being very low while crossing the gap. Further, this effect was also present if the total number of nanowires is increased up to five opposing nanowire pairs (see Figure 29, panel C). The spot-size increase of the electric field was still present, while the electric field in the gap is slightly

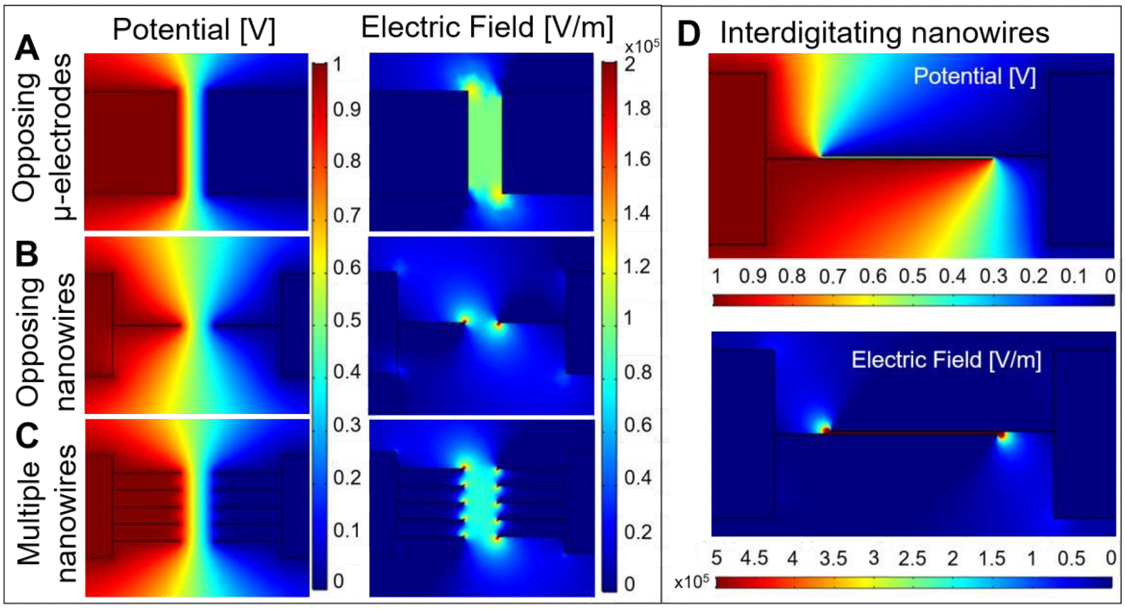

Figure 31: Identification of the most appropriate nanoelectronic structure by COMSOL Multiphysics® simulations. **(A)** Opposing microelectrodes with a distance of 10 µm caused an inhomogeneous electric field with a maximum value of 1.2 V/m. **(B)** Opposing nanowires (50 nm width) with a gap of 10 µm caused an inhomogeneous electric field with maximum value of 2 V/m at the nanowire tips. **(C)** Multiple opposing nanowires with the same gap distance. As observed for one opposing pair, only a local field enhancement at the nanowire tips could be observed. **(D)** Interdigitating nanowires with a pitch of 1 µm. This geometry granted a homogeneous electric field with a magnitude of up to 5 V/m.

increased, but still showed too low strength in total (at approximately 0.8×10^5 V/m). Thus, also the opposing nanowire geometry was not suitable for the sensor design. Following, the design was changed to a mode, where the nanowires were overlapping each other between the electrodes, separated by a thin gap of 1 µm between them (see Figure 31, panel D). In this configuration, the interdigitated mode, the forming electric field was strongly enhanced to a value of 5×10^5 V/m. Further, compared to the opposing nanowire configuration, the maximum value was homogeneously distributed between the gap of the nanowires and only dropped at the very edges of the nanowire tips. Because of the homogeneous high electric field coverage of this configuration, it was chosen to be the geometry of choice and was further used for several optimization steps, which are described in the following chapters.

5.3.2 *Optimization of the sensing geometry*

Subsequently, geometry optimizations were simulated using the interdigitated nanowire configuration in the spirit of electric field strength and area maximization. In this, inter-electrode distances, namely the edge-to-edge distance between the nanowires (the pitch) and also the distance between nanowire tip and opposing microelectrode were tweaked (see Figure 32). Firstly, the dependency of the pitch distance on the electric field strength was elucidated, while the minimum tip-electrode distance was searched, which directly affects the sensing area, without current leakage between tip and electrode. Here, the pitch distance was altered to 1 µm, 0.5 µm and 0.1 µm, while the distance from the

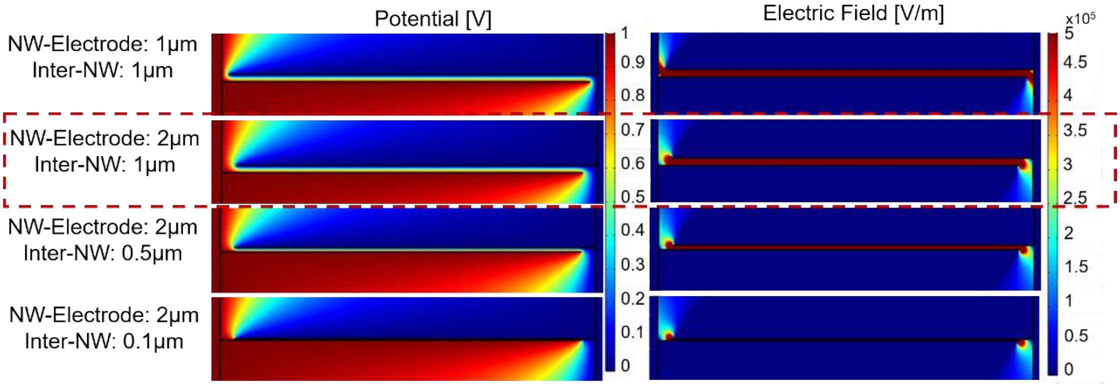

Figure 32: Evaluation of nanowire pitch and tip distance to the opposing microelectrode. Since no significant field enhancement could be observed by lowering the pitch down to 0.1 µm, the structure was fabricated with a nanowire pitch of 1 µm. At a lower distance of nanowire tip to the opposing electrode, the current becomes able to penetrate directly from the nanowire to the microelectrode. Thus, the distance was set to 2 µm to prevent punch-through leak current.

nanowire tip to the opposing microelectrode was set to 1 µm and 2 µm. With these combinations of various geometries, the electric field was simulated at a constant potential of 1 V. Regarding the pitch distance, the electric field already had its maximal strength at a distance of 1 µm. With decreasing pitch, the electric field stood constant (see Figure 32, right side) at the same magnitude. Thus, the optimal distance between interdigitating nanowire geometries was set to 1 µm, since smaller distances gave no additional features to the electric field and fabrication became simplified. Next, the electric field was observed for distances of 1 µm and 2 µm of tip to opposing electrode. Setting the distance to 1 µm, the electric field pinched through, resulting in field inhomogeneities at the edges of the capacitor structures and leakage currents directly to the microelectrode. In contrast, distances from 2 µm gave barely leaking of current directly to the microelectrode. In conclusion, capacitor nanowires geometries were fabricated with a 1 µm pitch between them and a distance to the opposing microelectrode of 2 µm to guarantee the largest and homogenous electric field between the microelectrodes.

5.3.3 Evaluation of the working potential

Next, simulations were performed to evaluate the most appropriate working potential between the electrodes during the sensing experiments. In previous simulations, the applied potential was only set to a constant value of 1 V. However, this potential did not reflect the best working potential in experimental work. In the following figure, a series of increasing potential and their resulting electric field between the nanowires can be seen. In this, the optimized nanowire geometry was applied (pitch: 1 µm, nanowire tip-to-electrode distance: 2 µm). During evaluation, the potential between the electrodes was increased stepwise from 0 V to 2 V with a step size of 0.2 V (see Figure 33, top panel). Starting from a potential of 0.2 V, the formation of an electric field could be observed with a magnitude up to around $4x10^5$ V/m. By minor increasing of the potential the electric field quickly reached its maximum magnitude at a potential of $5x10^5$ V/m starting at a potential of 0.4 V. However, further increase of the potential did not have any effect on the strength of the electric field (see Figure 33, bottom panel). Starting from a potential of 1.6V, strong electric field lines could be observed between the nanowire tips and its opposing microelectrode. Here, this effect has to be eliminated during sensing experiments, since it could alter the response of the sensor towards analytes. Thus, the evaluated distance to prevent leak current from nanowire to microelectrode was only feasible for potentials below 1.6 V. Further, these simulations were carried out in dry conditions, meaning that the punch-through effect from nanowire tip to microelectrode can be dramatically increased, if the sensor is in contact with any conductive liquid. In conclusion, the experimental working potential was set to 0.5 V to guarantee the maximum magnitude of the electric field between the nanowires and as little as possible leak current to the microelectrode.

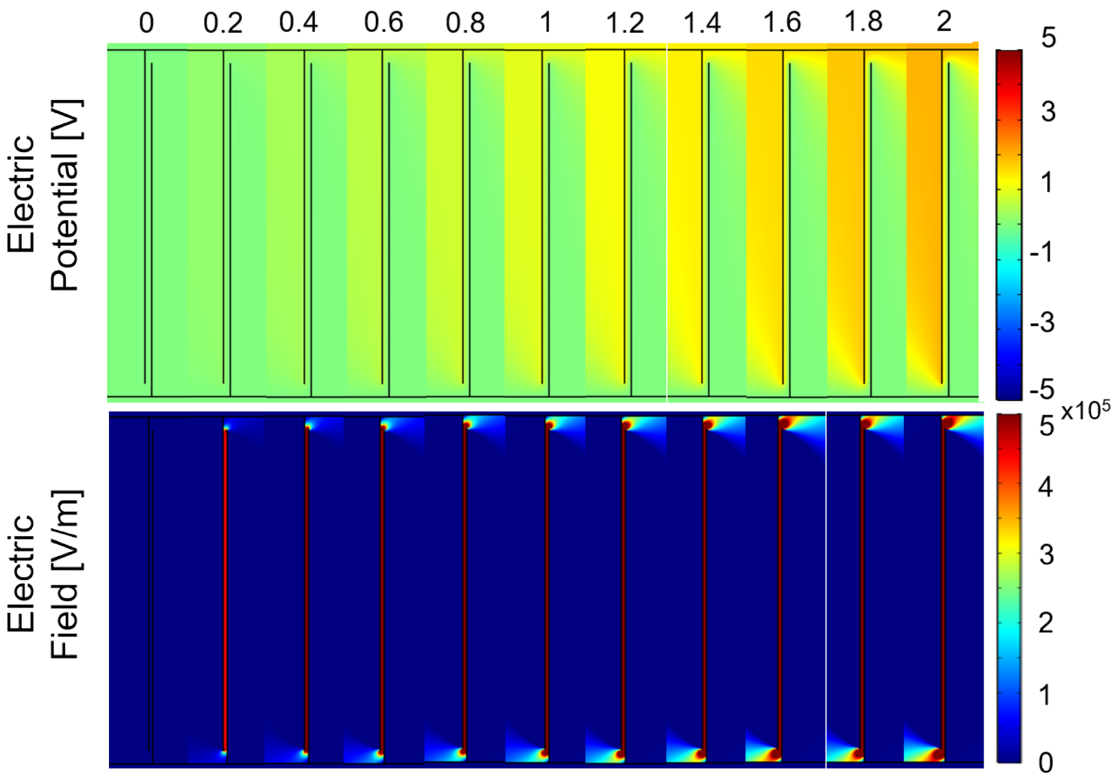

Figure 33: Evaluation of the working potential for experimental work. In the most appropriate sensing structure, the potential was slightly increased from 0 V to 2 V and the electric field was analyzed. Starting from a potential of 0.4 V, the electric field between the nanowires reached its maximum magnitude of 5 V/m. Further increase of the potential only caused a leak current between the nanowire and its opposing microelectrode.

5.3.4. Scaling of the sensing area

In all previous simulations, the focus was set on the electrical behavior of the structure containing only one pair of interdigitating nanowires. Thus, the effective detection area was rather low (46 µm²) which small area could result in a non-effective sensing at high noise. Hence, simulations were carried out to evaluate the electrical behavior, if the sensing area was increased by addition of several nanowire pairs, namely 6 pairs and 18 pairs (see Figure 34). The calculation of the detection the area between the nanowires was considered the following. For one pair, with an effective overlap of the nanowires of 46 µm, the area was calculated to be at A_{gap} = 46 µm² (46 µm in length and 1 µm in width). For multiple arrays of nanowire pairs, the area was calculated without the width of nanowires themselves having an area of A_{NW} = 4,8 µm² (0.1 µm in width and 48 µm in length). Therefore, the sensing area was found at 506 µm² for 6 pairs (11 gaps) and at 1610 µm² (35 gaps) for 18 pairs. During the simulation, the electric field distribution was evaluated for multiple interdigitating nanowires to get an insight into the electric field distribution for higher sensing areas at a constant potential of 1 V. Here, the electric field was homogeneous enlarged for larger nanowire arrays. Thus, also the up-scaling of single nanowire pair electrodes was successfully demonstrated without loss of electric field strength and homogeneity. In this, every nanowire pair represented an individual capacitor, connected in parallel (see Figure 34). In conclusion, up-scaling of the sensing area could result in a more stable signal and detection response, since the response signal when an analyte (with a smaller diameter than the sensing area) passes the sensing geometry, is equilibrated by unaffected capacitor structures. However, this equilibration results in a reduced sensitivity of the structure. A detailed analysis on this scaling effect will be discussed in *Chapter 5.7*.

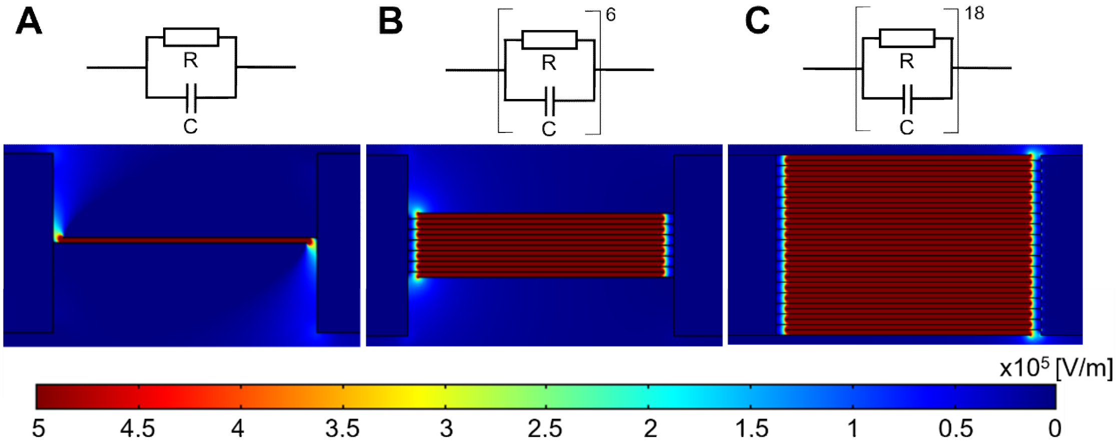

Figure 34: Electric field distribution for different sensing areas: **(A)** Single pair of interdigitating nanowires **(B)** 6 pairs and **(C)** 18 pairs. The electric field keeps its homogeneity while the strength of the electric stays constant when the number of nanowires is increased.

5.4 Fabrication of the nanoelectronic sensing structure

5.4.1 Nanofabrication and analysis

Both interdigitating nanowire structures and microelectrode pads for later integration into microcontact pads were patterned using electron beam lithography (see *Chapter 3.2.1*). The substrate consisted of a common glass-slide cut in half, thermally evaporated with a 5 nm thick Cr adhesive layer and a 50 nm thick Au layer. The substrate was additionally coated with a 70 nm thick PMMA 950k layer. Here, PMMA coating allowed selective manipulation of the surface by its sensitivity to electron beams and the nanoelectronic geometry could be directly written in the resist. For structuring, the negative mode of PMMA was applied and the steps can be seen on the following figure describing the fabrication of a sensor geometry with one interdigitating nanowire pair at different magnitudes, imaged by electron beam microscopy (see Figure 35). Firstly, the electron beam was guided in a specific pattern over the resist causing it to crosslink at the respective spots. Here, the dose was set to 7mC/cm² for electrode pads, while the dose for nanowire structures was increased to 27mC/cm². The reason for the application of higher doses for nanostructures can be explained by the proximity effect. As discussed in *Chapter 3.2.1*, if an electron beam hits the substrate, the electrons are able to penetrate both laterally and horizontally in the resist, thereby pre-exposing adjacent areas. Since the electron beam was guided over the substrate in scanning mode, this effect was greatly effecting the exposure in microstructures by pre-exposing neighboring areas, when it scanned over the pre-defined area. Subsequently, a smaller dose was needed to crosslink the resist. This effect was dramatically reduced in nanostructures, where the effective area, exposed by the electron beam, was greatly reduced. Thus, since the proximity effect was smaller, a higher dose was needed for an efficient hardening of the resist. The proximity effect on the nanowire width will be discussed in the following chapter. In Figure 35 panel A, a SEM image directly after exposure can be seen. The structure was written with respect to previous simulations, namely with a pitch of 1 µm, distance to the opposing microelectrodes of 2 µm, having 30 µm in length and 35 µm in width. In addition, the nanowire diameter was set to 50 nm in the design in order to compensate the proximity effect. By electron treatment of PMMA, both its structure and conductivity slightly changed and could be distinguished from unexposed parts. For a better visualization, the exposed parts were colored (blue). In this, the sensing designs could be efficiently transferred from the *in silico* design to the substrate. Subsequently, the unexposed resist was removed by soaking the substrate in acetone for 3 minutes. Following, the structure could be easily imaged using SEM by the strong differences in electrical conductance and electron density between gold and PMMA (see Figure 35, panel B). Depending on the applied dose for nanostructures, their width ranged from 75 nm to 250 nm. Now, the structured PMMA layer was used as an etching mask to transfer its structure to the gold layer. Finally, the unprotected gold layer was dry-etched in argon plasma followed by a final removal step of PMMA in oxygen plasma. Since PMMA shows high resistivity against dry-etching methods, the gold layer below crosslinked PMMA was well protected from the argon ions. Doing so, the PMMA structure could be efficiently transferred to the gold layer in a 1:1 fashion (see Figure 35, panel C).

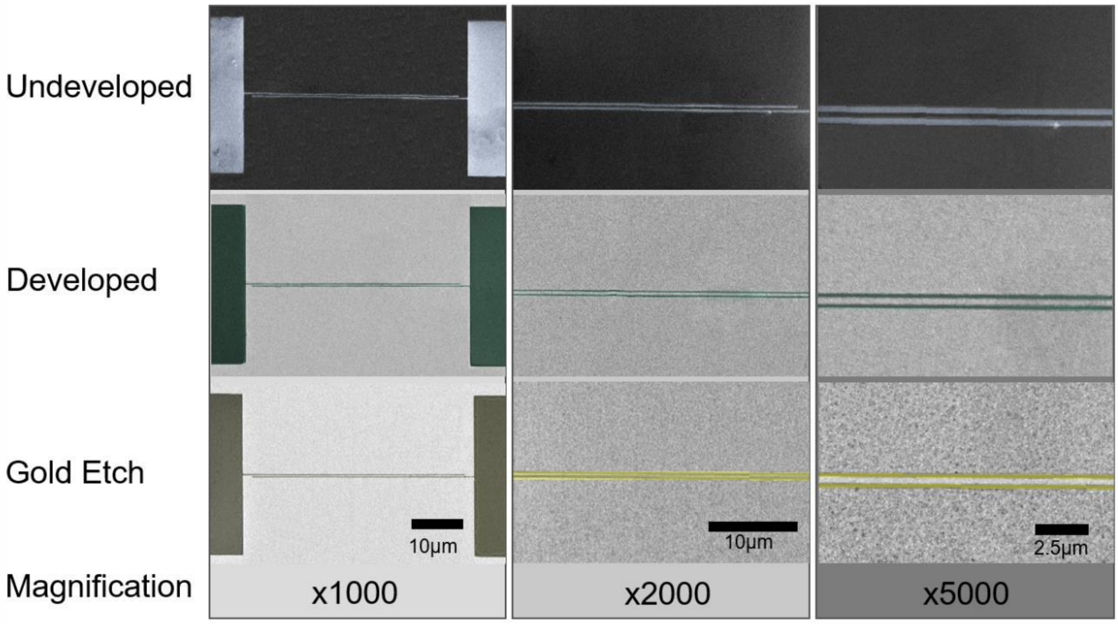

Figure 35: Fabrication of gold nanowire sensing geometries using EBL. **(A)** The electron beam at a high dose factor was guided in specific pattern on the PMMA layer, thereby crosslinking the PMMA chains. **(B)** Unexposed PMMA was removed in acetone, while exposed PMMA is resistant to this procedure. The sensor design could be efficiently transferred in the PMMA layer with a nanowire width of 75 nm to 250 nm. **(C)** Crosslinked PMMA layer was used as etching layer in argon plasma treatment. By removal of unprotected gold by argon ion etching (RIE), the layer below PMMA was protected allowing a 1:1 pattern transfer from the PMMA layer to the gold layer.

Further, the topography of the fabricated nanowires was evaluated to get an insight into the efficiency of the pattern transfer by dry etching strategy. For this, their profile was examined by both atomic force microscopy (AFM) as well as focused ion beaming (FIB) cutting. On Figure 36, the results for both techniques can be seen. In order to get information about the reproducibility of both EBL technique and pattern transfer, a sensor structure of 18 interdigitating nanowires was used for characterization (see Figure 36, panel A). During FIB cutting, the substrate was completely covered with 50 nm Ti for a correct cutting of the structure without any damage. In this, a large cut over the whole width of the nanowires was performed (see Figure 36, panel A, red dotted line) using an argon beam under ultra-high vacuum condition and imaged using a SEM setup (Neon 40, Carl Zeiss AG, Germany). On this chip, profile of the exposed parts of the nanowires revealed a near rectangle cross-section with a width of approximately 200 nm (see Figure 36, panel A, right side). So, the developed pattern transfer allowed homogeneous patterning of the nanowire array, as can be seen on the nearly identical appearance of the individual nanowires. Further, in order to examine the height of the wires, AFM (NanoWizard® 4, JPK Instruments AG, Germany) was used for measuring the profile (see Figure 36, panel B). Here, analysis revealed similar heights of the individual nanowires. Their heights were found to be between 50-60 nm which is slightly higher than the expected thickness when comparing with the evaporated layer thicknesses (Cr: 3 nm, Au: 50 nm). The reason for the variation in the thickness of nanowires was due to small changes

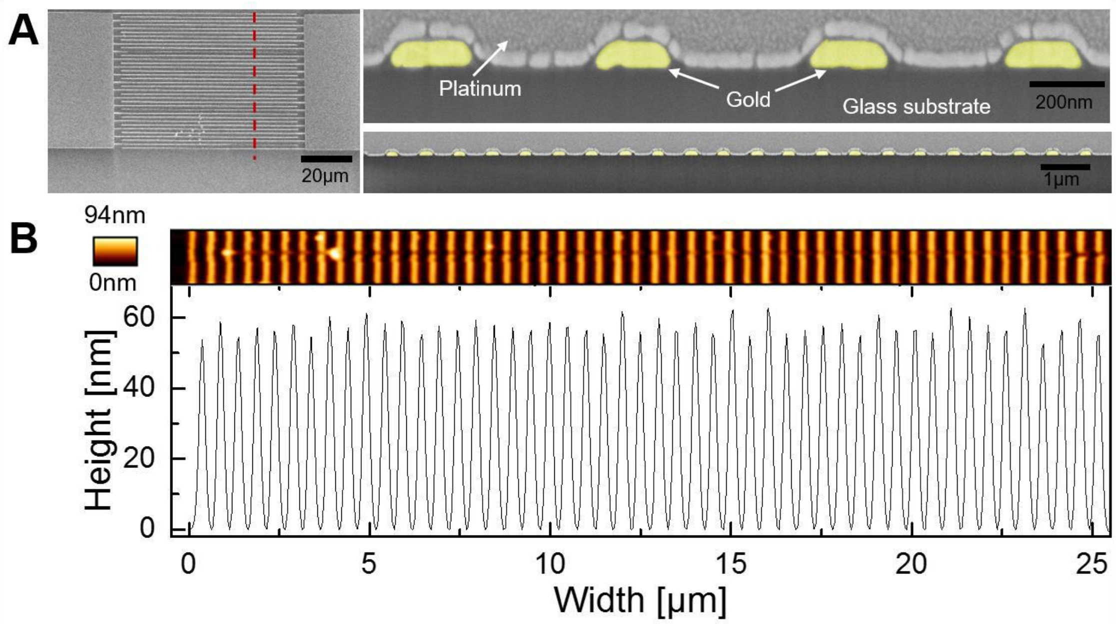

Figure 36: Profile examination of a fabricated nanowire array. **(A)** Focused Ion Beam (FIB) cutting technique allowed observation of profile appearance by ion-induced direct cutting of the device. Fabricated nanowires revealed nearly rectangular profile with a width of 200 nm. **(B)** Atomic force microscopy (AFM) was used to measure the height of the nanowires. Measurements revealed similar heights of the structures between 50-60 nm.

in deposited film thicknesses by the thermal evaporation of both metals. In conclusion, nanopatterning of the sensing structure was successfully demonstrated, showing nearly identical nanowire heights and widths without any defects and can be therefore used for prototyping of the sensing device.

5.4.2 Evaluation of the proximity effect

Due to unavoidable influences of the electron beam to adjacent areas from exposed structures, the resulting pattern in the resist was likely to be wider than in the original design. Here, the nanowire diameter was directly related to the dose of the electron beam. In detail, the dose was given by the settling time of the electron beam on one pixel, thereby defining the energy acting on one spot. Further, the optimal dose was additionally dependent on the effective feature size of the exposed area. The smaller it became, the higher the dose has to be set to guarantee sufficient energy to introduce molecular changes in the resist. On the other hand, the dose must not be too high since the proximity effect will increase the area, which was under the influence of electron irradiation. In the following, the optimal dose for nanowires with a design width of 50 nm was empirically evaluated and the result can be seen in the following figure. For microstructures, a dose of 7 mC/cm^2 was sufficient to chemically modify the area. In contrast,

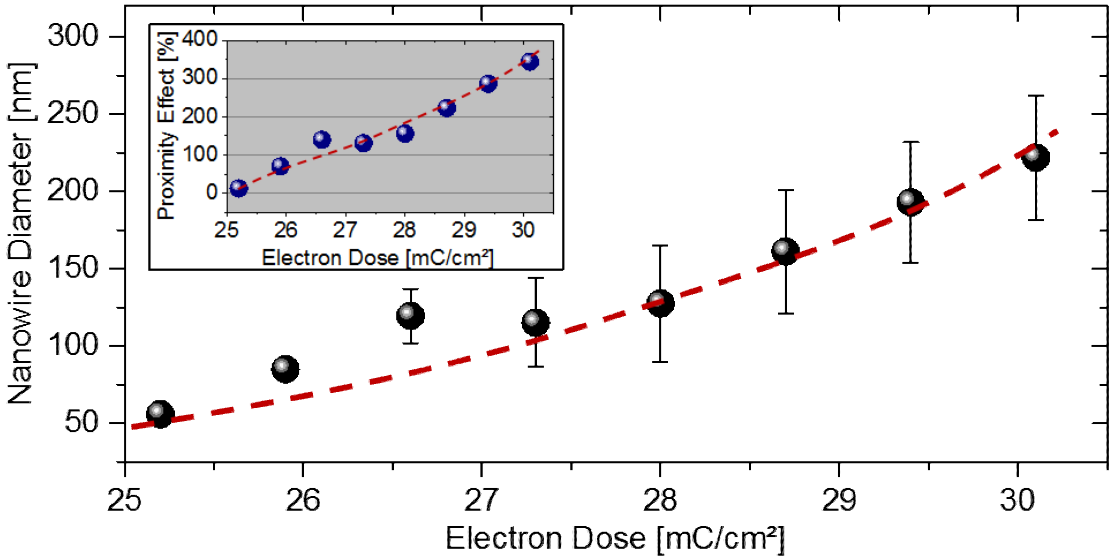

Figure 37: : Nanowire diameter depending on the electron dose. Due to unavoidable illumination of adjacent areas around the patterned regions, the patterns in the resist appeared wider compared to the design (see Inset). This effect, the “proximity effect” was directly related with the electron dose, or the electron beam settling time. At lower doses the nanowires had the same diameter or slightly higher diameter as in the design (design width: 50 nm) at a very low yield. The higher the dose was set, the bigger the nanowires and the yield became.

nanostructures were only visible starting from doses of 25 mC/cm^2. At this dose, nearly no proximity effect could be observed and the structures demonstrated a width with a maximum of 60 nm. However, the nanowire yield of correct PMMA pattering at this dose was very low and not reproducible. At higher electron doses up to 29 mC/cm^2, the yield increased stepwise while the proximity effect also raised to 100%-200%, (see Figure 37 Inset), resulting in nanowire widths from 100 nm – 200 nm. Furthermore, higher electron doses increased the nanowire widths beyond 200 nm. Thus, the electron dose was set between 27.5 and 29 mC/cm^2 resulting in nanowire patterning with a width of 100-200 nm at high yield.

5.5 Microcontacting of nanostructured sensing structures

In order to be able to electrically contact the nanostructures, common optical lithography technique was employed to connect the nanostructures with micron-sized electrodes. The overall design can be seen on the following figure. In total, six sensor structures could be contacted by independent electrode pairs, each one connected to a 1 mm² contact pad for micropositioner contacting (see Figure 38, panel A). The electrode pairs were designed in an opposing fashion having a width of 5 µm, separated by a gap of 90 µm. The overall distance from opposite pads was set to 22 mm, so that the design fitted on a conventional glass slide. Further, the distance between the nanowires was set to 1 mm. During EBL, the individual nanosensing structures were patterned on the glass substrate in the middle (at 12 mm from the edge) at a horizontal position starting from 10 mm from the edge with a distance of 1mm. Thus, this designed geometry allowed precise contacting of the contact pads, defined by EBL. In detail, the nanowire-contacting pads were carefully integrated into micron-sized electrodes connected to electrode pads (see Figure 38, panel B) using optical lithography with the resist AZ5214e in negative fashion (see *Chapter 3.2.3.1*). After development, 3 nm Cr and 50 nm Au were thermally evaporated on the substrate and the electrodes were defined by a lift-off process by resist removal in acetone (see *Chapter 3.3*) (see Figure 38, panel B and C). After an annealing process at 200°C for 2 hours, the electrode pads were covered with a drop of silver conduction solution to minimize the contact resistance between the tungsten tip of the micropositioner and the electrode pad. Doing so, the fabrication of the sensing platform was finished and the ready-to-use chip could be further utilized for microfluidic integration or characterization measurements.

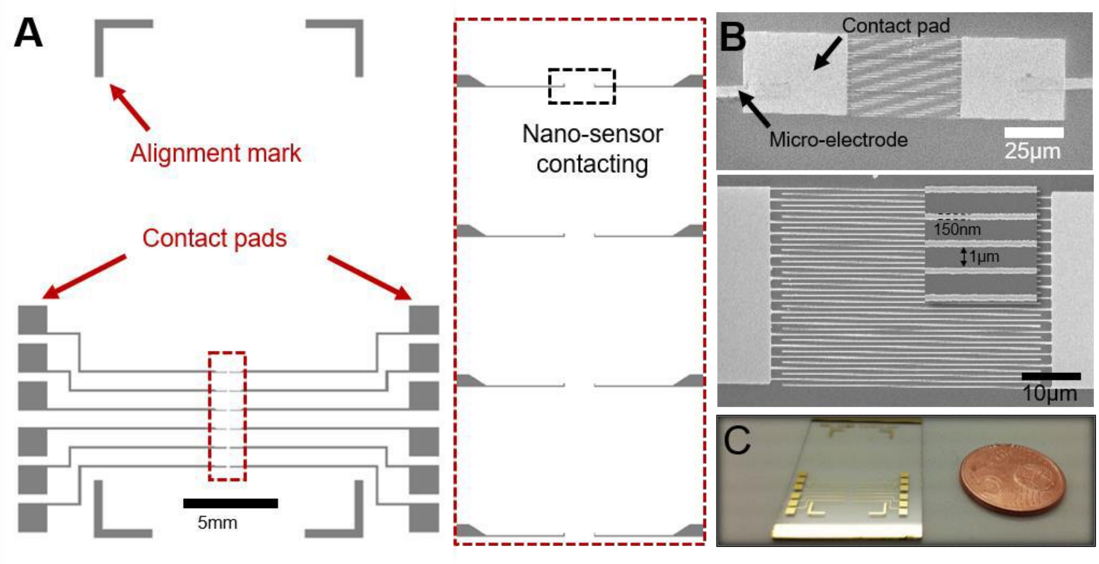

Figure 38: Microcontacting of the nanostructures, defined by electron beam lithography. **(A)** *In silico* design of the microelectrodes using the software WiWebs' CleWin. Six individual nanostructures could be contacted by opposing electrode pairs which geometry was aligned to be integratable on a common microscope slide. **(B)** Using the contact pads, defined by EBL, allows contacting of the nanowires by optical lithography methodology, including thermal deposition of 3 nm Cr and 50 nm Au and following lift-off strategy **(C)** Real-life appearance of the sensor platform.

5.6 Electrical characterization of the sensing structure

Prior to sensing experiments, the sensor's electric response was evaluated in both direct current (DC) and alternating current (AC). Based on the structure appearance, a capacitive response of the system was expected with the gold nanowire acting as the capacitor plates. Here, the substrate, namely boro-silicate glass, acted as the dielectric layer between the nanowire electrodes in dry condition. As soon as the condition were set to a liquid environment, the liquid covering the electrodes started to play the role of the dielectric layer, if the electrical conductivity was higher than the conductivity of the substrate. Since the response of the capacitor was dependent on the electric properties of the dielectric layer, two liquids with differences in their ionic concentration and their conductance were tested to evaluate the sensor's working behavior in liquid environment, namely 1x PBS and deionized water.

5.6.1 Characterization in alternating current (AC)

Applying the electrical impedance spectroscopy (EIS) principle allowed determination of the structure's response in alternating current in a wide range of frequencies. Here, the response was evaluated for frequencies ranging from 50 Hz to 20 MHz at a constant reference amplitude of 0.5 V. For electric characterization, 2 parameters were recorded: the sensor's response amplitude *V_{out}* and its phase shift *$Phase_{deg}$* from the reference frequency. With the help of these 2 signals, the complex *Impedance* of the device could be calculated. Here, the real part of the impedance, the amplitude, was calculated using the following formula:

$$Z' = \frac{V_{in}}{V_{out}\sqrt{\left(\omega C_{ref}\right)^2 + \left(\frac{1}{R_{ref}}\right)^2}} \tag{7}$$

With V_{in} = 0.5V as the input voltage, V_{out} the measured output voltage, ω the angular frequency, calculated by 2π*f*, C_{ref} = 10pF as the inner capacitance of the measurement device and R_{ref} = 1 MΩ as the inner resistance of the device. Following, the imaginary part of the impedance was calculated. For this, the phase signal $Phase_{deg}$ was initially transformed in radiant units applying the formula:

$$Phase_{rad} = -\frac{Phase_{deg}\,\pi}{180} \tag{8}$$

Now, the imaginary phase signal could be calculated with the transformed phase from formula (8):

$$Z'' = Phase_{rad} + tan^{-1}\left(\omega C_{ref} R_{ref}\right) \tag{9}$$

Finally, the polar form of the complex Impedance Z was calculated with the application of the following formula, introducing both formulae (7) and (9):

$$Z = Z' e^{-jZ''} \tag{10}$$

At first, the sensor's response to different ionic liquids was evaluated, namely deionized water with a low concentration of ions and 1x PBS buffer as high molarity liquid. In the following figure, the representation of the impedance in the Nyquist diagram can be seen, where the x-axis represents the real part of the impedance *ReZ* while the y-axis shows the negative imaginary part *-ImZ*. This graphical representation of the impedance allowed both determination of the equivalent circuit by characteristic shapes of distinct electrical building blocks and representative values for resistances and capacitances. Initially, the sensor's response in AC domain was analyzed in dry (see Figure 39, panel A). Here, the boro-silicate substrate acts as dielectric layer of the capacitor. Due to its low

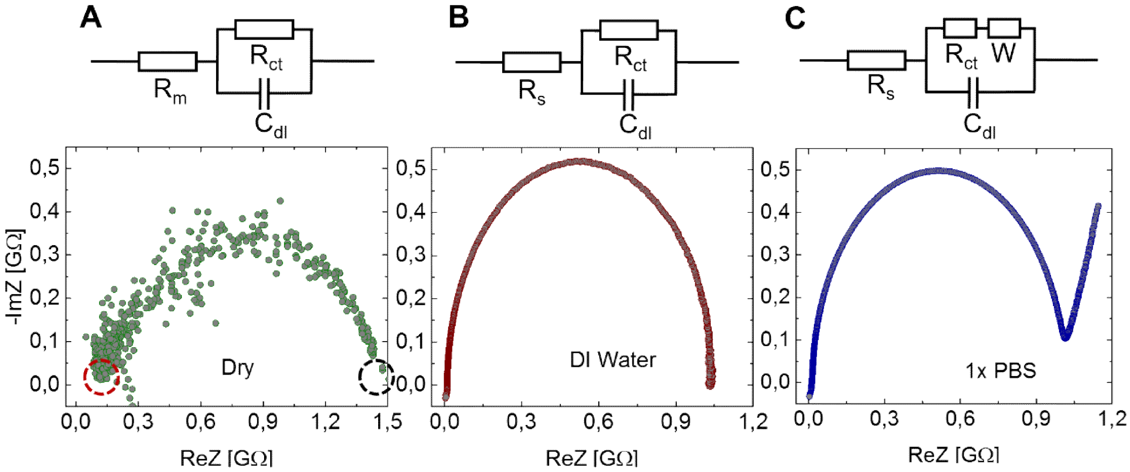

Figure 39: Nyquist diagram of the sensor element in dependence of its environment. **(A)** Dry conditions: The signal showed a strong noise caused by the low electric conductivity of the substrate. The negative semicircle of the diagram represents a RC circuit. **(B)** Deionized water droplet on the sensor: The signal was stabilized over the full frequency spectrum. The equivalent circuit shows a Randles cell. (**C**) High ionic liquid on the sensor caused linear increase of the impedance in the low frequency regime and shows the behavior of a diffusion-controlled Randles cell.

electric conductivity, the sensor response demonstrated a high-noise signal, especially in the high frequency region (left side of the plot). The shape of the Nyquist plot showed a negative semicircle, thus demonstrating a RC element in the equivalent circuit with an approximate resistance of the substrate $R_m = 100$ MΩ, indicated by the lower intersection point of the plot with the x-axis (See Figure 39, panel A, red circle). Additionally, the charge-transfer resistance could be found at R_{ct} = 1.4 GΩ, indicated by the higher intersection of the plot with the x-axis (See Figure 39, panel A, black circle). Next, a drop of deionized water was carefully placed on top of the sensing structure and the signal was recorded. Here, the presence of even small amounts of ions stabilized the signal significantly in the full range of measured frequencies resulting in the formation of the defined semi-circle in the Nyquist diagram, resembling an optimal appearance of a simplified *Randles cell* circuit with a solution resistance R_s of 10.66 MΩ and R_{ct} = 1.03 GΩ (see Figure 39, panel B). Further, deionized water was exchanged with PBS buffer with a high molar concentration of 10 mM (1x). In the Nyquist diagram, the effect of the strong ionic environment can be seen in the low frequency region (right side). Here, the linear increase of the impedance is related to the diffusion of the ions in solution and is represented in the equivalent circuit as the *Warburg* element *W* (see Figure 39, panel C). Consequently, the sensor signal in alternating current was behaving as expected; it was a capacitive electric building block where its covering liquid environment is changing its output behavior. Depending on the liquid on the sensor (high or low amount of dissolved ions) the equivalent circuit of the sensor described a RC-circuit, a Randles cell or – for high amounts of surrounding ions – a diffusion controlled Randles cell.

5.6.2 Characterization in direct current (DC)

The sensor's electric response was additionally evaluated in direct current using the electric voltammetry techniques. Here, the voltage between the electrode was swept from -1 V to +1 V and back with a step size of 0.05 V at a time constant of 100 ms, while the current was tracked. Based on the appearance in the IV plot, the electrical performance of the sensor can be evaluated. In dry conditions, the sensor demonstrated only very small currents with a maximum of 1 nA. This effect was due to the small conductivity of the dielectric layer, *i.e.* boron silicate. Nevertheless, the transformation of current values to absolute numbers revealed the characteristic "butterfly" appearance of a capacitive structure. Here, the difference of measured current based on the direction of the voltage sweeps showed the charging effect within the capacitor (see Figure 40, panel A). During the first loop of voltage increase (-1 V to +1 V) the capacitor was charged and in the second loop, it was discharging. Thus, the area between the curves could be interpreted as the electrochemical activity of the capacitor, or its efficiency. For dry condition, the area between the curves was rather low developed, but this effect was enhanced as soon as the experiment was repeated in liquid environment. In deionized water, the overall current was increased by a factor of 10, while the current difference between the sweeps was increasing (see

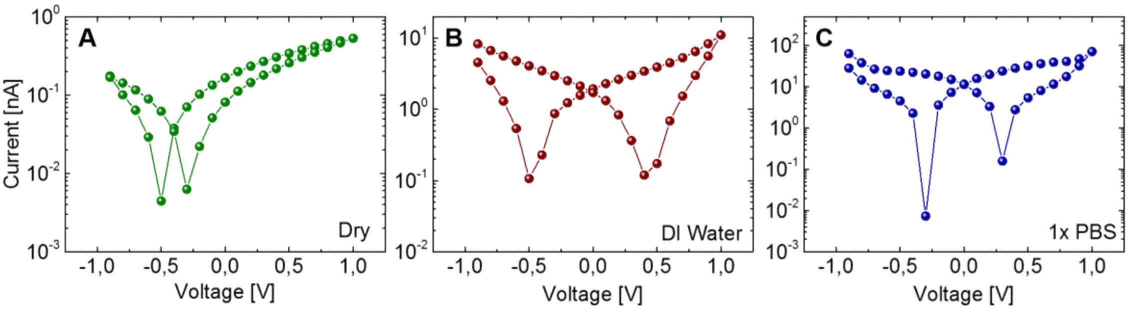

Figure 40: Cyclic voltammetry (CV) of the nanosensing structure in the range of -0.5V to +0.5V in DC mode. **(A)** In dry condition, the CV diagram showed a butterfly shape, characteristic for capacitive structures with maximum current levels of 1nA. **(B)** Measurement in liquid condition (deionized water). The capacitance and the maximum current level was vastly increased, while preserving the capacitive behavior by opening of the differences between forward and backward sweep. **(C)** Exchange of water to highly ionic environment (PBS, 10mM). Compared to dry conditions, the current level was increased by a factor of 100, majorly increasing the capacitance of the device.

Figure 40, panel B). Therefore, the capacitance and thus the energy storage was increased by the change of the dielectric medium to deionized water[215]. Since the maximum measured current of the capacitive structure was located at a very low level (10 nA), the liquid was exchanged with a highly molar solution, *i.e.* 1x PBS. As expected, the energy storage was increased by a factor of 100, compared to dry conditions (see Figure 40, panel C). Following, in order to use the developed nanostructure as sensing geometry, it had to be used in ionic environments to guarantee a sufficient current level and capacitance or energy storage level.

5.7 Scaling effect of nanostructures in static sensing conditions

In order to demonstrate the effect of nanostructures on the sensitivity the device towards foreign micron-sized objects in influence of the device' electric field, a SiO_2 particle with a diameter of 10 µm was carefully placed between the electrodes in 0.1x PBS. Here, PBS solution was dissolved by a factor of 10, since application of 1x PBS as solution screened the contribution of the particle and no difference to reference measurements could be observed. By placement of a particle, the equivalent circuit changed, since the particle introduced its own resistance and capacitance, which was now influencing the output characteristics of the device. The used model was developed in the late 80s and is widely used for interpretation of single-cell impedance measurements[39,104,216] (see *Chapter 2.3.2*). If no particle was present on the sensor, the circuit represented a common Randles cell circuit, where the resistance and capacitance were connected in parallel. As soon as a particle was influencing the sensor, a new element was added to the circuit, namely the resistance and capacitance of the particle in series, parallel to the inner RC circuit of the device (see *Chapter 2.3.2*, Figure 3). Next, the sensitivity was firstly evaluated in static mode using EIS technique in order to see the particle's effect over a big range of frequencies. In this, the output of three different structures was evaluated: (1) only microelectrode structure without nanowires, (2) 18 pairs of interdigitating nanowires, (3) one single pair of nanowires. In order to quantify the sensitivity of the device, the Nyquist curves of the respective structure with and without particle were compared. The frequency sweep was carried out from frequencies from 200 Hz to 20 MHz and the difference of the curves was acquired by the integral difference of the two signals. Here, only the region without the low frequency diffusion domain were taken into consideration, meaning only the signal from medium resistance (R_m) to the kink before the diffusion-influenced domain, at the end of the charge-transfer regime (R_{ct}). In the first case, when there were no nanowires present in the sensing geometry, the particle between the microelectrodes had nearly no influence on the output signal. The EIS in the presence of a microparticle merely deformed the output response (see Figure 41, panel A). In this, the Nyquist curve was negatively deformed in y-direction (see Inset) and shifted to the left. A more detailed analysis of the magnitudes of the lateral deformations will be discussed in the following chapter. The absolute integral difference of the curves was calculated to be at only 0.26% with an input voltage of 0.5V. In contrast, the signal difference in presence of nanowires is greatly enhanced by a factor of around ~20 (see Figure 41, panel B). In this, the signal deformation difference between the presence and absence of a particle was more pronounced leading to a signal difference of 4.22%. The biggest deformation of the output curve in the presence of a particle was observed for a single pair of interdigitating nanowires. Here, the signal difference was calculated to be at 5.68% (see Figure 41, panel C). In conclusion, presence of nanowires greatly improved the sensitivity towards micro-objects in the influence area of their electric field. Here, the strength and the homogeneity of the electric field played a major role. While the electric field between microelectrodes was weak and inhomogeneous, the field in the

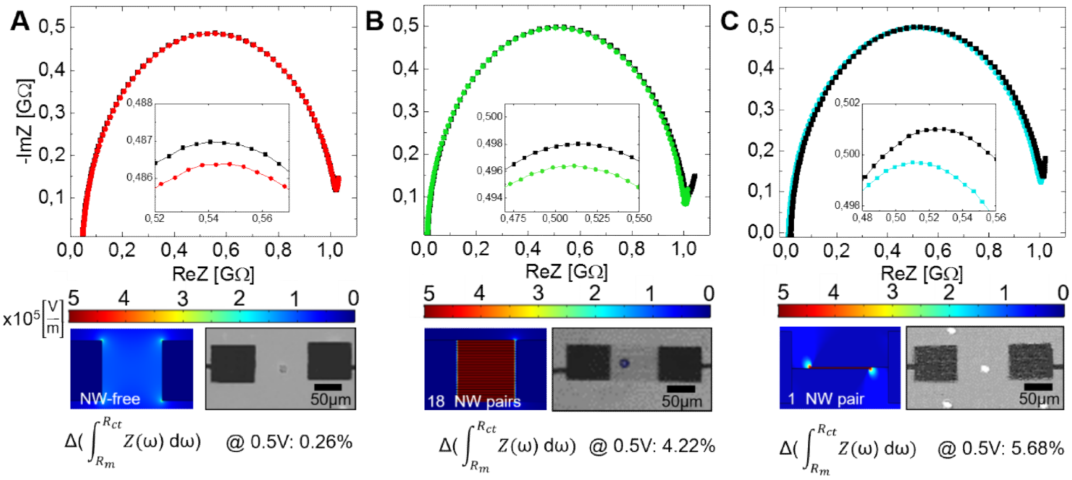

$\Delta(\int_{R_m}^{R_{ct}} Z(\omega)\,d\omega)$ @ 0.5V: 0.26%

$\Delta(\int_{R_m}^{R_{ct}} Z(\omega)\,d\omega)$ @ 0.5V: 4.22%

$\Delta(\int_{R_m}^{R_{ct}} Z(\omega)\,d\omega)$ @ 0.5V: 5.68%

Figure 41: Scaling effect of using nanostructures on the sensing sensitivity. **(A)** EIS with and w/o particle on the sensing area between solely microelectrodes. The difference of the curves in the Nyquist diagram was at 0.26%. **(B)** Comparison of the Nyquist diagrams with a sensor including 18 nanowire pairs. The difference was greatly enhanced, located at 4.22%. **(C)** Change from 18 nanowire pairs to only one pair. The difference of the Nyquist curve with particle and without particle was further increased to 5.68%.

presence of nanowires was greatly amplified to a strength of up to 5×10^5 V/m (see Figure 34, panel A-C). Further, reduction of the sensing area also improves the sensitivity of the device. In the case of 18 interdigitating nanowire pairs, every nanowire pair represented one capacitor. In this case, the sensing structure represented 18 individual capacitors, which were connected in parallel. Further, the particle was only able to cover a fraction of them and its resulting signal change was partly compensated by the other uncovered fraction of capacitors. For one single nanowire pair, the effect of the particle was more pronounced, since there were no other compensating capacitors present in the structure. However, in dynamic sensing experiments, only one capacitor might be very prone to differences of the position of the particle or electric noise in general, while bigger sensing areas might compensate the noise. A detailed analysis on the signal to noise ratio and the sensitivity in dependence of the number of interdigitating nanowires in dynamic measurement mode will be evaluated in *Chapter 5.11.3.*

5.8 Multi-analyte detection on the sensor

Additionally, the effect of several micro-objects on the sensing area was evaluated. For this, one to three particles in 0.1x PBS solution were carefully placed between the electrodes of a sensor structure with 18 interdigitating nanowire pairs and EIS was performed from 200 Hz to 20 MHz. Based on the difference of the reference Nyquist curve to the curves in the presence of a single or multiple particles, the effect of the analytes could be analyzed, as well as the extraction of the electrical parameters of the particles, namely electrical resistance and capacitance, became possible. On the following figure, the high frequency regime of the Nyquist curves for the device without (black), one (cyan), two (red) and three (yellow) particles can be seen (see Figure 42). Here, a clear trend could be observed: the more particles were present on the sensor, the more the Nyquist curve was shifted to the left. In Nyquist curves, the intersection with the x-axis indicated the resistance of the medium R_m, which was located at 12.68 MΩ for the absence of particles on the sensing area. The intersections of plots for the particles indicated the combination of the resistance of the medium R_m and the resistance of the particle(s). The value for this equivalent resistance R_{eq} was extracted from the plots and was located at 11.03 MΩ for 1 particle, 8.96 MΩ for 2 particles and 7.13 MΩ for 3 particles (see Figure 42, panel B). Based on the equivalent circuit model of single-shelled particles[39,217], the resistance of one particle R_p^1 could be calculated. Since R_m and R_p are connected in parallel, the resistance of the particle was calculated using:

$$\frac{1}{R_{eq}} = \frac{1}{R_m} + \frac{1}{R_p^1} \tag{11}$$

Thus:

$$R_p^1 = \frac{1}{\frac{1}{R_{eq}} - \frac{1}{R_m}} \tag{12}$$

Doing so, the resistance was calculated to be at 84.76 MΩ for a single particle. In the case of several particles, the individual particle capacitances and resistances (R_p^1 to R_p^3 and C_p^1 to C_p^3) were connected in parallel to the equivalent circuit (see Figure 42, panel A) since R_{eq} is shrinking with increasing numbers of particles. Thus, the magnitude of the resistance of individual particles are divided, resulting in resistances of 47.74 MΩ and 34.91 MΩ for two and three particles, respectively.

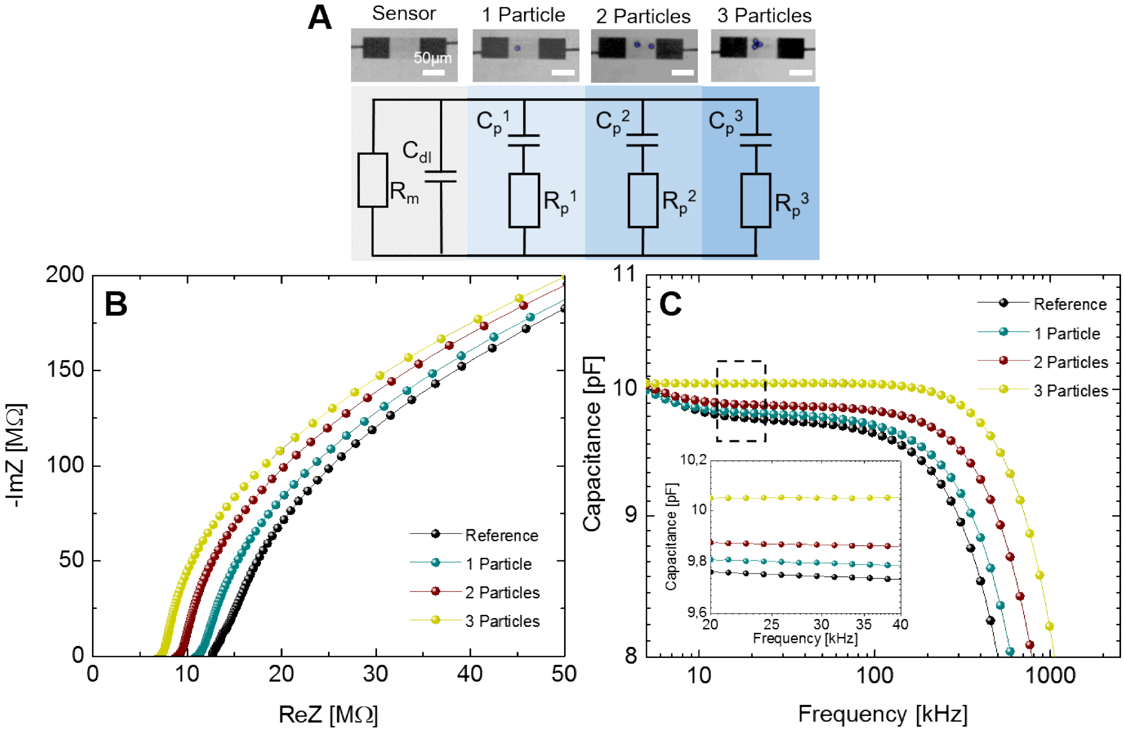

Figure 42: EIS output response of a sensing structure with 18 interdigitating nanowire pairs in absence and presence of 10 µm SiO_2 particle(s) **(A)** Equivalent circuit model in presence of multiple particles. **(B)** Close-up of high frequency region of the Nyquist plots for no particle and one, two and three particles on the sensor. The intersection of the plot and the x-axis defined the equivalent resistance R_{eq}. **(C)** Double logarithmic plot of the capacitance, calculated from the Nyquist plots. The forming plateau signal defined the equivalent capacitance C_{eq} of the system.

For this, formula (5) was extended with the resistance values for previous number of particles, in detail:

$$R_p^2 = \frac{1}{\frac{1}{R_{eq}} - \frac{1}{R_m} - \frac{1}{R_p^1}} \tag{13}$$

and

$$R_p^3 = \frac{1}{\frac{1}{R_{eq}} - \frac{1}{R_m} - \frac{1}{R_p^1} - \frac{1}{R_p^2}} \tag{14}$$

Here, the differences in their resistance values can be explained by the polydispersity of the particles themselves, their position on the nanostructures and how many capacitors are influenced, as well as if there are in contact with each other. Furthermore, the capacitance of the particle could also be determined by the analysis of the Nyquist curves. For this, the imaginary part of the complex impedance was divided by the angular frequency, resulting in an approximation of the capacitance values:

$$C = \left|\frac{Z''}{j\omega}\right| \tag{15}$$

On Figure 42, panel C, the calculated capacitance in dependence of the frequency can be seen. Plotting in a double logarithmic scale revealed the formation of a plateau between 10 kHz and 200 kHz, showing the capacitance of the electrical system. Here, the presence of particle(s) showed a clear influence of the device. With the help of the equivalent circuit model used previously, the capacitance of the particles C_p was calculated by using measured C_{eq} from the plateau values, subtracted by the capacitance of the medium C_m from the plateau value of the sensor without particles. Taking into account the connection of the capacitor in parallel fashion (or one particle), C_{eq} is defined by:

$$C_{eq} = C_m + C_p^1 \tag{16}$$

And thus:

$$C_p^1 = C_{eq} - C_m \tag{17}$$

And following for 2 and 3 particles:

$$C_p^2 = C_{eq} - C_m - C_p^1 \tag{18}$$

$$C_p^3 = C_{eq} - C_m - C_p^1 - C_p^2 \tag{19}$$

Here, the capacitance of one particle was found to be at $C_p^1 = 52.99\,fF$, while for the capacitances for 2 and 3 particles were calculated to be at $C_p^2 = 69.00\,fF$ and $C_p^3 = 185.00\,fF$, respectively. In conclusion, the sensor was able to detect micro-objects from single to multiple numbers, where the signal change was directly related to the number of analytes on its surface.

5.9 Microfluidic focusing system

Now, after characterization of the sensor device in frequency sweeping mode as well as investigation of the scaling effect in presence of nanoscopic structures, the system's measurement strategy was altered to dynamic mode allowing high-throughput measurements at a fixed frequency. For this, an adequate geometry for sample delivery had to be evaluated allowing high-throughput and clogging-free focusing of analytes in liquid. Further, in order to characterize sample delivery and reduced costs and efforts, a PDMS-based microfluidic flow cell was chosen. Here, the chosen material, PDMS, allowed fast prototyping of adequate geometries in reasonable times and allows flow characterization of fluorescent liquids due to its low auto-fluorescence. For fabrication, the standard soft lithography methodology was used (see *Chapter 3.2.4*). For sample delivery, a 2D hydrodynamic focusing structure was chosen, where the sample liquid was focused by three parallel flows, confining it to a vastly decreased cross-section prior to focusing. This strategy offered a great variety of advantages compared to solely reduced channel sizes. Firstly, channel fabrication became simplified, since the channel geometry had not to be confined to the sensing area. Here, the analyte stream width was tuned by the flow of the focusing liquid, meaning the channel width was not dependent on the sensing width, thus making the integration simpler. Second, micro-objects in laminar flow follow specific positions in the stream, introduced by inertial lift forces[218,219], improving the device's output response. Furthermore, contact of micro-objects in the focused stream with channel side walls is inhibited by the neighboring focusing streams. Thus, the chance of channel clogging is greatly reduced compared to single flow of analyte solution, especially if focusing strategies are applied by special geometries, *e.g.* ratchets, short channel width reductions and microchannel curve-assisted particle focusing[220,221]. Therefore, a 2D hydrodynamic focusing geometry was manufactured with a channel width of 200 µm. Here, the individual channel parts were arranged in way that the sample liquid was focused at the bottom and in the middle of the main channel, which was aligned over the sensing structure. In order to focus, the analyte stream was firstly focused horizontally by a perpendicular focusing stream from the top (see Figure 44, panel A). Further, the analyte stream was focused vertically by two focusing streams coming channels in a 45° angle top (see Figure 43, panel A). In the following paragraphs, the geometry's capability to focus laterally and vertically will be presented.

5.9.1 1D focusing using FITC-probed deionized water

Firstly, the efficiency of the designed channel system was evaluated in the lateral dimension. For this, a stream containing 1:100 diluted FITC solution was focused using a divided stream of 1M KCl solution. In this confined geometry at low Reynolds numbers, 2 miscible stream flowed next to each other, where mixing only took place at the interface by diffusion. At the crossing of the FITC solution channel and the KCl liquid channels in a 45° angle (see Figure 43, panel A), the FITC solution was confined by the two focusing streams in the middle of the channel. Here, the width of the FITC solution could be tuned by changing the flow

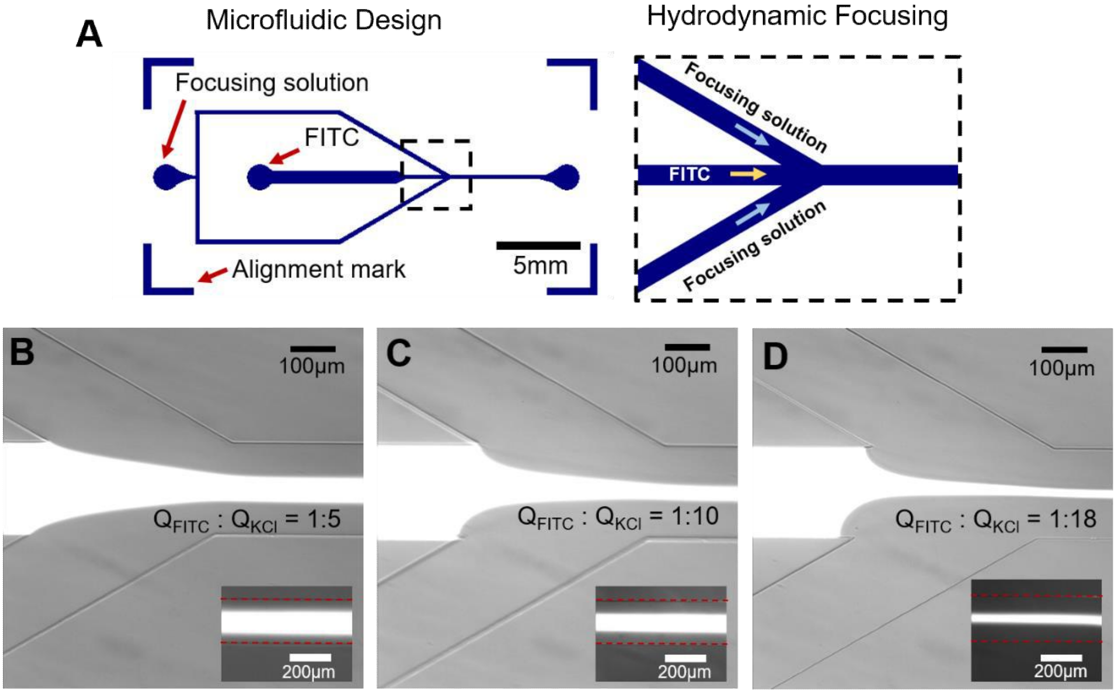

Figure 43: 2D microfluidic hydrodynamic focusing geometry characterization. **(A)** *In silico* design of the channel geometry. The FITC containing solution was focused by two KCl focusing solutions at the crossing geometry. **(B)** Fluorescent microscope image of the focusing structure. At a flow ratio of 1:5, FITC solution was focused to a width of 70 µm. Further increase of the ratio to 1:10 **(C)** and 1:18 **(D)** decreased the width to 40 µm and 20 µm, respectively.

rate ratio between the two streams. At a flow rate of 5 µl/min for KCl and 1 µl/min for FITC, the focusing streams reduced its width from 200 µm to approximately 70 µm (see Figure 43, panel B). The focused stream was stable for the complete range of the subsequent main channel, where only diffusion of FITC at the surface to the focusing streams took place (see Figure 41, panel B Inset). The effective stream width by focusing could be further reduced by increasing flow rates of the KCl stream. Changing the ratio of the flow rates $Q_{FITC} : Q_{KCl}$ to 1:10 and 1:18 reduces the FITC solution width to 40 µm and 20 µm, respectively (see Figure 43, panel C and D). In conclusion, the efficiency of the 1D focusing system could be successfully proven, since this geometry offers precise control over the efficient sample liquid in the main channel in the correct range.

5.9.2 2D Focusing using fluorescent microparticles

Subsequently, the 2D focusing capability of the device was tested using fluorescent 1.08 µm polystyrene particles in deionized water, probed with 0.1% Tween in order to reduce particle adhesion to the channel walls and particle aggregation. Here, after injection of the particle solution a novel inlet for focusing was introduced, which allowed focusing in the horizontal dimension (see Figure 44, black dashed box). This perpendicular stream of focusing liquid pushed the analyte stream at the bottom of the channel which was later focused in the middle of the channel as it was done with FITC solution in the previous experiment (see Figure 43, panel A and B). Using two independent focusing streams for lateral and horizontal focusing allowed precise control on the focusing area of the analyte stream and therefore the position of the particles in the channel after the focusing geometries. Figure 44, panel C-E, shows an example of particle focusing where the flow rates of the two focusing streams were applied in a way that the particle solution was focused in a small area in the middle of the channel with a width of around 40 µm and a height of maximum 2.9 µm. In this, the lateral position of the particle could be easily determined by microscopic records of the channel after focusing. In contrast, the horizontal position of the particles had to be calculated using the formula for height analysis of microparticles in microfluidics, established by Winer and co-workers[222]. In this, the measured particle size in the records is directly correlated with its height in the microchannel, when the focus is set on the channel bottom.

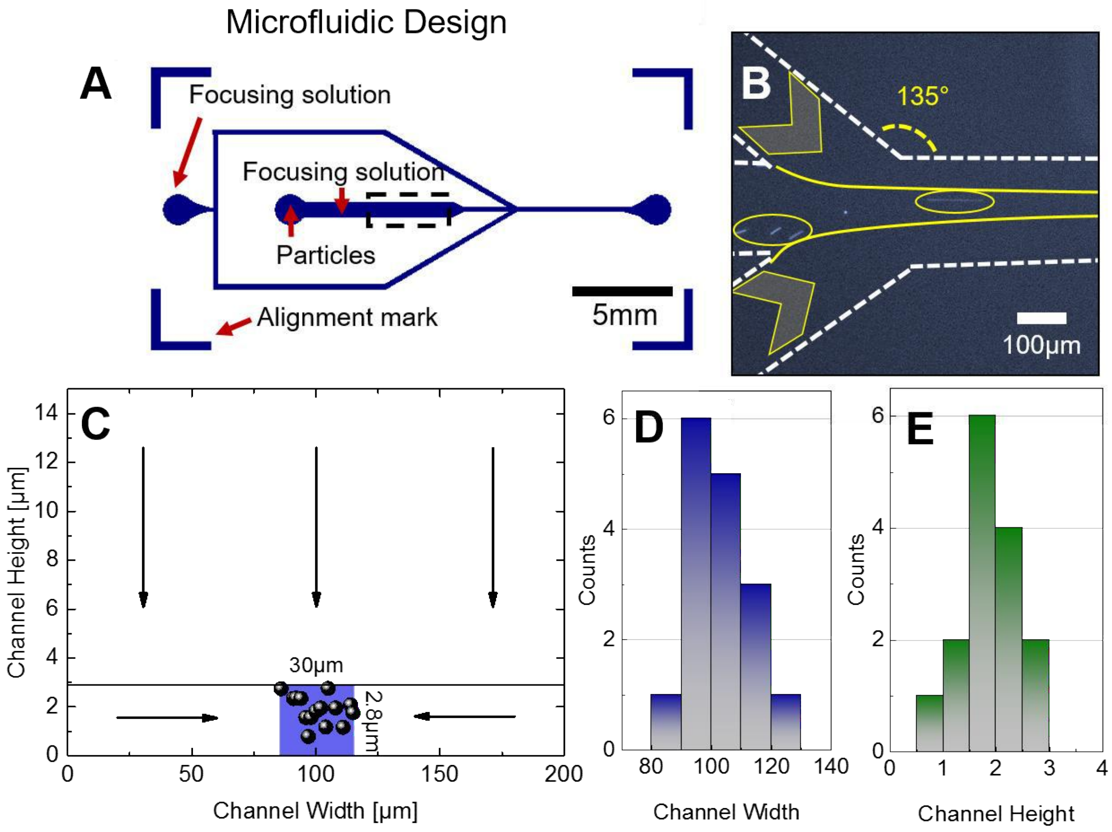

Figure 44: 2D focusing of fluorescent microbeads: **(A)** *In silico* design of the microfluidic setup **(B)** Fluorescent image of particle focusing **(C)** Position of the particle in the main channel with a height of 15 µm and a width of 200 µm. The beads could be efficiently focused in a small window of 30 µm width and 2.9 µm height **(D)** Width counting of the particles **(E)** Representation of the corresponding particle heights using the formula from Winer and co-workers[222].

Here, the formula was derived for the following parameters: particle size of 1.08 µm at a magnification of 10x and a numerical aperture of 0.25, illuminated by a fluorescent light source at a wavelength of 503 nm:

$$z[m] = \left(d_p[m] - \frac{1{,}23 \text{ x } 10^{-11}[m]}{170}\right)^{\frac{1}{2}} \tag{18}$$

where z is the distance of the particle with measure diameter d_p from the surface.

5.10 Microfluidic integration of the two technologies

If both these technologies, the 2D hydrodynamic focusing and the nanosized impedance sensor, are brought together, this conjunction opens a new route towards nanosensing in the impedance cytometry regime, where the analyte is delivered to the sensor via microfluidic geometries. Here, the two technologies were combined by careful alignment of the main channel structure on the nanosensors so that the sensing structure is located in the middle of the channel (see Figure 45, panel A and B). The integration was carried out by treatment of both substrates in oxygen plasma at 40W for 5 seconds, followed by immediate alignment under the microscope. In order to strengthen the covalent bonding, the chip was kept at 70°C on the hotplate overnight. Doing so, the focused flow of analytes could be directly focused towards the sensing structure (see Figure 45, panel C).

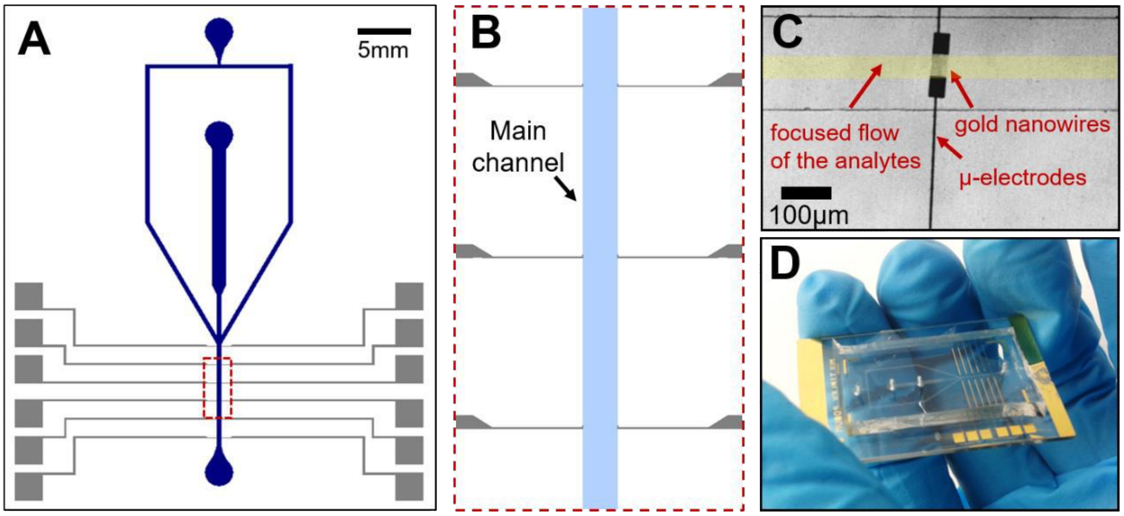

Figure 45: Integration of the two technologies: **(A)** Illustration of the alignment of the main channel to the sensors and the microelectrode structure. **(B)** Close-up of the channel alignment between the microelectrodes. **(C)** Microscope image of the main channel aligned over the nanosensors. The focused flow of analytes could be utilized for efficient and direct delivery of the analytes to the sensor. **(D)** Real-life appearance of the final sensor.

5.11 Dynamic SiO_2 particle detection

5.11.1 Single particle detection

Utilizing the integrated sensor platform, the first step included the detection of common unmodified SiO_2 particles with a diameter of 10 µm. Here, the 2D hydrodynamic focusing structure was applied to guide the particle solution, SiO_2 particles in 0.1x PBS probed with 0.1% Tween, over the sensing element between three streams of KCl solution (100mM). The applied flow rates described a ratio of $KCl_{vertical}$:$KCl_{horizontal}$: particle solution= 0.5:2:1, resulting in a focused particle solution stream which width matched the width of the sensing structure (see Figure 46, Inset 1, PBS: yellow; KCl: blue). Particle presence on the sensing structure was measured with an applied AC voltage of an amplitude of 0.5 V at a frequency of 100 kHz. In this, two parameters were measured: The output voltage response V_{out} from the input voltage and the phase shift from the reference frequency. On Figure 46, a close-up of a detection event of a 10 µm sized silica particle can be seen. In this, the baseline from the obtained raw data was subtracted, resulting in baselines at 0 V and 0°, where the magnitude of the detection signal of passing particles could be clarified directly as ΔV_{out} and ΔPhase. During baseline subtraction, the whole data set was subtracted by an envelope function. By subtraction of the initial data sets by their envelopes (positive envelope for V_{out} and negative envelope for the phase shift), the background signal could be successfully set to 0 V without influencing the peak signal magnitude. First, if no particle was present on the sensor, both ΔV_{out} and ΔPhase showed a stable baseline without any unspecific signal deviations (see Figure 44, region 1). Then, as soon as a particle crossed the sensing area, a drop of the output voltage ΔV_{out} and a simultaneous increase of the phase could be observed (see Figure 47, region 2). This effect was dedicated by the introduction of a new capacitor-resistor element to the device' equivalent circuit. Here, the particle's presence on the sensor was approximately 100ms, demonstrated in the peak width. When the particle left the sensor area, the signal equilibrated to its initial baseline value after the particle left the sensing structure (see Figure 46, region 3).

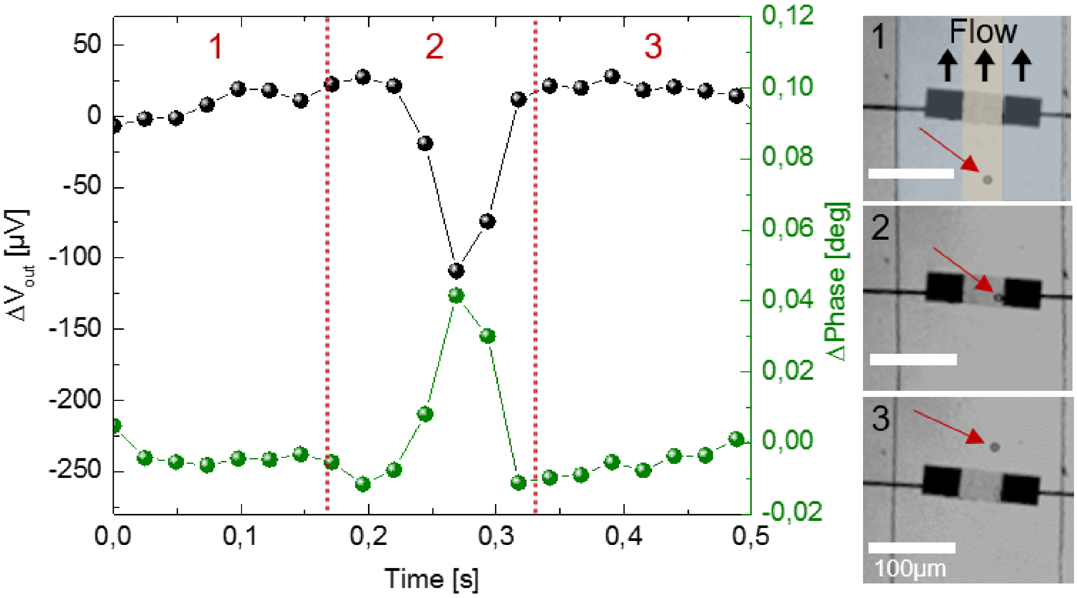

Figure 46: Close up of a 10 µm silica particle detection event. As soon as the particle entered the sensing area a decrease of V_{out} and an increase of the phase could be seen. The signal returned to the baseline value after the particle left the sensor.

5.11.2 Scatter plot representation

In order to be able to compare individual sensing experiments with various sensing areas, the height of the detection peaks, when a particle crosses the sensing area, were measured and taken as characteristic value for the respective kind of analyte used. For this, the baseline was subtracted of both amplitude and phase signals by subtracting the envelope data set from the same measurement from the original raw data, as already described in the previous chapter. Now, by measuring the height of the peaks, the characteristic peak height for the analyte could be determined for both parameters ΔV_{out} and ΔPhase (see Figure 47, left side). Here, the two detection peaks formed during a detection event were set into dependency, resulting in a scatter plot with ΔV_{out} as x-value and ΔPhase as y-value (see Figure 47, right side). The formed scatter cloud represented the characteristic signal alteration for one given type of analyte (here a SiO_2 particle with 10µm diameter), including deviations in both amplitude and phase changes.

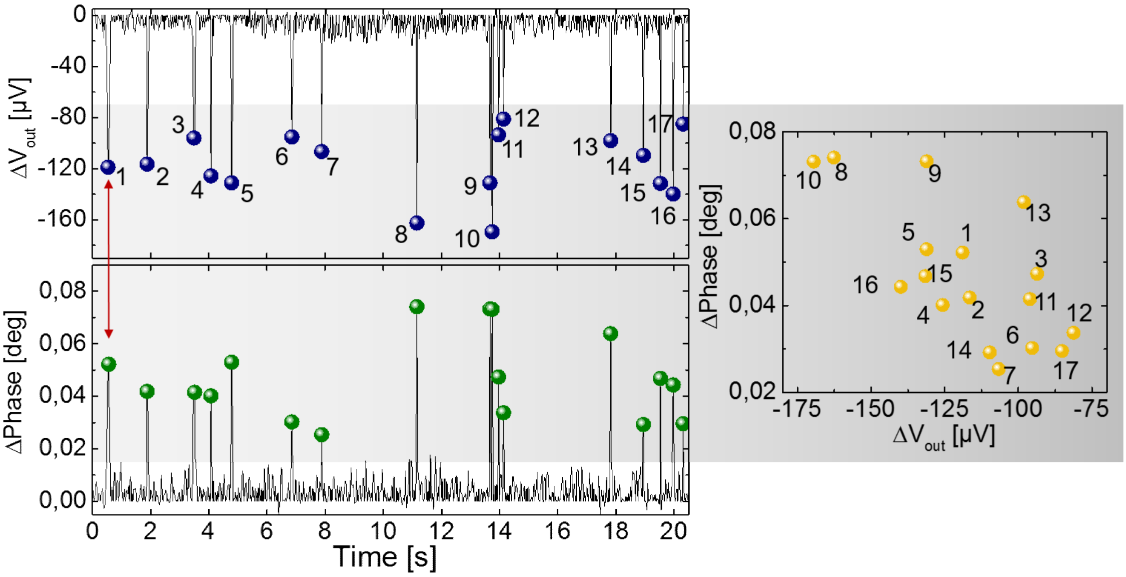

Figure 47: Scatter cloud determination: After baseline subtraction, peak heights of related amplitude and phase signal changes were set into dependency. The resulting scatter cloud represents the characteristic signal alterations for a given analyte.

5.11.3 Effect of the sensing area in dynamic particle detection

In order to evaluate the effect of the sensing area on the sensitivity of the device, 10 µm SiO_2 particles were detected by sensing structures with different numbers of interdigitating nanowire pairs, namely one pair (sensing area ~46 µm^2), 6 pairs (sensing area of ~506 µm^2) and 18 pairs (sensing area of 1610 µm^2). In order to compare the detection events for different sensing areas, the height of the detection peaks, when a particle was passing the sensor, was calculated as the percentual deviation of the peak signal to the baseline, the *signal-to-noise* ratio. For the highest sensing area (18 nanowire pairs, 1610µm^2) the detection peaks

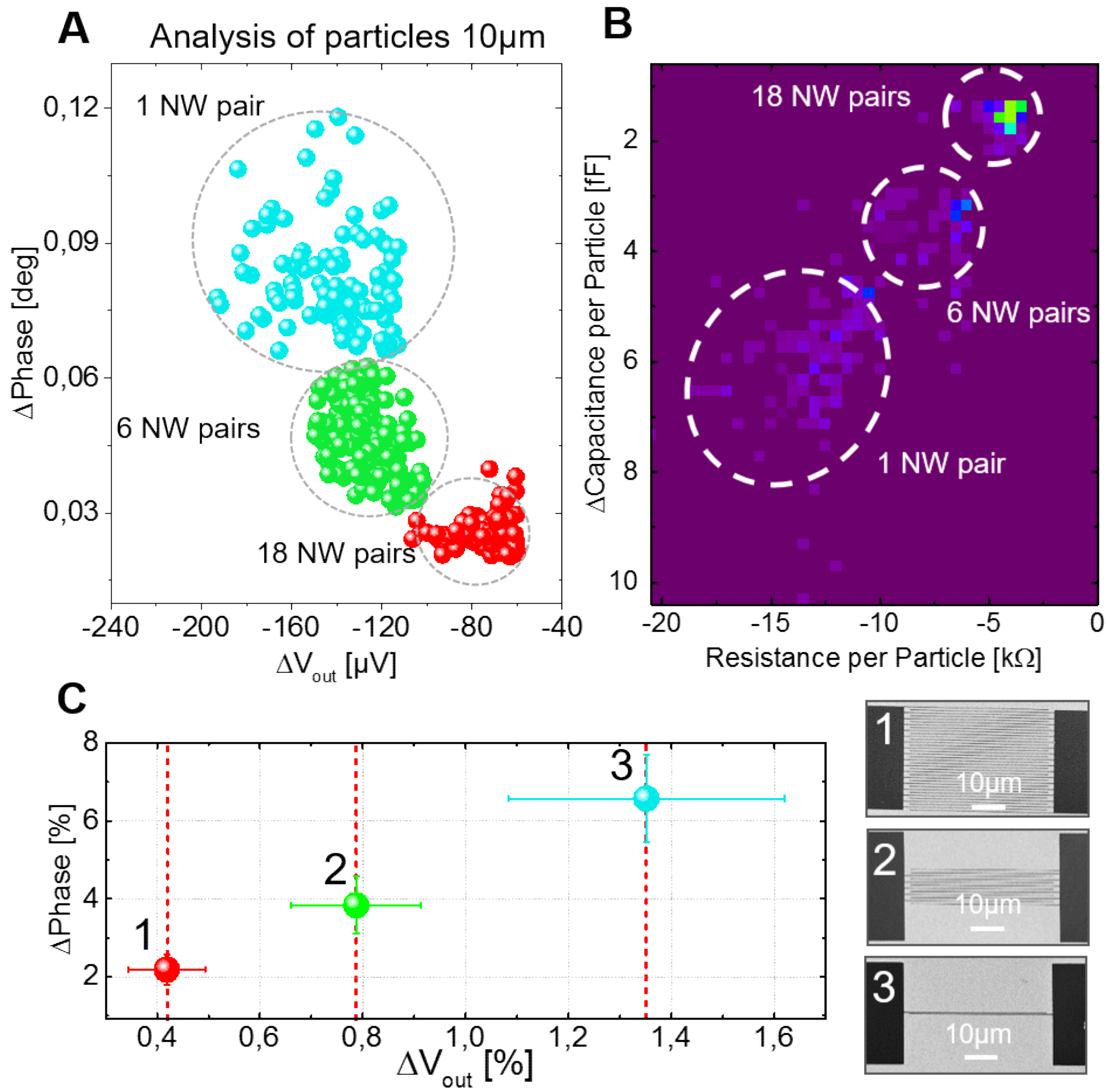

Figure 48: Evaluation of the sensing area on the signal strengths and deviations. (A) Signal-to-noise ratio analysis for different sensing areas: one pair (area ~46 µm^2), 6 pairs (area of ~506 µm^2) and 18 pairs (area of 1610 µm^2) of interdigitating nanowires. The decrease of the sensing area led to higher signal strengths, but also led to higher noise for independent detection events. (B) Sensitivity analysis of the device with respect to capacitance and resistance changes of the device. As before, larger sensing areas led to smaller, but more robust, signals, 0.02 fF and 2 MΩ for 18 pairs, while smaller areas increase both signal strength and noise, 10 fF and 15 MΩ for one single pair. (C) Percentual representation of the data clouds, demonstrating increasing values for decreasing detection areas. Further, the inner dispersity of the values within one data cloud is dramatically reduced if the sensor area is increased.

only showed a rather weak signal detection peaks, located between -60 µV and -100 µV in ΔV_{out} and 0,02° to 0,03° in ΔPhase (see Figure 48, panel A). Further, the height of the peaks was expressed in percentual values, based on the absolute difference of peak value and its corresponding baseline value. For 18 nanowire pairs the percentual difference was calculated to be at a mean value of 0.42% in ΔV_{out} change and 2,2% in ΔPhase (see Figure 48, panel C). In this scenario, the inner signal dispersity S_D of the data cloud was calculated to be at 14,53% and 13,13% for ΔV_{out} and ΔPhase, respectively. Here, the sensing width of the sensing was bigger than the analyte itself. Therefore, if a particle was present on the sensor, it was not able to cover all nanowires causing a partial signal compensation of the detection event by nanowire pairs, which were not under the influence of the analyte, since every nanowire pair could be considered as an individual capacitor. On the other hand, this compensation effect resulted in low signal deviation within the data cloud but in a more reliable signal readout. If the number of nanowire pairs was decreasing, the signal change was rapidly increasing, since the compensation effect of the unaffected sensing area was decreased. In detail, the signal variation for individual detection events was increasing, since the presence of the particle on the sensor at unavoidable different lateral and horizontal positions had a greatly enhanced impact on the strength of the signal. In this, the signal-to-noise ratios for six nanowire pairs, where the sensing width is close to the particle diameter, were found between -110 µV and -160 µV for ΔV_{out} (0,79%, S_D: 28,59%) and 0,03° to 0,06° for ΔPhase (3,83%, S_D: 23,43%). Further, if the sensing width was greatly decreased to only one nanowire pair, the signal revealed the strongest of the modulation increased between -120 µV and -200 µV for ΔV_{out} (1,35%, S_D: 36,72%) and 0,06° to 0,12° for ΔPhase (6,57%, S_D: 34,35%) (see Figure 48, panel A and C). In conclusion, the choice of the sensing area reflected a trade-off decision, where bigger sensing areas led to smaller and robust signals, while smaller areas lead to higher detection signals with higher noise. Further, the sensitivity of the device with respect to the change of the resistance and capacitance was evaluated. In this, the time-dependent signal of V_{out} and phase shift was transformed into change of the capacitance and resistance. For the capacitance, the earlier described formula (15) (see *Chapter 5.8*) was applied. Second, the resistance change was extracted from the amplitude of the complex impedance signal $R[\Omega] = \mathrm{Re}\{Z'\}$ (see *Chapter 5.6,* formula (7)). Further, the signal strengths of capacitance and resistance changes of detection events were subtracted by the baseline signals of the respective signals (as described in *Chapter 5.11.1*). In Figure 48 panel B, the contour plot with the density reflection can be seen for particle detection events from the same data set used in the previous analysis (see Figure 46, panel A and C). The trend of both signal and standard deviation matched the signal-to-noise calculations. While for the biggest sensing area (18 nanowire pairs) the capacitance and resistance changes in presence of the analyte were small and robust around 2 fF and -5 kΩ, they were greatly enhanced for single nanowire sensors, namely up to 6 fF and -15 kΩ. This analysis strengthened the findings from the previous analysis, demonstrating the direct effect of sensing area to both sensitivity and signal-to-noise ratio. For later experimental work, either the sensing areas including 6 pairs and 18 pairs were used since they grant enough sensitivity towards moving objects. Although the signal modulations were found to be highest for single nanowire pairs, the signal dispersity was too pronounced to differentiate objects with different diameters.

5.11.4 Dynamic detection of SiO_2 particles with different diameters

In the following, the sensitivity towards different diameters of SiO_2 particles was examined. Here, the frequency between the electrodes with a sensing area of 506 µm² (six interdigitating nanowires) was set to 100 kHz, allowing the probing of the size of passing analytes on the sensor. Firstly, the device was calibrated for SiO_2 particles with sizes of 3 µm, 5 µm and 10 µm. In this, solutions with one single type of particles were guided on the sensor and both the output voltage and phase shift were acquired. Here, the microfluidic parameters and liquids matched the previous experiments (see *Chapter 5.11.1*). Here, a clear dependence of the

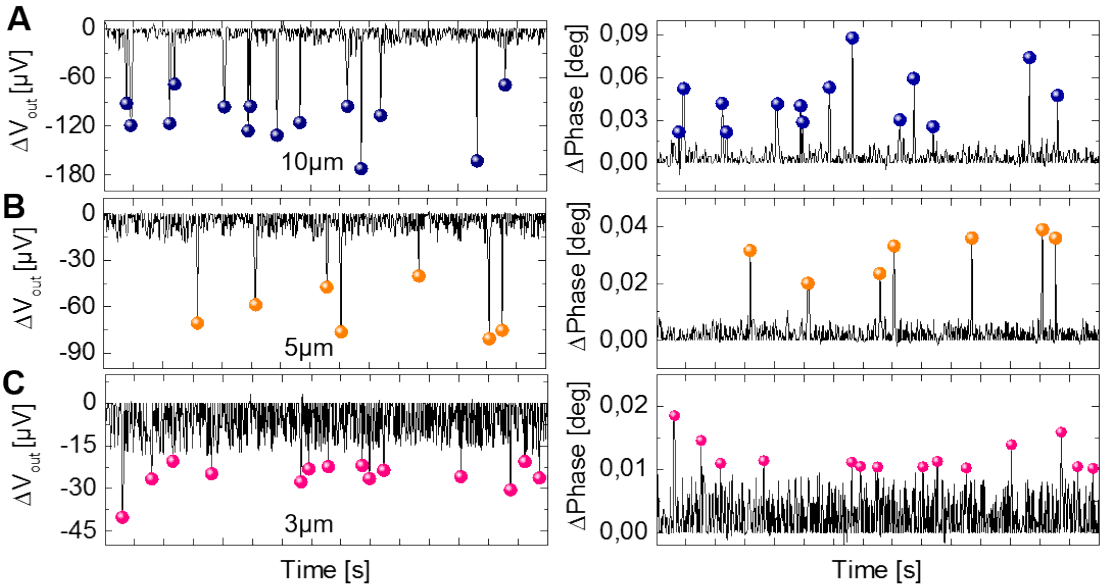

Figure 49: Detection of SiO_2 particles with different diameters. By application of a reference frequency of 100 kHz, the size of passing analytes could be probed. In this, a clear dependence of the detection signal strength on the diameter of passing particles could be observed. For 10 µm particles the resulting negative signal peaks were in the range of -80 to -120 µV and 0.03° to 0.09° (top), 5 µm signal strengths at -60 to -30 µV and 0.02° to 0.04° as well as -25 to -10 µV and 0.01° to 0.02° for 3 µm particles.

signal peaks of passing particles on their diameter could be observed (see Figure 49). After baseline subtraction, the resulting negative signal peaks for ΔV_{out} were in the range of -80 to -180 µV for 10 µm particles and 0.03 to 0.09° in ΔPhase (see Figure 49, panel A), matching the results from the previous chapter. After guidance of the 10 µm particle solution, the chip was cleaned thoroughly by flushing with deionized water till no 10 µm particle could be seen any more in the channels. Following, the microfluidic system was flushed with the 5 µm particle solution and the signal was captured with the same parameters as for 10 µm particle solution. Here, the reduced particle diameters led to smaller peak signal, namely -30 to -80 µV in ΔV_{out} and 0.02 to 0.04° in ΔPhase (see Figure 49, panel B). Further, the experiment was repeated for 3 µm particles, resulting in output signals of -20 to -40 µV and 0.01 to 0.02° in ΔPhase. In conclusion, a clear trend of the output signal magnitude in dependency of the particle diameter could be

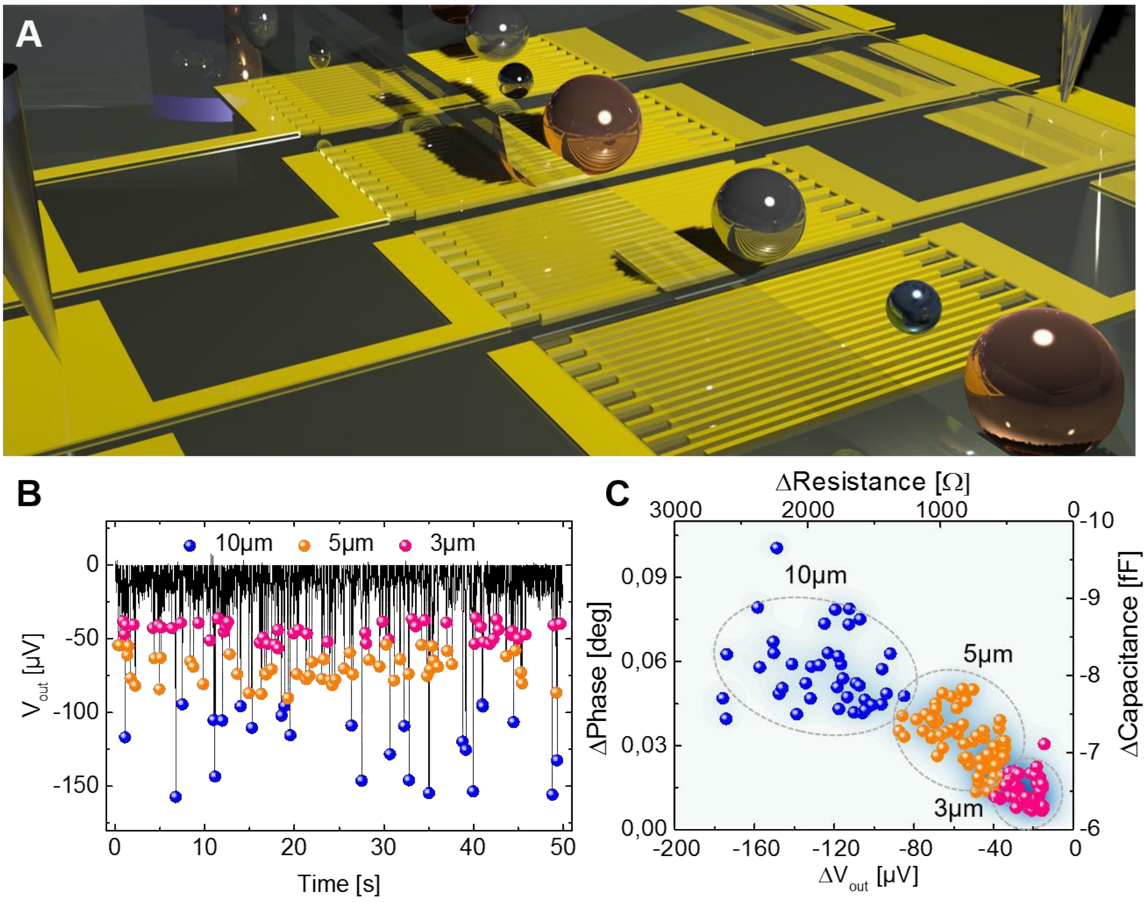

Figure 50: Detection of particles with different parameters in complex fashion. **(A)** Schematic illustration of the experiment. **(B)** Output signal of the sensor after baseline subtraction. Based on the classification in the previous experiment, the signal peaks could be classified into the various diameters of the particles, namely 10 µm, 5 µm and 3 µm. **(C)** Scatter plot of the individual peak signal pairs of amplitude and phase shift. The diameter of the unknown particles which were passing the sensor could be successfully classified by cluster formation of the peak signal pairs.

observed. By utilization of these calibration experiments, the classification of mixed particles became possible because of their known signal alterations.

Next, a solution containing a mixture of 10 µm, 5 µm and 3 µm particles was guided over the sensor and the signal was acquired (see Figure 50, panel A and B). The resulting signal with different magnitudes of peak events could be matched with the calibration data and allowed classification of the peaks to specific diameters. A representative example of the output response signal can be seen in panel B of the following figure, containing various peaks caused by different particles sizes. Compared to single particle experiment in the previous experiment, the output signal demonstrated detection peaks over the full response range from -20 µV up to -180 µV, resembling the detection events of particles with various diameters. Further, the output response was transformed to relative resistance and capacitance changes of the device, using the strategy from *chapter 5.11.3* (see Figure 50, panel C). In this,10 µm particles caused a resistance change of 1000 kΩ - 2500 kΩ between ΔV_{out} values of -80 µV to -180 µV. For smaller diameters the change was found to be at 500 kΩ-1000 kΩ and 250 kΩ-500 kΩ for 5 µm and 3 µm particles, respectively. Further, the related signal peaks in the phase shift and capacitance shift was gathered, where the signal strengths were found at 0.05°-0.09° and 8-9fF for 10 µm particles, 0.02°-0.05° and 7-8fF for 5 µm particles and 0.01°-0.03° and 6-7 fF for 3 µm particles. By representation in a scatter plot of the individual signal pairs (see Figure 50, panel C), a clear trend of the pairs depending on the size of the particles could be observed. By combination of the two parameters, amplitude and phase shift, at a size-probing frequency of 100kHz, differentiation of passing particle sizes could be successfully demonstrated. The analysis proves, that the sensor was sensitive to minor changes in the diameter of passing analytes, allowing the use of this platform as an impedance-based analyte counter.

5.12 Detection of peripheral blood mononuclear cells (PBMCs)

5.12.1 Overview

After demonstration of the sensor's sensitivity towards inorganic micro-objects with different sizes and proving that the developed platform could be used as a sensor, the type of analyte was altered to a biological species. In this, peripheral blood mononuclear cells (PBMCs) were chosen as the analyte of choice, since they offer a great biological impact in today's medical trials and assays. PBMCs represent a subfamily of human white blood cells taken involved in the immune response. In this, two main-families are present, originating from different stem cell progenitors: Monocytes and granulocytes, originating from myeloblasts and leukocytes having a common lymphoid progenitor. Furthermore, lymphocytes are additionally split between natural killer (NK) cells, T-lymphocytes and B-lymphocytes[145]. Each cell holds a specific task in the human immune response. Monocytes are progenitors of macrophages, responsible for phagocytosis, NK cells for rapid immune-response, B cells for antigen recognition and T cells for activation of several types of cells including B cells, macrophages and cytotoxic T cells[144]. Any defect in their function or in their development serves as an indicator for various diseases including several types of leukemia or cancer[156,157] (see *Chapter 2.5.1*). Thus, analysis of PBMC has a big impact in today's medical assays and tests for various diseases. In the following chapters,

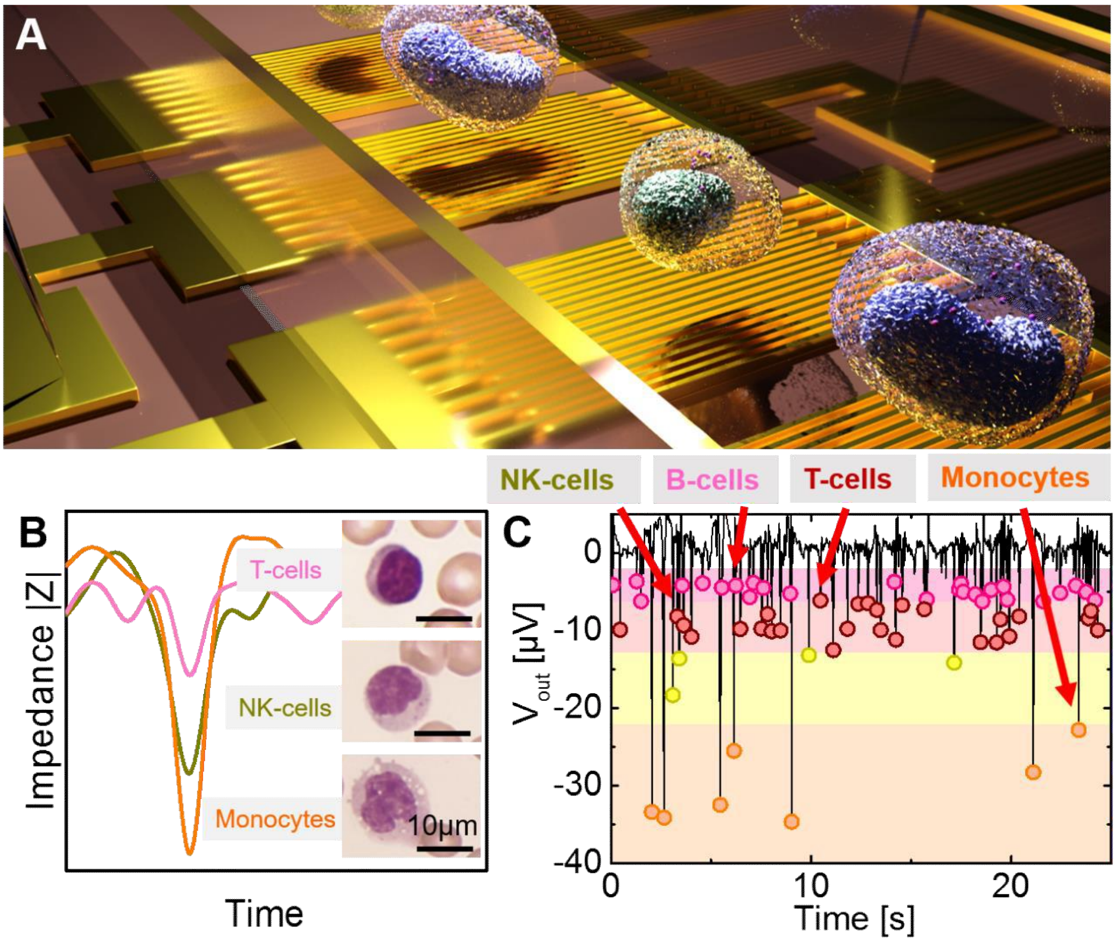

Figure 51: Conceptual description of PBMC detection. **(A)** Schematic illustration of the experiment, where the complex PBMC mixture is guided over the sensing structure. **(B)** Overlay of individual sensor responses towards different kinds of PBMCs. **(C)** Typical appearance of the acquired signal. The peak magnitude corresponded to the size of the cell, allowing classification of the signal to the cell type.

the analysis for human PBMCs using the developed platform is demonstrated, where the complex PBMC solution is guided towards the sensor (see Figure 51, panel A). In this, differentiation of PBMC subfamilies is possible since they possess different sizes and surface configurations. In the PBMC subpopulations, monocytes have the biggest sizes ranging while the various lymphocytes classes demonstrate smaller sizes. Thus, the various sub-families can be classified at 500 kHz, where monocytes showed the highest signal change, while NK-, B- and T cells showed decreasing peaks based on their size[144] (see Figure 51, panel B and C). A deeper analysis of the individual clusters, caused by the different cell species, is presented in the following paragraph.

5.12.2 PBMC classification detected by impedance cytometry

In the following, isolated PBMCs from a healthy human donor (male, age at 25) were guided untreated to the nanosensor and both amplitude and phase was acquired at a frequency of 500 kHz. In this, the PBMC population was purified from whole blood samples using FICOLL technique, where only monocytes and lymphocytes (B cells, T cells and NK cells) are present in the sample. In order to be able to classify the clusters, formed by the peak pairs of amplitude and phase, the percentage of abundance of peak pairs was analyzed. In healthy human PBMCs, the individual cell types have a distinct range of percentage in the sample. Here, the percentual composition was determined using conventional flow cytometry, where the monocyte population and lymphocyte population was evaluated by detection of the side-scattered light (SSC) and forward-scattered light (FSC) of passing analytes in the nozzle (see Figure 52, panel A). Here, the monocyte population within the sample was found to be at 11,80%, while the lymphocyte population was found at 88,20% (see Table 6). Further, the distribution of subfamilies of lymphocytes were determined by fluorescent labeling of the surface-specific antigens of the individual cells classes, namely CD3 for T cells, CD20 for B cells and CD56 for NK cells. As a double check, monocytes were fluorescently labeled with $CD14^+$ (see Figure 52, panel B-D). In this, a total cell number of 20,000 was used for the percentual distribution of the subfamilies, resulting in 57,50% for T cells, 30,70% for B cells and 10,10% for NK cells (see Table 6). Now, PBMCs from the same donor were analyzed using the developed nanowire impedance sensor platform. Here, only 5µl of PBMC solution was needed to fully characterize the PBMC percentual composition. As before, the PBMC solution was guided to the sensing geometry using the 2D hydrodynamic focusing system at the same flow and electrical parameters (see *Chapter 5.11*). Here, the scatter plot representation of the data peak pairs ΔV_{out} and Δ_{Phase} can be seen on the following figure, panel A. In the plot, two main cluster could be observed, where one cluster (right side) is separated into three sub-clusters (see Figure 53, panel A). Based on the knowledge, that monocytes are larger than lymphocytes in total, and could cause higher signal peaks, the cluster was classified as the monocyte populations. This assumption was verified by the percentage analysis of the population. In this, the monocyte cluster had a percentage of 9.84% while the other cluster (now referred as the lymphocyte cluster) was found to be at 90.16% (see Table 6). This finding strongly strengthens the applied classification of monocyte and lymphocyte sub-populations. Further, a more detail analysis of the lymphocyte cluster was carried

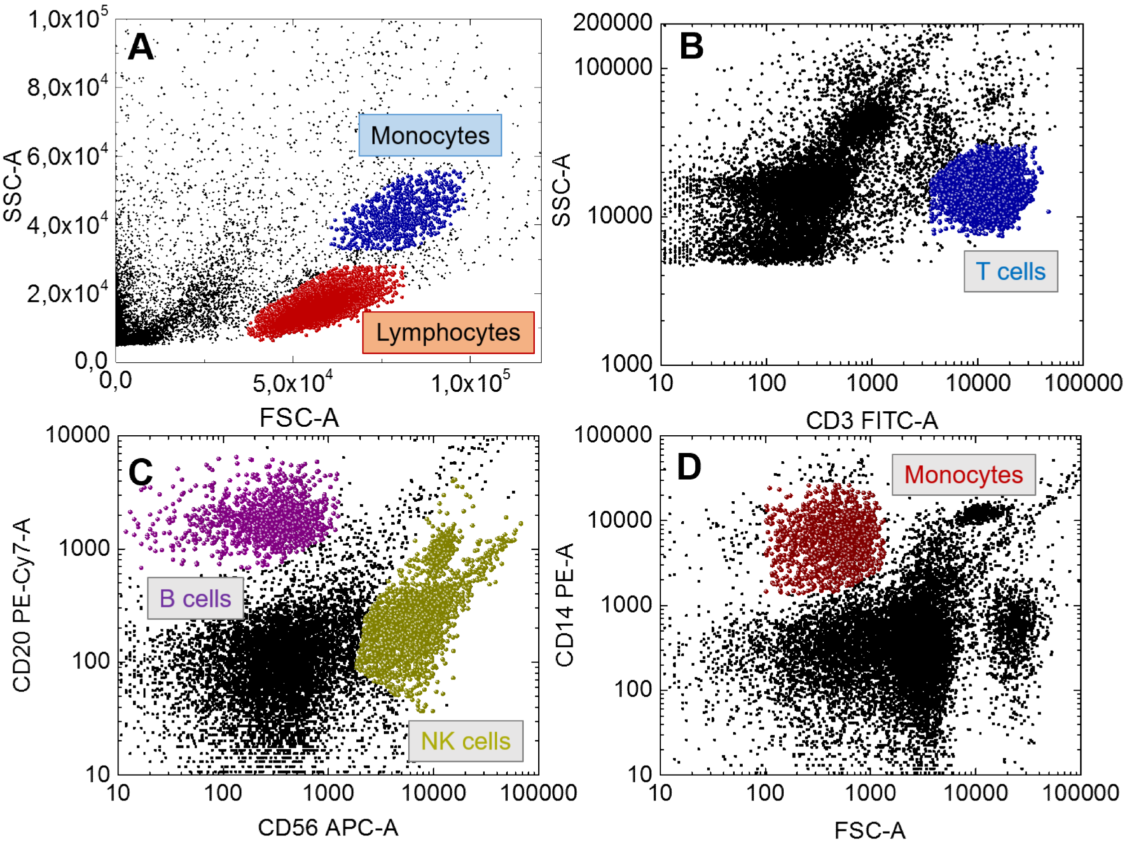

Figure 52: Detection and classification of PBMC subpopulations using conventional flow cytometry. Flow cytometry forward (FSC) and side scattering (SSC) plot of the population. The data clearly showed the presence of monocyte population (blue) and lymphocyte population (red). **(B)** Surface protein fluorescent marking of CD3^{+} for identification of T cells and **(C)** CD20^{+} for B cells, CD56^{+} for NK cells and **(D)** CD14^{+} for monocytes. Based on these plots, the percentual composition of the sample could be determined (see Table 6).

Table 6: PBMC subfamily distribution measurement, calculated for conventional flow cytometry and the nanocytometer

Cell Type	Monocytes	Lymphocytes	T cells	B cells	NK cells
Flow cytometer	11,80%	88,20%	57,50%	30,70%	10,10%
Nanocytometer	9,84%	90,16%	62,31%	31,34%	7,34%

out. Here, three sub-clusters could be distinguished with percentage values of 7.34% (red), 62.31% (purple) and 31.34% (green) (see Figure 53, panel B). With the aid of these values, the sub-clusters could be identified to their respective lymphocyte cells by comparison with the values obtained from flow cytometry: Slightly bigger NK cells with the lowest percentage (red), T cells with the highest abundance (purple) and B cells at intermediate abundance (green). Taken these two parameters into consideration, cell size and percentage, the peak pair cluster could be successfully classified, completely defining the analyzed sample.

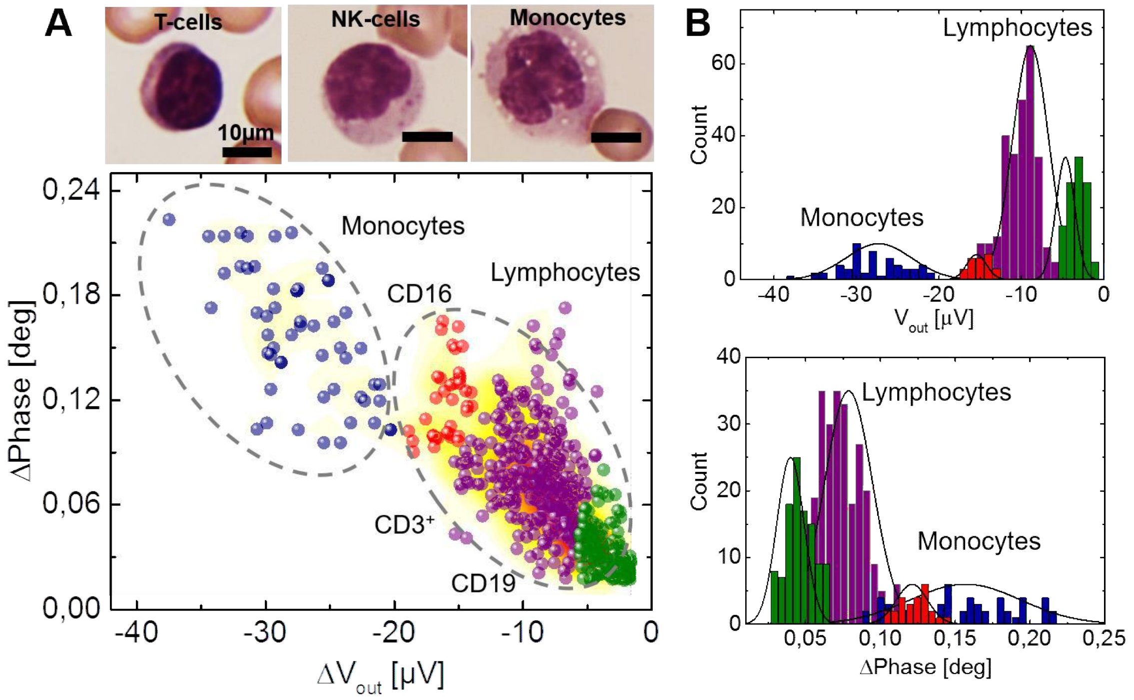

Figure 53: Detection and classification of PBMC subpopulations: **(A)** Impedance cytometry data for whole analysis of PBMCs. Two main clusters could be identified: monocyte population (left side) and lymphocyte population (right side). Additionally, the lymphocyte cluster showed three sub-clusters, referring to the NK cell (red), T cell (purple) and B cell (green) populations **(B)** Percentage analysis of the cluster for correct classification of the clusters. The measured percentage values were in good agreement.

5.12.3 PBMC Long-time detection

In total, the experimental sample measuring span could be increased up to several hours without damaging the device. On the following figure, a complete typical measurement for PBMCs from the healthy donor from the previous chapter can be seen. Here, the complete measurement of ΔV_{out} of healthy human PBMCs were detected at 500 kHz with a sensing area of 506 µm² with an amplitude of 0.5V over a time span of 25 minutes. In this, over 4000 cells could be detected with a rate of 2.6 cells per second using a flow rate of 1 µl/min, thus 25µl of analyzed sample volume. The individual subpopulations could be clearly identified, namely NK cells (yellow), T cells (pink) and B cells (red) and monocytes (orange) (see Inset). The supposedly decrease of the noise during the measurement (starting at approximately 12 minutes) is due to the lowering concentration of PBMCs in the channel as the sample liquid was pushed through the channel. This effect could be attributed by sticking of cells to the inner part of the teflon tubes.

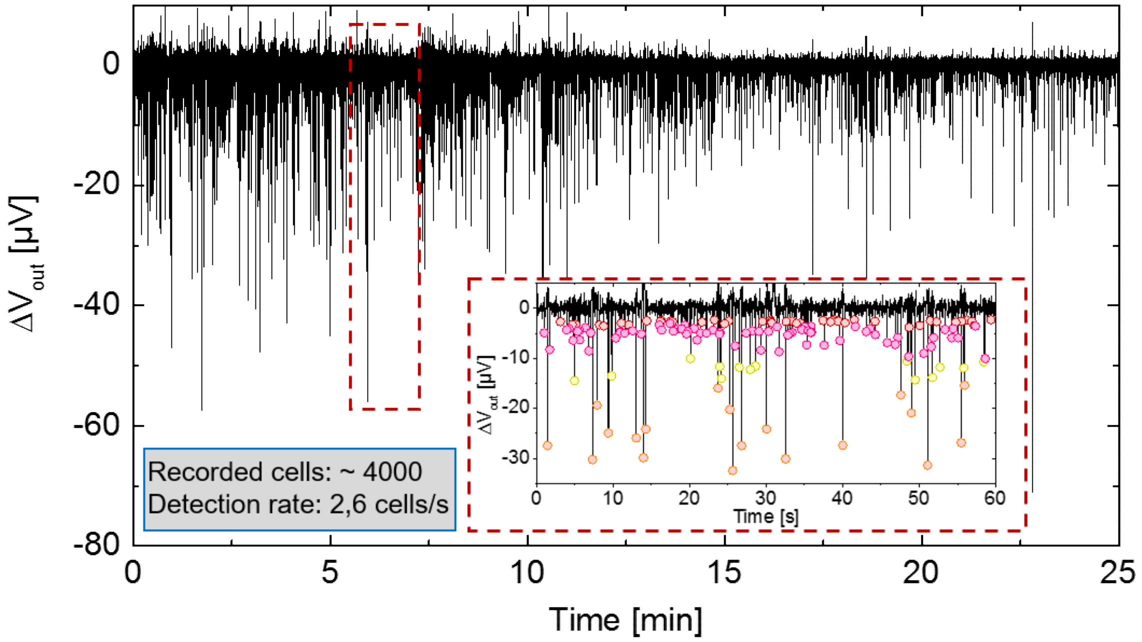

Figure 54: Long-time experiment of PBMCs from a healthy donor at 500 kHz and 0.5 V. Subpopulations could be clearly identified over the whole time span (see Inset). In total, over 4000 cells could be detected and classified at a detection rate of 2.6 cells per second.

5.13 Detection of acute myeloid leukemia by impedance cytometry

5.13.1 Manual analysis of the output response

In this section, the capability of the developed platform for disease diagnostic is demonstrated. Here, PBMC populations can be utilized for detection of various diseases, *e.g.* acute myeloid leukemia (AML). In this type of cancer, patient suffer from a high percentage of leukocytes in their blood, which population is highly probed with undifferentiated stem cell progenitors of monocytes and granulocytes, *the myeloblasts*. The cancerous myeloblasts are circulating in the blood with a very high dividing rate, influencing the composition of both whole blood and PBMCs[153]. Therefore, impedance analysis is an adequate tool for identification of the different compositions from healthy donors and patients, who suffer from leukemia. In this, PBMCs were isolated from healthy human donors and patients, where AML was diagnosed. Further, the composition, based on the knowledge from the previous paragraph, was analyzed. For healthy donors, the composition of PBMC subpopulations showed the same trend as before with two main clusters, monocyte and lymphocyte clusters, at the correct percentage values: Monocytes 18.57%, lymphocytes 81.42%, T cells 60.74%, B cells 25.51% and NK cells 13.75% (see Figure 55, panel A and Table 7). In contrast, the PBMC analysis for a leukemia donor showed lower abundance of lymphocytes at 38.86%, while the population of monocytes is increased to 29.62% (see Figure 55, panel B and Table 7).

Table 7: Leukocyte distribution differences between healthy human PBMCs and AML-infected PBMCs

Cell type	Monocytes	Lymphocytes	T cells	B cells	NK cells	Myeloblasts
Healthy donor	18,57%	81,42%	60,74%	25,51%	13,75%	0%
AML patient	29,62%	38,86%	61,53%	21,30%	17,17%	31,52%

The increase of monocytes and decrease of lymphocytes are in agreement with the disease picture of AML. Additionally, a newly formed cluster could be found, located close to the monocyte cluster (black data point points). By percentage analysis, this cluster was found to be at 31.52%. Defined by the World Health Organization (WHO) AML is classified by a myeloblast percentage starting from 20%[223]. Based on the correct percentage of the myeloblasts, as well as the close relation to monocytes since they represent their progenitor, the cluster was classified as the myeloblast cluster. In conclusion, a clear difference between healthy human donor PBMC and AML patient could be successfully demonstrated. Therefore, the developed sensor platform is suitable to serve a point-of-care diagnostic tool for easy and fast screening of PBMCs and their related diseases.

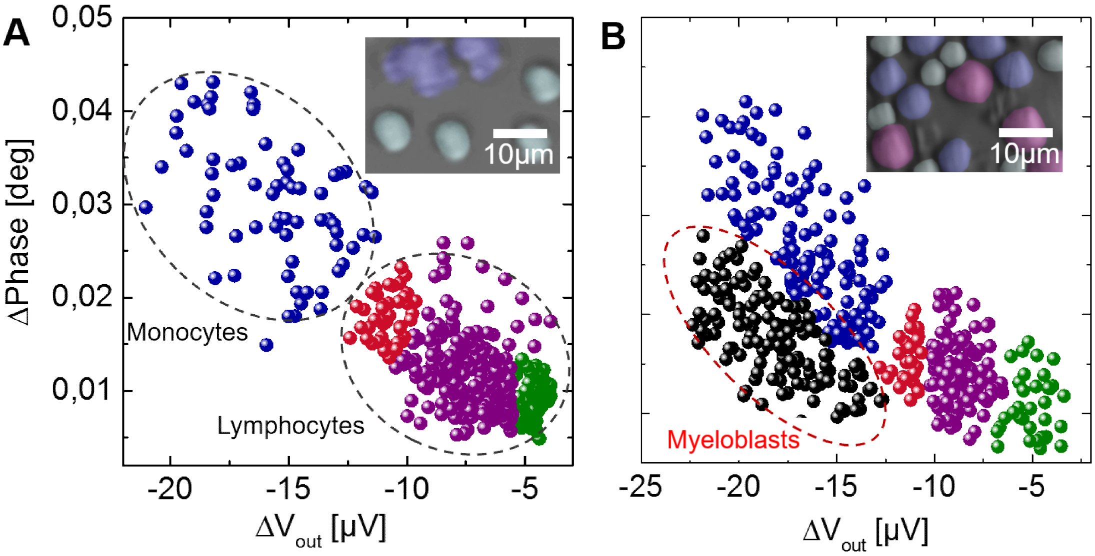

Figure 55: Comparison between healthy human and AML PBMC subpopulations. (A) Healthy human donor PBMC sub-population demonstrate the correct trend of cell type abundance: Monocytes (blue), NK cells (red), T cells (purple) and B cells (green). (B) In AML patient PBMCs, the lymphocyte percentage is decreased while the percentage of monocytes is increased. Additionally, a new cluster could be found (black data points), demonstrating the abundance of myeloblasts in the PBMC sample.

5.13.2 Learning algorithm for automatic cell classification

Finally, in order to accelerate the data analysis and to open the route towards an automatic analysis of the collected response data, a learning algorithm for automatic cell classification was developed. In contrast to manual analysis, the application of an automated cell classification strategy greatly improves the data throughput granting huge time savings as well as unbiased and more precise cell classification. In recent years, successful application of automated classification of biological detection has been demonstrated, greatly improving the performance of biosensors with respect to data processing[224–227]. In this, the same response data of the sensor from the previous chapter for healthy and AML PBMCs was used in order to compare the results from automatic and manual treatment of the data. Here, the developed algorithm for automatic output clustering could be divided into 5 subparts. In the following, an overview of the individual steps can be seen. Firstly, the signal profile was approximated using a smoothing spline:

$$\sum_{i=1}^{n}\left(Y_i - \mu(x_i)\right)^2 + \lambda\int_{x_1}^{x_n}\mu''(x)^2 dx \tag{19}$$

The application of this spline minimizes approximation errors leading to an evaluation of the true signal baseline, followed by its subtraction from the raw signal. Following, peak signals from both signals (ΔV_{out} and ΔPhase) were detected simultaneously by application of an outlier analysis in the interquartile range from Q_1 of 25% to Q_3 of 75% percentile:

$$IQR = Q_3 - Q_1 \tag{20}$$

Here, the peaks were considered as deviations from the baseline and the range definition gave rise to exclude outliers and set the minimum height of true cell detections. Subsequently, the data was filtered towards false positive cell detection due to multiple neighboring peaks. Here, only the highest peak value was taken into consideration. Following, isolation forest algorithm[228] was utilized for discarding outliers from obtained peak spaces. Finally, K-means clustering[229] strategy was used for classification of the data peak pairs into clusters for determination of their mean, standard deviation and distribution characteristics. By this analysis, automatic differentiation of PBMCs from healthy donors and AML patients became possible (see Figure 56). Here, the data treatment allowed clustering of the individual color codes, which classify further detection events and can be utilized as a *classification map* for samples with unknown PBMC composition. In this, these maps reflect differences in the PBMC composition and can be utilized for detection of various diseases which influence percentual differences or occurrence of new cells in the PBMC composition. In conclusion, this strategy opens the path towards a multiplexed analysis of various white blood cell related diseases by automatic pattern recognition and creation of a library at low-computational effort.

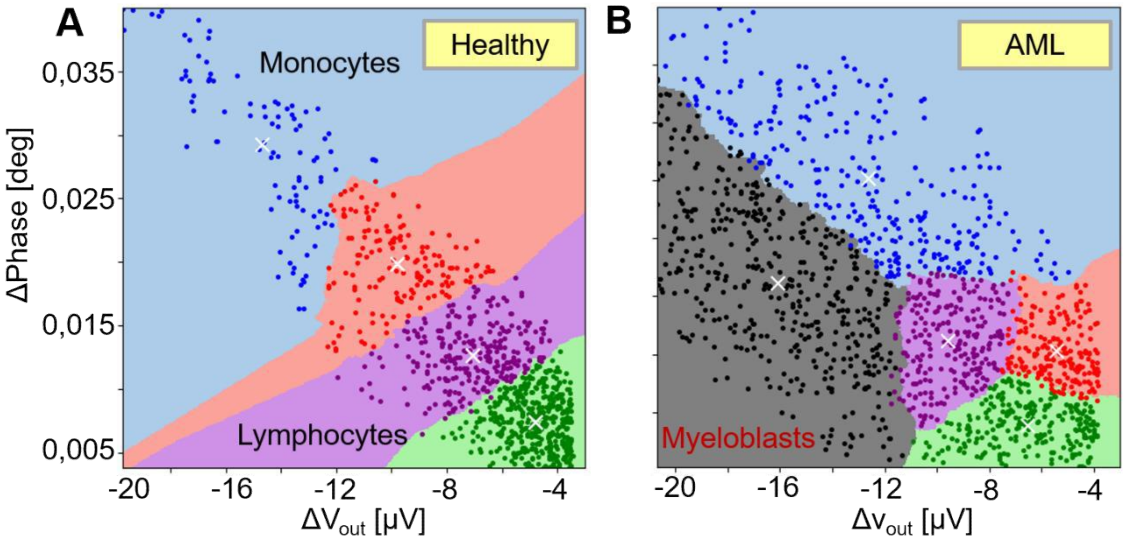

Figure 56: Application of the learning algorithm for automatic cell signal detection and classification. Here, PBMCs from healthy donors and AML-patients revealed differences in their percentual composition as well as the occurrence of myeloblasts in AML. Based on the creation of a color classification map, a map library for easy identification of various white blood cell diseases became possible.

5.14 Exploring the detection limit of the device

Till today, there are no findings on the detection and classification on unlabeled bacteria was observed in the field of impedance cytometry. Since the developed platform showed excellent sensitivity to the phenotype of organic and inorganic analyte, the sensor was tested for various microorganisms in order to explore the detection limit. Here, the sensor area was decreased to a sensing area of 46 µm² (one pair of nanowire electrodes) for enhanced sensitivity for smaller objects at a frequency of 500 kHz at 0.5 V, since bigger sensing areas did not show any sensitivity towards these small objects. In the following, four bacterial species were independently detected and classified. The used bacteria strains and their properties can be seen in the following table. In this, the various strains demonstrated only small differences in their sizes, phenotypes and gram staining and are adequate to explore the detection limit of the device. The resulting peak pair signals can be seen on the following figure. In this, differences in the pairs could be observed for the different strains. For two rod-shaped bacteria, *b. subtilis* (green) and *e. coli*, an L-shaped data cloud could be observed (see Figure 57). This effect is due to the different orientation of single bacterial cells as they pass sensor, since non-spherical objects cause alterations in their detection signal in EIC, depending on their orientation as they pass the sensor[230]. Here, the signal the of the two bacteria was overlapping, since they showed similar sizes (see

Table 8: Bacteria strains used in impedance cytometry and their properties

Bacteria strain	Phenotype	Size	Gram stain
Bacillus subtilis	rod-shaped	4-10µm x 0.25-1 µm	gram+
Escherichia coli	rod-shaped	2µm x 0.25-1µm	gram-
Lysinibacillus sphaericus	rod-shaped	1-5µm x 0.6-1 µm	gram+
Sporosarcina ureae	coccus	1 - 2,5µm	gram+

Table 8). Additionally, various stages in the development of bacteria influence the signal, in detail maturation of the bacteria or cell division state. For round-shaped bacteria, *s. ureae*, the L-shape could not be observed, but a rather big cluster compared to its overall size. This can be explained by the

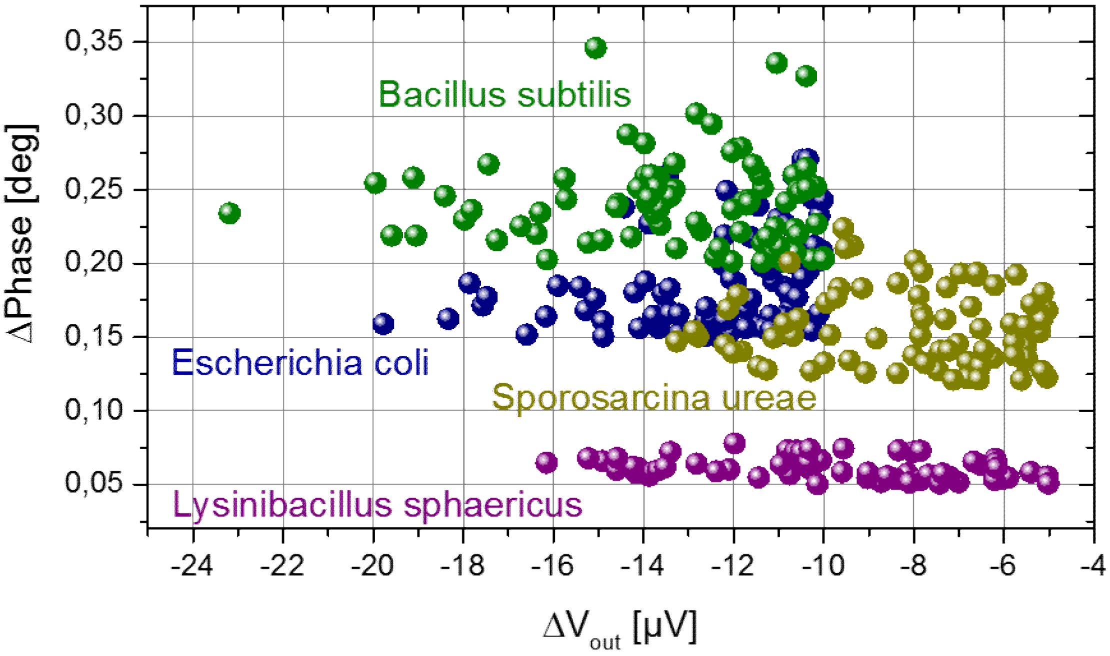

Figure 57: Detection of various bacterial strains using the developed sensor platform. The device shows sensitivity towards the phenotype of the analyzed bacteria. Rod-shaped bacteria, *b. subtilis* and *e. coli*, demonstrated L-shaped cluster formation due to their different orientation when they pass the sensor. Coccus-shaped bacteria, *s. ureae*, on the other hand, showed a round-like and large cluster due to their roundish shape and their ability to form clusters of up to 9 independent cells. Rod-shaped *l. sphaericus* did not show the same trend as the other rod-shaped bacteria with a rectangular shape with high deviation in amplitude but nearly not deviation in the phase. Further investigations have to be made to understand this behavior.

characteristic of *s. ureae* to form clusters of up to 9 single cells[231]. Thus, the resulting cluster showed a round-like and large cluster. Lastly, rod-shaped *l. sphaericus* showed no characteristic L-shape appearance of the cluster, but a rectangular cluster with nearly no deviation in the phase signal and large alteration in the amplitude signal. Till now, this trend cannot be explained and further investigations in this directions have to be made. In conclusion, the spirit of this experiment was to demonstrate the detection limit of the device showing sensitivity towards various bacterial strains. In order to improve the sensitivity of the device on the lower micron-scale, optimizations in both microfluidics and sensor geometry have to be examined.

6. Summary and outlook

The presented work focused on the microfluidic integration of nanosensing elements in the spirit of biosensing applications. Here, the conjunction of these elements and their microfluidic integration grants analyte delivery and protection from outer influences on one platform and is essential for transportable point-of-care devices. The utilized microfluidic channels were modified for additional functionalities aside from analyte delivery, namely the introduction of isolated aqueous droplets in a carrier stream and analyte focusing in two dimensions.

In the first part of the work, microfluidic droplets were detected using SiNW technology based on a pure electrical sensing of their chemical environment. Till now, microfluidic droplet detection is mainly based on optical imaging methods, *e.g.* by microscope analysis or fluorescent imaging. Thus, bulky devices are needed for signal readout in droplet microfluidics which makes the platform non-transportable, has to be operated by trained personnel and requires expensive labeling molecules which may also alter the original signal. For the first time, electrical sensing of microfluidic droplets was demonstrated which directly sensed the chemical environment of them, based on the inner electrical conductance of the liquid as well as its pH value and ionic concentration. Further, time-depending changes of the composition of passing droplets were successfully observed. This opens a new route towards a new detection scheme for microfluidic droplets without the use of indirect fluorescent detection and can greatly minimize the need for bulky equipment, essential for a transportable point-of-care diagnostic platform. Further, droplet microfluidics offers the possibility to separate the sample into nanoliters compartments, allowing a broad range of analytical assays. For instance, conventional conductance and pH value measurements, for which big volumes (tens of milliliters) are needed till now, can be also carried out in the nanoliter regime, especially beneficial for analysis of expensive and valuable liquid samples. Further, the developed platform can be utilized in biological or pharmaceutical assays by applying a concentration gradient among an isolated droplet array, probed with microorganisms. Since bacteria cause a decrease of the pH value in their environment, the critical concentration of inhibition of the tested drug, molecule or antibiotic can be evaluated by tracking the pH value of passing droplets over the FET. Finally, even minor changes of the ionic concentration of pH value changes can be tracked more precise in the nanoliter regime, compared to macro-volumes. Here, the next optimization step is the down-scaling of the peripheral devices, namely the probe station setup and the sourcemeter, and the multiplexed connection of several FET structures. These steps can be combined by integration of the FET-chip on a SD-card connected to a small readout device, which is controlled and powered by an USB connection, directly to the computer. This device has been already realized in our chair, but has not yet been utilized with droplet microfluidics.

In the second part of the work, the first chip for impedance cytometry detection using nanostructured materials as sensing geometry was fabricated, characterized and utilized as measurement platform for differentiation of PBMC cells of healthy humans and AML patients. The utilization of nanostructures greatly improves the sensitivity of the device towards analytes which come into the field of influence of their electric field. Here, the laboratory steps from the idea to the finalized sensor platform were described. During this process, the dependency of the signal-to-noise ratio and sensitivity on the sensing area could be successfully described, *i.e.* smaller sensing areas lead to higher signal strengths but also lead to higher noise. Without any special sample treatment, isolated PBMC cells were guided over the sensing structure and were differentiated based on their size. Additionally, conventional flow cytometry helped to identify the formed signal clusters to their respective cell type. The results of flow cytometry and impedance cytometry were in excellent agreement. Based on these findings, differentiation of PBMC cells from cancer patients could be identified for the first time using EIS. By application of a learning algorithm, which is capable to extract the data points from raw signal and identify and classify the clusters, the developed system was boosted the next level concerning data treatment protocols. The combination of the sensor and the learning algorithm opens the path for a transportable device for point-of-care diagnostic for detection of micron-sized objects in *e.g.* blood, saliva or urine. In order to achieve this goal, few optimizations of the device have to be made, *e.g.* the reduction of the influence of the contact pads on the electric field. This can be achieved by increasing the length of the nanowires, so that the contact pads are located outside of the microfluidic channel. Further, the stability of the nanowires has to be improved since they are not very robust; a thin oxide protecting layer on top of the electronic structure, deposited by *e.g*. atomic layer deposition (ALD), can be utilized for this purpose. This platform offers the possibility to further increase the density of sensors on the substrate. Like in the previous part, multiplexed analysis of single samples at different frequencies to probe various parameters of the medium or even analysis of multiple liquid samples at once. In this, double detection of the same analyte at different frequencies can be utilized for extraction of the membrane characteristics without the influence of the its size. Further, the learning algorithm can be further trained via deep learning methods to recognize specific patterns of scatter data for various (non-)biological samples accompanied diseases or contaminations. The generation, learning and recognition of the scatter plot patterns formed by the various samples would lead to higher impacts in *e.g.* biomedical assays and test, contamination testing in *e.g.* wastewater analysis or biological applications like differentiation assays in stem cells development.

Scientific output

Publications in peer review journals

J. Schütt, E. Avitabile, G. Milyukov, L. Delogu, M. Rauner, M. Middeke, K. Sockel, L. Baraban and G. Cuniberti, *Nanocytometer for detection and smart analysis of acute myeloid leukemia: a pilot study*, submitted

S. Klinghammer, T. Uhlig, F. Patrovsky, M. Böhm, **J. Schütt**, N. Pütz, L. Baraban, L.M. Eng, and G. Cuniberti, *Plasmonic biosensor based on vertical arrays of gold nanoantennas.* ACS Sens., 2018, doi:10.1021/acssensors.8b00315

E. Baek, T. Rim, **J. Schütt,** K. Kim, C.-K. Baek, L. Baraban, G. Cuniberti, *Negative photoconductance in heavily doped Si nanowire field-effect transistors*. Nano Lett., 2017, 17 (11), pp 6727–6734

J. Schütt, B. Ibarlucea, R. Illing, F. Zörgiebel, S. Pregl, D. Nozaki, W. M. Weber, T. Mikolajick, L. Baraban and G. Cuniberti, *Compact Nanowire Sensors Probe Microdroplets*, Nano Lett., 2016, 16 (8), pp 4991–5000

Selected conference contributions

Oral Presentations

J. Schütt, B. Ibarlucea, R. Illing, F. Zörgiebel, S. Pregl, D. Nozaki, W. M. Weber, T. Mikolajick, L. Baraban and G. Cuniberti, *Compact Nanowire Sensors Probe Microdroplets*, DPG Frühjahrstagung, 2017, Dresden, Germany

L. Baraban, **J. Schütt**, B. Ibarlucea, R. Illing, F. Zörgiebel, E. Baek, D. Nozaki, A. Nerowski, L. Römhildt, A. Gang, and G. Cuniberti, *Detection of Diseases at the early Stage*, Trends in Nanotechnology (TNT), 2017, Dresden, Germany

J. Schütt, B. Ibarlucea, R. Illing, F. Zörgiebel, S. Pregl, D. Nozaki, W. M. Weber, T. Mikolajick, L. Baraban and G. Cuniberti, *Compact Nanowire Sensors Probe Microdroplets*, DPG Frühjahrstagung, 2016, Regensburg, Germany

Poster Presentations

J. Schütt, E. Avitabile, G. Milyukov, L.Delogu, M.Rauner, M. Middeke, K. Sockel, L. Baraban and G. Cuniberti, *Nanocytometer for detection and smart analysis of acute myeloid leukemia*, EMBL The European Molecular Biology Laboratory (EMBL) Microfluidics Conference, 2018, Heidelberg, Germany

J. Schütt, L. Baraban and G. Cuniberti, *Real-time in-flow impedance sensing of microparticles using gold nanowires*, Trends in Nanotechnology (TNT), 2017, Dresden, Germany

J. Schütt, L. Baraban and G. Cuniberti, *Real-time in-flow impedance sensing of microparticles using gold nanowires*, European Conference on Molecular Electronics (ECME), 2017, Dresden, Germany

J. Schütt, L. Baraban and G. Cuniberti, *Nanoscaled impedance cytometry for electrical bacteria analysis*, NanoBioSensor Conference, 2017, Dresden, Germany

J. Schütt, S. Pregl, F. Zörgiebel, B. Ibarlucea, L. Römhildt, W. Weber, T. Mikolajick, L. Baraban and G. Cuniberti, *Droplet-based microfluidics meets silicon nanowire sensors*, The European Molecular Biology Laboratory (EMBL) Microfluidics Conference, 2014, Heidelberg, Germany

Exhibition

R. Illing, **J. Schütt**, L. Baraban and G. Cuniberti**,** Demonstration of millifluidic droplet analyzer prototype, Nanofair 2014, Dresden, Germany

References

1. United Nations, Department of Economic and Social Affairs ,. Population Division. World Population Prospects: The 2017 Revision, Volume II: Demographic Profiles (ST/ESA/SER.A/400). (2017).

2. 13. koordinierte Bevölkerungsvorausberechnung. Available at: https://service.destatis.de/bevoelkerungspyramide/#!y=2018. (Accessed: 1st August 2018)

3. Majumder, S., Mondal, T. & Deen, M. J. Wearable Sensors for Remote Health Monitoring. *Sensors* **17,** (2017).

4. Milenković, A., Otto, C. & Jovanov, E. Wireless sensor networks for personal health monitoring: Issues and an implementation. *Comput. Commun.* **29,** 2521–2533 (2006).

5. Lynch, J. P. A Summary Review of Wireless Sensors and Sensor Networks for Structural Health Monitoring. *Shock Vib. Dig.* **38,** 91–128 (2006).

6. FreeStyle Libre – Blutzucker messen ohne Stechhilfe. Available at: http://www.freestylelibre.de/. (Accessed: 22nd February 2018)

7. Wan, H., Yin, H., Lin, L., Zeng, X. & Mason, A. J. Miniaturized planar room temperature ionic liquid electrochemical gas sensor for rapid multiple gas pollutants monitoring. *Sens. Actuators B Chem.* **255,** 638–646 (2018).

8. Zilberstein, G. *et al.* A miniaturized sensor for detection of formaldehyde fumes. *ELECTROPHORESIS* **38,** 2168–2174

9. Lee, T. M.-H. Over-the-Counter Biosensors: Past, Present, and Future. *Sensors* **8,** 5535–5559 (2008).

10. Luka, G. *et al.* Microfluidics Integrated Biosensors: A Leading Technology towards Lab-on-a-Chip and Sensing Applications. *Sensors* **15,** 30011–30031 (2015).

11. Roggo, C. & van der Meer, J. R. Miniaturized and integrated whole cell living bacterial sensors in field applicable autonomous devices. *Curr. Opin. Biotechnol.* **45,** 24–33 (2017).

12. Syedmoradi, L. *et al.* Point of care testing: The impact of nanotechnology. *Biosens. Bioelectron.* **87,** 373–387 (2017).

13. Goers, L. *et al.* Whole-cell Escherichia coli lactate biosensor for monitoring mammalian cell cultures during biopharmaceutical production. *Biotechnol. Bioeng.* **114,** 1290–1300 (2017).

14. Misun, P. M., Rothe, J., Schmid, Y. R. F., Hierlemann, A. & Frey, O. Multi-analyte biosensor interface for real-time monitoring of 3D microtissue spheroids in hanging-drop networks. *Microsyst. Nanoeng.* **2,** 16022 (2016).

15. Ewald, M., Fechner, P. & Gauglitz, G. A multi-analyte biosensor for the simultaneous label-free detection of pathogens and biomarkers in point-of-need animal testing. *Anal. Bioanal. Chem.* **407,** 4005–4013 (2015).

16. IBM Research Alliance Builds New Transistor for 5nm Tech. (2017). Available at: http://www-03.ibm.com/press/us/en/pressrelease/52531.wss. (Accessed: 21st February 2018)

17. Sorgenfrei, S. *et al.* Label-free single-molecule detection of DNA-hybridization kinetics with a carbon nanotube field-effect transistor. *Nat. Nanotechnol.* **6,** 126–132 (2011).

18. Zhang, Y. *et al.* New Gold Nanostructures for Sensor Applications: A Review. *Materials* **7,** 5169–5201 (2014).

19. Zhang, G.-J. & Ning, Y. Silicon nanowire biosensor and its applications in disease diagnostics: A review. *Anal. Chim. Acta* **749,** 1–15 (2012).

20. Cui, Y., Zhong, Z. H., Wang, D. L., Wang, W. U. & Lieber, C. M. High performance silicon nanowire field effect transistors. *Nano Lett.* **3,** 149–152 (2003).

21. Zheng, G., Lu, W., Jin, S. & Lieber, C. M. Synthesis and Fabrication of High-Performance n-Type Silicon Nanowire Transistors. *Adv. Mater.* **16,** 1890–1893 (2004).

22. Wang, W. U., Chen, C., Lin, K., Fang, Y. & Lieber, C. M. Label-free detection of small-molecule–protein interactions by using nanowire nanosensors. *Proc. Natl. Acad. Sci. U. S. A.* **102,** 3208–3212 (2005).

23. Patolsky, F., Zheng, G. & Lieber, C. M. Fabrication of silicon nanowire devices for ultrasensitive, label-free, real-time detection of biological and chemical species. *Nat. Protoc.* **1,** 1711–1724 (2006).

24. Cui, Y. & Lieber, C. M. Functional Nanoscale Electronic Devices Assembled Using Silicon Nanowire Building Blocks. *Science* **291,** 851–853 (2001).

25. Cui, Y., Wei, Q., Park, H. & Lieber, C. Nanowire nanosensors for highly sensitive and selective detection of biological and chemical species. *Science* **293,** 1289–1292 (2001).

26. Gao, X. P. A., Zheng, G. & Lieber, C. M. Subthreshold Regime has the Optimal Sensitivity for Nanowire FET Biosensors. *Nano Lett.* **10,** 547 (2010).

27. Chen, K.-I., Li, B.-R. & Chen, Y.-T. Silicon nanowire field-effect transistor-based biosensors for biomedical diagnosis and cellular recording investigation. *Nano Today* **6,** 131 – 154 (2011).

28. Shehada, N. *et al.* Ultrasensitive Silicon Nanowire for Real-World Gas Sensing: Noninvasive Diagnosis of Cancer from Breath Volatolome. *Nano Lett.* **15,** 1288–1295 (2015).

29. Sivakumarasamy, R. *et al.* Selective layer-free blood serum ionogram based on ion-specific interactions with a nanotransistor. *Nat. Mater.* **17,** 464–470 (2018).

30. Kim, A. *et al.* Ultrasensitive, label-free, and real-time immunodetection using silicon field-effect transistors. *Appl. Phys. Lett.* **91,** 103901 (2007).

31. Puppo, F. *et al.* High sensitive detection in tumor extracts with SiNW-FET in-air biosensors. in *IEEE SENSORS 2014 Proceedings* 866–869 (2014). doi:10.1109/ICSENS.2014.6985137

32. Presnova, G. *et al.* Biosensor based on a silicon nanowire field-effect transistor functionalized by gold nanoparticles for the highly sensitive determination of prostate specific antigen. *Biosens. Bioelectron.* **88,** 283–289 (2017).

33. N, M. N. M. *et al.* Top-Down Nanofabrication and Characterization of 20 nm Silicon Nanowires for Biosensing Applications. *PLOS ONE* **11,** e0152318 (2016).

34. Hahm, J. & Lieber, C. M. Direct Ultrasensitive Electrical Detection of DNA and DNA Sequence Variations Using Nanowire Nanosensors. *Nano Lett.* **4,** 51–54 (2004).

35. Regonda, S. *et al.* Silicon multi-nanochannel FETs to improve device uniformity/stability and femtomolar detection of insulin in serum. *Biosens. Bioelectron.* **45,** 245–251 (2013).

36. Randviir, E. P. & Banks, C. E. Electrochemical impedance spectroscopy: an overview of bioanalytical applications. *Anal. Methods* **5,** 1098–1115 (2013).

37. Gu, W. & Zhao, Y. Cellular electrical impedance spectroscopy: an emerging technology of microscale biosensors. *Expert Rev. Med. Devices* **7,** 767–779 (2010).

38. Chen, J. *et al.* Microfluidic Impedance Flow Cytometry Enabling High-Throughput Single-Cell Electrical Property Characterization. *Int. J. Mol. Sci.* **16,** 9804–9830 (2015).

39. Sun, T. & Morgan, H. Single-cell microfluidic impedance cytometry: a review. *Microfluid. Nanofluidics* **8,** 423–443 (2010).

40. Holmes, D. *et al.* Leukocyte analysis and differentiation using high speed microfluidic single cell impedance cytometry. *Lab. Chip* **9,** 2881–2889 (2009).

41. Holmes, D. & Morgan, H. Single Cell Impedance Cytometry for Identification and Counting of CD4 T-Cells in Human Blood Using Impedance Labels. *Anal. Chem.* **82,** 1455–1461 (2010).

42. Han, X., van Berkel, C., Gwyer, J., Capretto, L. & Morgan, H. Microfluidic Lysis of Human Blood for Leukocyte Analysis Using Single Cell Impedance Cytometry. *Anal. Chem.* **84,** 1070–1075 (2012).

43. Haandbæk, N., Bürgel, S. C., Heer, F. & Hierlemann, A. Characterization of subcellular morphology of single yeast cells using high frequency microfluidic impedance cytometer. *Lab. Chip* **14,** 369–377 (2013).

44. Haandbæk, N., Bürgel, S. C., Rudolf, F., Heer, F. & Hierlemann, A. Characterization of Single Yeast Cell Phenotypes Using Microfluidic Impedance Cytometry and Optical Imaging. *ACS Sens.* **1,** 1020–1027 (2016).

45. McGrath, J. S. *et al.* Analysis of Parasitic Protozoa at the Single-cell Level using Microfluidic Impedance Cytometry. *Sci. Rep.* **7,** 2601 (2017).

46. Chiu, T.-K. *et al.* A low-sample-loss microfluidic system for the quantification of size-independent cellular electrical property—Its demonstration for the identification and characterization of circulating tumour cells (CTCs). *Sens. Actuators B Chem.* **246,** 29–37 (2017).

47. Song, H. *et al.* Identification of mesenchymal stem cell differentiation state using dual-micropore microfluidic impedance flow cytometry. *Anal. Methods* **8,** 7437–7444 (2016).

48. Dak, P. *et al.* Droplet-based Biosensing for Lab-on-a-Chip, Open Microfluidics Platforms. *Biosensors* **6,** (2016).

49. Zhu, Y. & Fang, Q. Analytical detection techniques for droplet microfluidics—A review. *Anal. Chim. Acta* **787,** 24–35 (2013).

50. Kaminski, T. S., Scheler, O. & Garstecki, P. Droplet microfluidics for microbiology: techniques, applications and challenges. *Lab. Chip* **16,** 2168–2187 (2016).

51. Shang, L., Cheng, Y. & Zhao, Y. Emerging Droplet Microfluidics. *Chem. Rev.* **117,** 7964–8040 (2017).

52. Makarov, S. N., Ludwig, R. & Bitar, S. *Practical Electrical Engineering*.

53. Feynman, R. P. There's Plenty of Room at the Bottom. *Eng. Sci.* **23,** 22–36 (1960).

54. Moore, G. E. Cramming more components onto integrated circuits, Reprinted from Electronics, volume 38, number 8, April 19, 1965, pp.114 ff. *IEEE Solid-State Circuits Soc. Newsl.* **11,** 33–35 (2006).

55. Peercy, P. S. The drive to miniaturization. *Nature* (2000). doi:10.1038/35023223

56. Reverté, L., Prieto-Simón, B. & Campàs, M. New advances in electrochemical biosensors for the detection of toxins: Nanomaterials, magnetic beads and microfluidics systems. A review. *Anal. Chim. Acta* **908,** 8–21 (2016).

57. Ramgir, N. S., Yang, Y. & Zacharias, M. Nanowire-based sensors. *Small Weinh. Bergstr. Ger.* **6,** 1705–1722 (2010).

58. You, C.-C. *et al.* Detection and identification of proteins using nanoparticle–fluorescent polymer ‘chemical nose’ sensors. *Nat. Nanotechnol.* **2,** 318–323 (2007).

59. Wang, L. *et al.* ZnO nanorod gas sensor for ethanol detection. *Sens. Actuators B Chem.* **162,** 237–243 (2012).

60. Kong, J. *et al.* Nanotube Molecular Wires as Chemical Sensors. *Science* **287,** 622–625 (2000).

61. Shao, Y. *et al.* Graphene Based Electrochemical Sensors and Biosensors: A Review. *Electroanalysis* **22,** 1027–1036 (2010).

62. Mehrotra, P. Biosensors and their applications – A review. *J. Oral Biol. Craniofacial Res.* **6,** 153–159 (2016).

63. Hock, B., Seifert, M. & Kramer, K. Engineering receptors and antibodies for biosensors. *Biosens. Bioelectron.* **17,** 239–249 (2002).

64. Marrazza, G. Aptamer Sensors. *Biosensors* **7,** (2017).

65. Zhu, C., Yang, G., Li, H., Du, D. & Lin, Y. Electrochemical Sensors and Biosensors Based on Nanomaterials and Nanostructures. *Anal. Chem.* **87,** 230–249 (2015).

66. Zörgiebel, F. M. *et al.* Schottky barrier-based silicon nanowire pH sensor with live sensitivity control. *Nano Res.* **7,** 263–271 (2014).

67. Roh, S., Chung, T. & Lee, B. Overview of the Characteristics of Micro- and Nano-Structured Surface Plasmon Resonance Sensors. *Sensors* **11,** 1565–1588 (2011).

68. Stampfer, C. *et al.* Nano-Electromechanical Displacement Sensing Based on Single-Walled Carbon Nanotubes. *Nano Lett.* **6,** 1449–1453 (2006).

69. Lim, D.-K. *et al.* Highly uniform and reproducible surface-enhanced Raman scattering from DNA-tailorable nanoparticles with 1-nm interior gap. *Nat. Nanotechnol.* **6,** 452–460 (2011).

70. Li, H., Shi, L., Sun, D., Li, P. & Liu, Z. Fluorescence resonance energy transfer biosensor between upconverting nanoparticles and palladium nanoparticles for ultrasensitive CEA detection. *Biosens. Bioelectron.* **86,** 791–798 (2016).

71. Pierce, J. R. The naming of the transistor. *Proc. IEEE* **86,** 37–45 (1998).

72. Löcherer, K.-H. *Halbleiterbauelemente*. (1992).

73. Wang, F. F. Y. *Impurity Doping Processes in Silicon*. (Elsevier, 2012).

74. Hering, E., Bressler, K. & Gutekunst, J. *Elektronik für Ingenieure*. (Springer, 2001).

75. *Handbook of semiconductor manufacturing technology*. (CRC Press, 2008).

76. Pachauri, V. & Ingebrandt, S. Biologically sensitive field-effect transistors: from ISFETs to NanoFETs. *Essays Biochem.* **60,** 81–90 (2016).

77. van Hal, R. E. G., Eijkel, J. C. T. & Bergveld, P. A novel description of ISFET sensitivity with the buffer capacity and double-layer capacitance as key parameters. *Sens. Actuators B Chem.* **24,** 201–205 (1995).

78. Purushothaman, S., Toumazou, C. & Ou, C.-P. Protons and single nucleotide polymorphism detection: A simple use for the Ion Sensitive Field Effect Transistor. *Sens. Actuators B Chem.* **114,** 964–968 (2006).

79. Baumann, W. H. *et al.* Microelectronic sensor system for microphysiological application on living cells. *Sens. Actuators B Chem.* **55,** 77–89 (1999).

80. Park, H.-J. *et al.* An ISFET biosensor for the monitoring of maltose-induced conformational changes in MBP. *FEBS Lett.* **583,** 157–162 (2009).

81. Gubanova, O. *et al.* Fabrication and package of ISFET biosensor for micro volume analysis with the use of direct ink writing approach. *Mater. Sci. Semicond. Process.* **60,** 71–78 (2017).

82. Ohno, Y., Maehashi, K. & Matsumoto, K. Label-Free Biosensors Based on Aptamer-Modified Graphene Field-Effect Transistors. *J. Am. Chem. Soc.* **132,** 18012–18013 (2010).

83. Sarkar, D. *et al.* MoS2 Field-Effect Transistor for Next-Generation Label-Free Biosensors. *ACS Nano* **8,** 3992–4003 (2014).

84. Jacobs, C. B., Peairs, M. J. & Venton, B. J. Review: Carbon nanotube based electrochemical sensors for biomolecules. *Anal. Chim. Acta* **662,** 105–127 (2010).

85. Curreli, M. *et al.* Real-Time, Label-Free Detection of Biological Entities Using Nanowire-Based FETs. *IEEE Trans. Nanotechnol.* **7,** 651–667 (2008).

86. Datta, S., Kanjilal, B. & Sarkar, P. Electrochemical Sensor for Detection of Polyphenols in Tea and Wine with Differential Pulse Voltammetry and Electrochemical Impedance Spectroscopy Utilizing Tyrosinase and Gold Nanoparticles Decorated Biomembrane. *J. Electrochem. Soc.* **164,** B118–B126 (2017).

87. Department of Clinical Skills Experimental Teaching Center, Wuchang Hospital, Qiqihaer City, Heilongjiang Province, 161000, P.R. China & Ding, L. Detection of Insulin-Like Growth Factor 1 Based on an Electrochemical Impedance Spectroscopy Sensor. *Int. J. Electrochem. Sci.* 11163–11170 (2017). doi:10.20964/2017.12.37

88. Clemente, F., Arpaia, P. & Manna, C. Characterization of human skin impedance after electrical treatment for transdermal drug delivery. *Measurement* **46,** 3494–3501 (2013).

89. Köster, O., Schuhmann, W., Vogt, H. & Mokwa, W. Quality control of ultra-microelectrode arrays using cyclic voltammetry, electrochemical impedance spectroscopy and scanning electrochemical microscopy. *Sens. Actuators B Chem.* **76,** 573–581 (2001).

90. Westbroek, P. *et al.* Quality Control of Textile Electrodes by Electrochemical Impedance Spectroscopy. *Text. Res. J.* **76,** 152–159 (2006).

91. Chiwunze, T. E., Thapliyal, N. B., Palakollu, V. N. & Karpoormath, R. A Simple, Efficient and Ultrasensitive Gold Nanourchin Based Electrochemical Sensor for the Determination of an Antimalarial Drug: Mefloquine. *Electroanalysis* **29,** 2138–2146 (2017).

92. Orazem, M. E. & Tribollet, B. *Electrochemical impedance spectroscopy*. (Wiley, 2008).

93. Grossi, M. & Riccò, B. Electrical impedance spectroscopy (EIS) for biological analysis and food characterization: a review. *J. Sens. Sens. Syst.* **6,** 303–325 (2017).

94. Ward, A. C., Connolly, P. & Tucker, N. P. Pseudomonas aeruginosa Can Be Detected in a Polymicrobial Competition Model Using Impedance Spectroscopy with a Novel Biosensor. *PLoS ONE* **9,** (2014).

95. Dastider, S. G., Barizuddin, S., Dweik, M. & Almasri, M. A micromachined impedance biosensor for accurate and rapid detection of E. coli O157:H7. *RSC Adv.* **3,** 26297 (2013).

96. Gomez-Sjoberg, R., Morisette, D. T. & Bashir, R. Impedance microbiology-on-a-chip: microfluidic bioprocessor for rapid detection of bacterial metabolism. *J. Microelectromechanical Syst.* **14,** 829–838 (2005).

97. Holmes, D. & Webb, B. L. J. Electrical Impedance Cytometry. in *Encyclopedia of Nanotechnology* 662–671 (Springer, Dordrecht, 2012). doi:10.1007/978-90-481-9751-4_122

98. Xu, Y. *et al.* A review of impedance measurements of whole cells. *Biosens. Bioelectron.* **77,** 824–836 (2016).

99. Sun, T., Bernabini, C. & Morgan, H. Single-Colloidal Particle Impedance Spectroscopy: Complete Equivalent Circuit Analysis of Polyelectrolyte Microcapsules. *Langmuir* **26,** 3821–3828 (2010).

100. Coulter, W. H. High speed automatic blood cell counter and cell analyzer. *Proc Natl Electron Conf* **12,** 1034–1040 (1956).

101. Larsen, U. D., Blankenstein, G. & Branebjerg, J. Microchip Coulter particle counter. in *Solid State Sensors and Actuators, 1997. TRANSDUCERS'97 Chicago., 1997 International Conference on* **2,** 1319–1322 (IEEE, 1997).

102. Saleh, O. A. & Sohn, L. L. Quantitative sensing of nanoscale colloids using a microchip Coulter counter. *Rev. Sci. Instrum.* **72,** 4449–4451 (2001).

103. Branton, D. *et al.* The potential and challenges of nanopore sequencing. *Nat. Biotechnol.* **26,** 1146–1153 (2008).

104. Gawad, S., Schild, L. & Renaud, P. Micromachined impedance spectroscopy flow cytometer for cell analysis and particle sizing. *Lab. Chip* **1,** 76–82 (2001).

105. Bernabini, C., Holmes, D. & Morgan, H. Micro-impedance cytometry for detection and analysis of micron-sized particles and bacteria. *Lab. Chip* **11,** 407–412 (2011).

106. Zheng, Y., Shojaei-Baghini, E., Azad, A., Wang, C. & Sun, Y. High-throughput biophysical measurement of human red blood cells. *Lab. Chip* **12,** 2560–2567 (2012).

107. Chen, J. *et al.* Classification of cell types using a microfluidic device for mechanical and electrical measurement on single cells. *Lab. Chip* **11,** 3174–3181 (2011).

108. Zhao, Y. *et al.* A microfluidic system enabling continuous characterization of specific membrane capacitance and cytoplasm conductivity of single cells in suspension. *Biosens. Bioelectron.* **43,** 304–307 (2013).

109. Zhao, Y. *et al.* A microfluidic system for cell type classification based on cellular size-independent electrical properties. *Lab. Chip* **13,** 2272–2277 (2013).

110. Song, H. *et al.* A microfluidic impedance flow cytometer for identification of differentiation state of stem cells. *Lab. Chip* **13,** 2300–2310 (2013).

111. Onnela, N. *et al.* Electric impedance of human embryonic stem cell-derived retinal pigment epithelium. *Med. Biol. Eng. Comput.* **50,** 107–116 (2012).

112. *Encyclopedia of microfluidics and nanofluidics*. (Springer, 2015).

113. Dixit, C. K. & Kaushik, A. K. Microfluidics for Biologists: Fundamentals and Applications. (2016).

114. Whitesides, G. M. The origins and the future of microfluidics. *Nature* **442,** 368–373 (2006).

115. Beebe, D. J., Mensing, G. A. & Walker, G. M. Physics and Applications of Microfluidics in Biology. *Annu. Rev. Biomed. Eng.* **4,** 261–286 (2002).

116. Brody, J. P., Yager, P., Goldstein, R. E. & Austin, R. H. Biotechnology at low Reynolds numbers. *Biophys. J.* **71,** 3430–3441 (1996).

117. Lin, Y.-C., Chung, Y.-C. & Wu, C.-Y. Mixing enhancement of the passive microfluidic mixer with J-shaped baffles in the tee channel. *Biomed. Microdevices* **9,** 215–221 (2007).

118. Lynn, N. S. & Dandy, D. S. Passive microfluidic pumping using coupled capillary/evaporation effects. *Lab. Chip* **9,** 3422–3429 (2009).

119. Novo, P., Chu, V. & Conde, J. P. Integrated optical detection of autonomous capillary microfluidic immunoassays:a hand-held point-of-care prototype. *Biosens. Bioelectron.* **57,** 284–291 (2014).

120. Tsai, J.-H. & Lin, L. Active microfluidic mixer and gas bubble filter driven by thermal bubble micropump. *Sens. Actuators Phys.* **97–98,** 665–671 (2002).

121. Jackson, W. C., Tran, H. D., O'Brien, M. J., Rabinovich, E. & Lopez, G. P. Rapid prototyping of active microfluidic components based on magnetically modified elastomeric materials. *J. Vac. Sci. Technol. B Microelectron. Nanometer Struct. Process. Meas. Phenom.* **19,** 596–599 (2001).

122. Zhang, Y. S. *et al.* Multisensor-integrated organs-on-chips platform for automated and continual in situ monitoring of organoid behaviors. *Proc. Natl. Acad. Sci. U. S. A.* **114,** E2293–E2302 (2017).

123. Jeong, S. *et al.* A Three-Dimensional Arrayed Microfluidic Blood #8211;Brain Barrier Model With Integrated Electrical Sensor Array. *IEEE Trans. Biomed. Eng.* **65,** 431–439 (2018).

124. Shih, K. *et al.* Microfluidic metamaterial sensor: Selective trapping and remote sensing of microparticles. *J. Appl. Phys.* **121,** 023102 (2017).

125. Moon, J.-M. *et al.* A disposable amperometric dual-sensor for the detection of hemoglobin and glycated hemoglobin in a finger prick blood sample. *Biosens. Bioelectron.* **91,** 128–135 (2017).

126. Cinti, S., Minotti, C., Moscone, D., Palleschi, G. & Arduini, F. Fully integrated ready-to-use paper-based electrochemical biosensor to detect nerve agents. *Biosens. Bioelectron.* **93,** 46–51 (2017).

127. Singh, C. *et al.* Biofunctionalized graphene oxide wrapped carbon nanotubes enabled microfluidic immunochip for bacterial cells detection. *Sens. Actuators B Chem.* **255,** 2495–2503 (2018).

128. Kong, Q., Wang, Y., Zhang, L., Ge, S. & Yu, J. A novel microfluidic paper-based colorimetric sensor based on molecularly imprinted polymer membranes for highly selective and sensitive detection of bisphenol A. *Sens. Actuators B Chem.* **243,** 130–136 (2017).

129. Wang, L., Musile, G. & McCord, B. R. An aptamer-based paper microfluidic device for the colorimetric determination of cocaine. *Electrophoresis* **39,** 470–475 (2018).

130. Kim, J.-M., Lim, J., Lee, T.-R. & Park, S. PDMS-based Screw-wall Microfluidic Channel Forming a Turbulent Flow at Low Reynold Number. *J. Korean Phys. Soc.* **73,** 60–64 (2018).

131. Wang, X., Zandi, M., Ho, C.-C., Kaval, N. & Papautsky, I. Single stream inertial focusing in a straight microchannel. *Lab. Chip* **15,** 1812–1821 (2015).

132. Cohen, C. *et al.* Parallelised production of fine and calibrated emulsions by coupling flow-focusing technique and partial wetting phenomenon. *Microfluid. Nanofluidics* **17,** 959–966 (2014).

133. Guo, M. T., Rotem, A., Heyman, J. A. & Weitz, D. A. Droplet microfluidics for high-throughput biological assays. *Lab. Chip* **12,** 2146 (2012).

134. Teh, S.-Y., Lin, R., Hung, L.-H. & Lee, A. P. Droplet microfluidics. *Lab. Chip* **8,** 198–220 (2008).

135. Hung, L.-H. *et al.* Alternating droplet generation and controlled dynamic droplet fusion in microfluidic device for CdS nanoparticle synthesis. *Lab. Chip* **6,** 174 (2006).

136. Collignon, S., Friend, J. & Yeo, L. Planar microfluidic drop splitting and merging. *Lab. Chip* **15,** 1942–1951 (2015).

137. Laval, P., Lisai, N., Salmon, J.-B. & Joanicot, M. A microfluidic device based on droplet storage for screening solubility diagrams. *Lab. Chip* **7,** 829–834 (2007).

138. Zhu, P. & Wang, L. Passive and active droplet generation with microfluidics: a review. *Lab. Chip* **17,** 34–75 (2017).

139. On the Stability, or Instability, of certain Fluid Motions - Rayleigh - 1879 - Proceedings of the London Mathematical Society - Wiley Online Library.

140. Squires, T. M. & Quake, S. R. Microfluidics: Fluid physics at the nanoliter scale. *Rev. Mod. Phys.* **77,** 977–1026 (2005).

141. Baroud, C. N., Gallaire, F. & Dangla, R. Dynamics of microfluidic droplets. *Lab. Chip* **10,** 2032 (2010).

142. Garstecki, P., Fuerstman, M. J., Stone, H. A. & Whitesides, G. M. Formation of droplets and bubbles in a microfluidic T-junction—scaling and mechanism of break-up. *Lab. Chip* **6,** 437 (2006).

143. Menech, M. D., Garstecki, P., Jousse, F. & Stone, H. A. Transition from squeezing to dripping in a microfluidic T-shaped junction. *J. Fluid Mech.* **595,** 141–161 (2008).

144. Martin, M. & Klaus, R. *Immunologie*. (UTB GmbH, 2009).

145. Kaufmann, S. H. E. *Basiswissen Immunologie: mit 17 Tabellen*. (Springer, 2014).

146. Pecankova, K., Majek, P., Cermak, J. & Dyr, J. E. Peripheral Blood Mononuclear Cell Proteome Changes in Patients with Myelodysplastic Syndrome. *BioMed Res. Int.* **2015,** (2015).

147. Swisher, E. M. *et al.* Somatic Mosaic Mutations in PPM1D and TP53 in the Blood of Women With Ovarian Carcinoma. *JAMA Oncol.* **2,** 370–372 (2016).

148. Zikos, T. A., Donnenberg, A. D., Landreneau, R. J., Luketich, J. D. & Donnenberg, V. S. Lung T-cell subset composition at the time of surgical resection is a prognostic indicator in non-small cell lung cancer. *Cancer Immunol. Immunother. CII* **60,** 819–827 (2011).

149. Garg, N. J. *et al.* Changes in Proteome Profile of Peripheral Blood Mononuclear Cells in Chronic Chagas Disease. *PLoS Negl. Trop. Dis.* **10,** (2016).

150. de Almeida, T. V. V. S. *et al.* Schistosoma mansoni antigens alter activation markers and cytokine profile in lymphocytes of patients with asthma. *Acta Trop.* **166,** 268–279 (2017).

151. Olsen, N. J., Moore, J. H. & Aune, T. M. Gene expression signatures for autoimmune disease in peripheral blood mononuclear cells. *Arthritis Res. Ther.* **6,** 120–128 (2004).

152. Bakker, E., Qattan, M., Mutti, L., Demonacos, C. & Krstic-Demonacos, M. The role of microenvironment and immunity in drug response in leukemia. *Biochim. Biophys. Acta BBA - Mol. Cell Res.* **1863,** 414–426 (2016).

153. Stewart, B. W., Wild, C., International Agency for Research on Cancer & World Health Organization. *World cancer report 2014*. (2014).

154. *World cancer report*. (IARC Press, 2003).

155. De Kouchkovsky, I. & Abdul-Hay, M. ‘Acute myeloid leukemia: a comprehensive review and 2016 update’”. *Blood Cancer J.* **6,** e441 (2016).

156. Estey, E. & Döhner, H. Acute myeloid leukaemia. *The Lancet* **368,** 1894–1907 (2006).

157. Appelbaum, F. R. *et al.* Age and acute myeloid leukemia. *Blood* **107,** 3481–3485 (2006).

158. Avissar, Y. *et al. Biology*. (2016).

159. *Biology*. (Macmillan Reference USA, 2002).

160. Covington, A., Bates, R. & Durst, R. Definition of Ph Scales, Standard Reference Values, Measurement of Ph and Related Terminology - (recommendations 1984). *Pure Appl. Chem.* **57,** 531–542 (1985).

161. Narendranath, N. V. & Power, R. Relationship between pH and Medium Dissolved Solids in Terms of Growth and Metabolism of Lactobacilli and Saccharomyces cerevisiae during Ethanol Production. *Appl. Environ. Microbiol.* **71,** 2239–2243 (2005).

162. Rousk, J., Brookes, P. C. & Bååth, E. Contrasting Soil pH Effects on Fungal and Bacterial Growth Suggest Functional Redundancy in Carbon Mineralization. *Appl. Environ. Microbiol.* **75,** 1589–1596 (2009).

163. Ma, L. *et al.* Rapid biodegradation of atrazine by Ensifer sp. strain and its degradation genes. *Int. Biodeterior. Biodegrad.* **116,** 133–140 (2017).

164. Monfoulet, L.-E. *et al.* The pH in the Microenvironment of Human Mesenchymal Stem Cells Is a Critical Factor for Optimal Osteogenesis in Tissue-Engineered Constructs. *Tissue Eng. Part A* **20,** 1827–1840 (2014).

165. Buselmaier, W. *Biologie für Mediziner*. (Springer, 2015).

166. *Electron microscopy: principles and fundamentals*. (VCH, 1997).

167. Mohammad, M. A., Muhammad, M., Dew, S. K. & Stepanova, M. Fundamentals of Electron Beam Exposure and Development. in *Nanofabrication* (eds. Stepanova, M. & Dew, S.) 11–41 (Springer Vienna, 2012). doi:10.1007/978-3-7091-0424-8_2

168. Auffan, M. *et al.* Electron Beam Lithography (EBL). in *Encyclopedia of Nanotechnology* (ed. Bhushan, B.) 718–740 (Springer Netherlands, 2012). doi:10.1007/978-90-481-9751-4_344

169. Electron Beam Technology. Available at: https://www.raith.com/technology/electron-beam-technology.html. (Accessed: 26th February 2018)

170. Kotera, M. & Niu, H. Influence of Electron Scattering on Resolution in Low-Dose Electron-Beam Lithography. *Jpn. J. Appl. Phys.* **43,** 3749 (2004).

171. Dai, Q., Lee, S.-Y., Lee, S.-H., Kim, B.-G. & Cho, H.-K. Experiment-based estimation of point spread function in electron-beam lithography: Forward-scattering part. *Microelectron. Eng.* **88,** 3054–3061 (2011).

172. Seo, E. & Kim, O. Dose and Shape Modification Proximity Effect Correction for Forward-Scattering Range Scale Features in Electron Beam Lithography. *Jpn. J. Appl. Phys.* **39,** 6827 (2000).

173. Anderson, E. H., Olynick, D. L., Chao, W., Harteneck, B. & Veklerov, E. Influence of sub-100 nm scattering on high-energy electron beam lithography. *J. Vac. Sci. Technol. B Microelectron. Nanometer Struct. Process. Meas. Phenom.* **19,** 2504–2507 (2001).

174. e-Beam Lithography resists from MicroChem Corp. Available at: http://www.microchem.com/Appl-E-Beam.htm. (Accessed: 26th February 2018)

175. CNF - Electron Beam Lithography Resist Capabilities. Available at: http://www.cnf.cornell.edu/cnf_process_ebl_resists.html. (Accessed: 26th February 2018)

176. Chen, W. & Ahmed, H. Fabrication of 5–7 nm wide etched lines in silicon using 100 keV electron-beam lithography and polymethylmethacrylate resist. *Appl. Phys. Lett.* **62,** 1499–1501 (1993).

177. Vieu, C. *et al.* Electron beam lithography: resolution limits and applications. *Appl. Surf. Sci.* **164,** 111–117 (2000).

178. Zailer, I., Frost, J. E. F., Chabasseur-Molyneux, V., Ford, C. J. B. & Pepper, M. Crosslinked PMMA as a high-resolution negative resist for electron beam lithography and applications for physics of low-dimensional structures. *Semicond. Sci. Technol.* **11,** 1235 (1996).

179. Hoole, A. C. F., Welland, M. E. & Broers, A. N. Negative PMMA as a high-resolution resist - the limits and possibilities. *Semicond. Sci. Technol.* **12,** 1166 (1997).

180. Lee, E. H., Rao, G. R. & Mansur, L. K. LET effect on cross-linking and scission mechanisms of PMMA during irradiation. *Radiat. Phys. Chem.* **55,** 293–305 (1999).

181. DWL 66+ - Home. Available at: https://www.himt.de/index.php/dwl66.html. (Accessed: 6th August 2018)

182. WieWeb software. Available at: http://www.wieweb.com/ns6/index.html. (Accessed: 9th August 2018)

183. Lin, B. J. & SPIE. *Optical lithography here is why*. (SPIE, 2010).

184. Teh, W. H., Dürig, U., Drechsler, U., Smith, C. G. & Güntherodt, H.-J. Effect of low numerical-aperture femtosecond two-photon absorption on (SU-8) resist for ultrahigh-aspect-ratio microstereolithography. *J. Appl. Phys.* **97,** 054907 (2005).

185. Ponce, D. R. *et al.* Thermophysical analysis of SU8-modified microstructures created by visible light lithography. *J. Polym. Sci. Part B Polym. Phys.* **48,** 47–54 (2010).

186. Mitra, S. K. *Microfluidics and nanofluidics handbook*. (CRC, 2012).

187. MicroChem Corp. SU-8 2000 Permanent Epoxy Negative Photoresist PROCESSING GUIDELINES SU-8 2000.5, SU-8 2002, SU-8 2005, SU-8 2007, SU-8 2010 and SU-8 2015.

188. Carlier, J. *et al.* Integrated microfluidics based on multi-layered SU-8 for mass spectrometry analysis. *J. Micromechanics Microengineering* **14,** 619 (2004).

189. Chung, S. & Park, S. Effects of temperature on mechanical properties of SU-8 photoresist material. *J. Mech. Sci. Technol.* **27,** 2701–2707 (2013).

190. Lin, C.-H., Lee, G.-B., Chang, B.-W. & Chang, G.-L. A new fabrication process for ultra-thick microfluidic microstructures utilizing SU-8 photoresist. *J. Micromechanics Microengineering* **12,** 590 (2002).

191. Ramli, N. A., Arslan, T., Haridas, N. & Zhou, W. Design, simulation and analysis of a digital RF MEMS varactor using thick SU-8 polymer. *Microsyst. Technol.* **24,** 473–482 (2018).

192. Cui, Z. *Nanofabrication: principles, capabilities and limits*. (2011).

193. Merck Performance Materials GmbH. AZ 5214 E Photoresist Technical Data Sheet.

194. Xia, Y. & Whitesides, and G. M. Soft Lithography. *Annu. Rev. Mater. Sci.* **28,** 153–184 (1998).

195. Qin, D., Xia, Y. & Whitesides, G. M. Soft lithography for micro- and nanoscale patterning. *Nat. Protoc.* **5,** 491–502 (2010).

196. Chung, K., Crane, M. & Lu, H. Automated on-chip imaging and sorting of C. elegans. *Protoc. Exch.* (2009). doi:10.1038/nprot.2009.105

197. Sidorova, J. M., Li, N., Schwartz, D. C., Folch, A. & Monnat Jr, R. J. Microfluidic-assisted analysis of replicating DNA molecules. *Nat. Protoc.* **4,** 849–861 (2009).

198. Mata, A., Fleischman, A. J. & Roy, S. Characterization of Polydimethylsiloxane (PDMS) Properties for Biomedical Micro/Nanosystems. *Biomed. Microdevices* **7,** 281–293 (2005).

199. Xiong, L., Chen, P. & Zhou, Q. Adhesion promotion between PDMS and glass by oxygen plasma pre-treatment. *J. Adhes. Sci. Technol.* **28,** 1046–1054 (2014).

200. Shiroma, L. S. *et al.* Self-regenerating and hybrid irreversible/reversible PDMS microfluidic devices. *Sci. Rep.* **6,** 26032 (2016).

201. Pregl, S. *et al.* Parallel arrays of Schottky barrier nanowire field effect transistors: Nanoscopic effects for macroscopic current output. *Nano Res.* **6,** 381–388 (2013).

202. — NaMLab. Available at: http://www.namlab.de/. (Accessed: 2nd August 2018)

203. Nolting, D. *et al.* pH-Induced Protonation of Lysine in Aqueous Solution Causes Chemical Shifts in X-ray Photoelectron Spectroscopy. *J. Am. Chem. Soc.* **129,** 14068–14073 (2007).

204. Rueden, C. T. *et al.* ImageJ2: ImageJ for the next generation of scientific image data. *BMC Bioinformatics* **18,** (2017).

205. Pasternack, R. M., Rivillon Amy, S. & Chabal, Y. J. Attachment of 3-(Aminopropyl)triethoxysilane on Silicon Oxide Surfaces: Dependence on Solution Temperature. *Langmuir* **24,** 12963–12971 (2008).

206. Cossins, B. P., Jacobson, M. P. & Guallar, V. A New View of the Bacterial Cytosol Environment. *PLoS Comput. Biol.* **7,** (2011).

207. Stern, E. *et al.* Importance of the Debye Screening Length on Nanowire Field Effect Transistor Sensors. *Nano Lett.* **7,** 3405–3409 (2007).

208. Gao, N. *et al.* General strategy for biodetection in high ionic strength solutions using transistor-based nanoelectronic sensors. *Nano Lett.* **15,** 2143–2148 (2015).

209. Department of Creative IT Engineering. Available at: http://citeng.postech.ac.kr/. (Accessed: 26th April 2018)

210. Kim, K. *et al.* Silicon nanowire biosensors for detection of cardiac troponin I (cTnI) with high sensitivity. *Biosens. Bioelectron.* **77,** 695–701 (2016).

211. Rim, T. *et al.* Electrical Characteristics of Doped Silicon Nanowire Channel Field-Effect Transistor Biosensors. *IEEE Sens. J.* **17,** 667–673 (2017).

212. Rim, T. *et al.* Improved Electrical Characteristics of Honeycomb Nanowire ISFETs. *IEEE Electron Device Lett.* **34,** 1059–1061 (2013).

213. Rim, T. *et al.* Silicon Nanowire Biologically Sensitive Field Effect Transistors: Electrical Characteristics and Applications. *J. Nanosci. Nanotechnol.* **14,** 273–287 (2014).

214. Rim, T., Meyyappan, M. & Baek, C.-K. Optimized operation of silicon nanowire field effect transistor sensors. *Nanotechnology* **25,** 505501 (2014).

215. Kimizuka, O. *et al.* Electrochemical doping of pure single-walled carbon nanotubes used as supercapacitor electrodes. *Carbon* **46,** 1999–2001 (2008).

216. Sun, T., Gawad, S., Bernabini, C., Green, N. G. & Morgan, H. Broadband single cell impedance spectroscopy using maximum length sequences: theoretical analysis and practical considerations. *Meas. Sci. Technol.* **18,** 2859 (2007).

217. Foster, K. & Schwan, H. Dielectric-Properties of Tissues and Biological-Materials - a Critical-Review. *Crit. Rev. Biomed. Eng.* **17,** 25–104 (1989).

218. Bhagat, A. A. S., Kuntaegowdanahalli, S. S. & Papautsky, I. Inertial microfluidics for continuous particle filtration and extraction. *Microfluid. Nanofluidics* **7,** 217–226 (2009).

219. Carlo, D. D., Irimia, D., Tompkins, R. G. & Toner, M. Continuous inertial focusing, ordering, and separation of particles in microchannels. *Proc. Natl. Acad. Sci.* **104,** 18892–18897 (2007).

220. Zhang, J. *et al.* Fundamentals and applications of inertial microfluidics: a review. *Lab. Chip* **16,** 10–34 (2015).

221. Caballero, D., Katuri, J., Samitier, J. & Sánchez, S. Motion in microfluidic ratchets. *Lab. Chip* **16,** 4477–4481 (2016).

222. Winer, M. H., Ahmadi, A. & Cheung, K. C. Application of a three-dimensional (3D) particle tracking method to microfluidic particle focusing. *Lab Chip* **14,** 1443–1451 (2014).

223. Vardiman, J. W., Harris, N. L. & Brunning, R. D. The World Health Organization (WHO) classification of the myeloid neoplasms. *Blood* **100,** 2292–2302 (2002).

224. Kermany, D. S. *et al.* Identifying Medical Diagnoses and Treatable Diseases by Image-Based Deep Learning. *Cell* **172,** 1122–1131.e9 (2018).

225. Lannin, T. B., Thege, F. I. & Kirby, B. J. Comparison and optimization of machine learning methods for automated classification of circulating tumor cells. *Cytometry A* **89,** 922–931

226. Chen, C. L. *et al.* Deep Learning in Label-free Cell Classification. *Sci. Rep.* **6,** 21471 (2016).

227. Xu, M. *et al.* A deep convolutional neural network for classification of red blood cells in sickle cell anemia. *PLOS Comput. Biol.* **13,** e1005746 (2017).

228. Liu, F. T., Ting, K. M. & Zhou, Z.-H. Isolation-Based Anomaly Detection. *Acm Trans. Knowl. Discov. Data* **6,** 3 (2012).

229. Lloyd, S. Least-Squares Quantization in Pcm. *Ieee Trans. Inf. Theory* **28,** 129–137 (1982).

230. Zhu, Z., Xu, X., Fang, L., Pan, D. & Huang, Q. Investigation of geometry-dependent sensing characteristics of microfluidic electrical impedance spectroscopy through modeling and simulation. *Sens. Actuators B Chem.* **235,** 515–524 (2016).

231. Madigan, M. T., Martinko, J. M., Brock, T. D., Lazar, T. & Thomm, M. *Brock Mikrobiologie*. (Pearson Studium, 20).

Acknowledgements

Firstly, I want to thanks my supervisor Prof. Dr. Gianaurelio Cuniberti for giving me the opportunity to carry out my thesis in his chair. Besides giving me scientific advices and personal inputs, he gave me the freedom to work and think independently. Further, he gave me the chance to challenged myself by taking over task not directly related to science like organizations of events, supervising students or presenting our work to non-scientific people.

A special thanks to Dr. Larysa Baraban for guiding me through my whole doctoral studies. She always had an open ear for me when I was facing any problems and helped me to find solutions or to try out alternative ways. I highly appreciate, that she supervised me during the last 4 years and helped me to grow personally with my tasks and challenges.

I would like to thank Dr. Hans-Georg Braun for fruitful discussions in the field of nano- and micropatterning and I would like to appreciate my thanks for being the third reviewer of this thesis. Further, I would like to express my appreciation to Prof. Dr. Arben Merkoçi for being the second reviewer of this thesis.

Without the nice working atmosphere at the Max-Bergmann Zentrum I would have never be able to finish my PhD. Many thanks to the all members of the work groups on the 4th floor: Dr. Francesca Moresco, Dr. Bergoi Ibarlucea, Eunhye Baek, Rico Illing, Antonio Panes, Xinne Zhao, Dmitry Belyeav, Tao Huang, Justus Krüger, Frank Eisenhut, Dmitry Skidin and Tim Kühne. Special thanks to Stephanie Klinghammer for making office 410 a place like home.

Ein besonderer Dank gilt meiner Familie, die mich stets in meinen Entscheidungen unterstützt und ermutigt haben, sowie an meiner Seite standen.

Meine liebe Claudi, ohne deine Unterstützung wäre ich nie an dem Punkt, an dem ich heute wäre. Du warst und bist eine der wichtigsten Stützen in meinem Leben.

Finally, I wanted to thank all mentioned and not mentioned people, who supported me during my years of my PhD.